Development of High Frequency Soft-switched Inverter Configurations for Multi-load Induction Cooking System

A Thesis
Submitted in partial fulfillment of the requirements
for the award of the degree of

Doctor of Philosophy
in
Electrical Engineering

By
Bhavin Salvi
(Roll No. 701920)

Supervisor
Dr. S. Porpandiselvi
Associate Professor

Co-supervisor
Dr. N. Vishwanathan
Professor

Department of Electrical Engineering
National Institute of Technology Warangal
(An Institute of National Importance)
Warangal - 506004, Telangana State, India

October - 2023

Dedicated to

My beloved Parents and family

Late Shri Kishorkumar Salvi & Smt. Ruxmaniben Salvi

APPROVAL SHEET

This Thesis entitled **"Development of High Frequency Soft-switched Inverter Configurations for Multi-load Induction Cooking System"** by **Bhavin Salvi** (Roll No. 701920) is approved for the degree of Doctor of Philosophy.

Examiners

.....

.....

.....

Supervisor

Dr. S. Porpandiselvi
Associate Professor
EED, NIT Warangal

Co-supervisor

Dr. N. Vishwanathan
Professor
EED, NIT Warangal

Chairman

Dr. Bhagwan K. Murthy
Professor,
EED, NIT Warangal

Date:.....

Department of Electrical Engineering
National Institute of Technology Warangal
Warangal - 506004, Telangana State, India

DEPARTMENT OF ELECTRICAL ENGINEERING

NATIONAL INSTITUTE OF TECHNOLOGY WARANGAL

CERTIFICATE

This is to certify that the thesis titled **"Development of High Frequency Soft-switched Inverter Configurations for Multi-load Induction Cooking System"**, submitted by **Mr. Bhavin Salvi** (Roll No. 701920), is a bonafide work submitted to National Institute of Technology Warangal in partial fulfilment of the requirements for the award of the degree of **Doctor of Philosophy** in Electrical Engineering. To the best of my knowledge, the work incorporated in this thesis has not been submitted elsewhere for the award of any degree.

Dr. N. Vishwanathan
(Thesis Co-supervisor)
Professor
Department of Electrical Engineering
National Institute of Technology
Warangal-506004

Dr. S. Porpandiselvi
(Thesis Supervisor)
Associate Professor
Department of Electrical Engineering
National Institute of Technology
Warangal-506004

Date: October 17, 2023

Place: Warangal

DECLARATION

This is to certify that the work presented in the thesis entitled **"Development of High Frequency Soft-switched Inverter Configurations for Multi-load Induction Cooking System"** is a bonafide work done by me under the supervision of **Dr. S. Porpandiselvi**, Associate Professor and **Dr. N. Vishwanathan**, Professor, Department of Electrical Engineering, National Institute of Technology Warangal, India and was not submitted elsewhere for the award of any degree.

I declare that this written submission represents my ideas in my own words and where others' ideas or words have been included, I have adequately cited and referenced the original sources. I also declare that I have adhered to all principles of academic honesty and integrity and have not misrepresented or fabricated or falsified any idea / data / fact / source in my submission. I understand that any violation of the above will be a cause for disciplinary action by the Institute and can also evoke penal action from the sources which have thus not been properly cited or from whom proper permission has not been taken when needed.

Date: October 17, 2023
Place: Warangal

Bhavin Salvi
(Research Scholar - 701920)

ACKNOWLEDGMENTS

It gives me immense pleasure to express my deep sense of gratitude and thanks to my supervisor **Dr. S. Porpandiselvi**, Associate Professor & co-supervisor **Dr. N Vishwanathan**, Professor, Department of Electrical Engineering, National Institute of Technology Warangal, for their invaluable guidance, support, and suggestions. Their knowledge, suggestions, and discussions helped me become a capable researcher. They have shown me the imaginative side of this wonderful and potential research area. Their encouragement helped me to overcome the difficulties encountered in research as well in my life.

I wish to express my sincere thanks to **Prof. Bidyadhar Subudhi,** Director, NIT Warangal for his official support and encouragement.

I also express my sincere thanks to **Prof. N V Ramana Rao,** Former Director, NIT Warangal for his official support and encouragement.

I am very much thankful to **Prof. B. L. Narsimharaju**, Head, Department of Electrical Engineering for his support and cooperation.

I also express my sincere thanks to **Prof. Sailaja Kumari** and **Prof. S. Srinivasa Rao**, Former heads, Department of Electrical Engineering for their valuable suggestions, support and cooperation.

I take this opportunity to thank all my Doctoral Scrutiny Committee members, **Prof. Bhagwan K. Murthy**, Department of Electrical Engineering, **Dr. A. Kirubakaran**, Associate Professor, Department of Electrical Engineering, **Dr. D. Sreenivasarao**, Associate Professor, Department of Electrical Engineering and **Prof. N. Bheema Rao**, Department of Electronics and Communication Engineering for their detailed review, constructive suggestions and excellent advice during the progress of this research work.

I also appreciate the encouragement from teaching and non-teaching members of Department of Electrical Engineering. They have always been encouraging and supportive.

I convey my special thanks to contemporary research scholars Dr. Sumon Dhara, Dr. Srinivas K, Dr. Chinmay Das, Dr. Arunkumar C R, Mr. Chandrasekhar, Mr. P. Manoj, Mrs. Parvathy M L, Mr. Dinesh, and Mr. Bhanu for being with me during my research journey.

I acknowledge my gratitude to all my teachers and colleagues at various places for supporting and co-operating with me to complete the work.

I am grateful to my beloved parents, dear wife and family members for their counsel, support and encouragement.

Above all, I express my deepest regards and gratitude to **"ALMIGHTY"** whose divine light and warmth showered upon me the perseverance, inspiration, faith and enough strength to keep the momentum of work high even at tough moments of research work.

Bhavin Salvi

ABSTRACT

Ensuring sustainable future for humanity has become challenging mainly due to global warming and increased pollution. United Nations (UN) has laid 17 sustainable development goals (SDGs). Most of them are appertaining to sustainable technological advancement. Decarbonization in the recent technology and industrial applications play a key role in achieving sustainable cities. Electrification plays a vital role in fulfilling this aim. Induction heating has been identified as a propitious technology for decarbonization. Induction heating (IH) is a trending technology for various domestic, industrial and medical applications due to its multiple advantages such as contact-less heating, environment friendliness and high efficiency. Advancement in technologies such as switching device, digital power control and magnetic components has lead to highly efficiency IH systems which outperforms traditional heating methods.

Induction cookers(IC) have gained popularity in the domestic market over recent past. Hearing multiple vessels at a time is a common requirement of induction cooking systems. Resonant inverters are mostly preferred for IH applications owing to their high efficiency. There is an increasing research to develop compact and efficient induction cooking system (ICS) for multiple load IH application. In this thesis, various topologies used for IH application are discussed in detail. The major challenges associated with heating non-ferromagnetic type material vessels along with the proposed solutions are described in detail. This thesis proposes four different resonant inverter topologies for multiple load IH application. The detailed design, analysis, simulation and experimentation of all the proposed topologies are described in detail. Simulations of the inverters are performed in OrCAD PSpice and MATLAB Simulink softwares. Experimental prototypes ranging from 550 W to 2 kW have been designed. The performance of the proposed inverters have been validated with simulation and experimental results.

The first proposed configuration is a three switch resonant inverter for multiple ferromagnetic (FM) induction heating loads. It uses asymmetric duty cycle control for independently controlling two similar steel vessel loads. It offers maximum efficiency of 96.3%. It provides lowest switch to load ratio for induction cooking application. It can also be extended for more number of loads by addition of three switch inverter legs.

The second proposed configuration is a full-bridge (FB) based multi-load inverter for

powering multiple different material IH loads. Along with FB, it uses switch-diode modules to power and control each IH load. It uses ON-OFF control technique for simultaneous and independent power control of IH loads. It offers efficiency of 94.3%. It provides extension for multiple loads with a reduced additional component count.

The third proposed configuration is a three switch dual frequency resonant inverter for induction heating applications. It uses three switches and a split capacitor arrangement for powering two different material IH loads. Steel and aluminum vessels are used as IH loads. Duty cycle and frequency based controls are implemented for independently powering two different material loads. The maximum efficiency of the inverter is 96.11%.

The fourth proposed configuration is a dual half-bridge three switch resonant inverter for different material IH application. It removes the lossy split capacitor arrangement used in the first and third configurations. It increases the efficiency of the inverter and component count is reduced. It offers an efficiency of 97.38%. Independent control is obtained using duty cycle and frequency based controls.

All the proposed inverter configurations have been found suitable for multiple load induction cooking application. The working and operation of these converters are studied thoroughly and explained in this thesis. Hardware prototypes are built for all four proposed inverter configurations. The operation of all the inverter configurations have been validated with simulation and experimental results.

Contents

List of Figures

List of Tables

Abbreviations & Symbols

List of Abbreviations

3S-DFRI	Three Switch Dual Frequency Resonant Inverter
3SI	Three Switch Resonant Inverter
AC	Alternating Current
ADC	Asymmetric Duty Cycle
AVC	Asymmetric Voltage Cancellation
C	Capacitor
DC	Direct Current
DHB-3SRI	Dual Half-Bridge Three Switch Resonant Inverter
DSP	Digital Signal Processor
DST	Department of Science & Technology
EMC	Electromagnetic Compatibility
EMI	Electromagnetic Interference
EMS	Electro-mechanical Switches
EPWM	Enhanced Pulse Width Modulation
ESR	Equivalent Series Resistance
FB-MI	Full-Bridge based Multi-load Inverter
FB	Full-bridge
FFT	Fast Fourier Transform

FM	Ferromagnetic
FM	Frequency Modulation
FPGA	Field Programmable Gate Arrays
HB	Half-bridge
HS	Hard Switching
ICS	Induction Cooking System
IC	Induction Cooking
IHS	Induction Heating System
IH	Induction Heating
LAM	Load Adaptive Modulation
L	Inductor
MDO	Mixed Domain Oscilloscope
N-FM	Non-Ferromagnetic
PDM	Pulse Density Modulation
PSC	Phase-Shift Control
PWM	Pulse Width Modulation
Q	Quality Factor
RMS	Root Mean Square
SDGs	Sustainable Development Goals
SRI	Series Resonant Inverter
SS	Soft Switching
SW	Square Wave
THD	Total Harmonic Distortion

UN	United Nations
ZVS	Zero Voltage Switching

List of Symbols

α, β	Control angles
δ	Skin depth from the vessel surface
μ	Magnetic permeability of the vessel
ρ	Resistivity of vessel
C	Capacitor value
C_r	Resonant capacitor value
f_s	Switching frequency
I	current
i	current
i_o	High frequency current referred to IH coil side
I_{11}	High frequency supply current flowing through IH coil
I_{22}	Eddy currents generated in the vessel
L	Inductor value
L_f	Equivalent inductance of a FM vessel
L_{11}	Lumped inductance of IH coil
L_{22}	Lumped inductance of the vessel
L_{al}	Equivalent inductance of a aluminum vessel
L_{eq}	Equivalent inductance of IH load
L_{nf}	Equivalent inductance of a N-FM vessel
L_{st}	Equivalent inductance of a Steel vessel

M	Mutual inductance
N	Number of turns of IH coil
N_p	Number of turns of primary winding of transformer
N_s	Number of turns of secondary winding of transformer
R_f	Equivalent resistance of a FM vessel
R_{22}	Lumped resistance of the vessel
R_{al}	Equivalent resistance of a aluminum vessel
R_{eq}	Equivalent resistance of IH load
R_{nf}	Equivalent resistance of a N-FM vessel
R_{st}	Equivalent resistance of a Steel vessel
S	MOSFET Switch
T	Total time period of a control signal
t_d	dead time
v_o	High frequency supply voltage referred to IH coil side
V_{11}	High frequency voltage supply given to IH coil
V_{22}	Electromagnetically induced emf in the vessel
η	Efficiency of the inverter
ω_o	Resonant frequency
Ψ	Phase angle between ouput voltage and current
C_f	Filter capacitor
d	Duty cycle
I_o	Output Current
L_b	Boost inductor

L_f	Filter inductor
P_{con}	Conduction power loss
P_o	Output Power
P_{sw}	Switching power loss
Q	Quality factor of IH load
r_{DS}	MOSFET resistance across Drain and Source when it is ON
t_{on}	ON time period of switching devices
V_{AC}	AC supply voltage
V_{DC}	Input DC voltage source
V_{in}	Input supply voltage
V_o	Output Voltage

Chapter 1

Introduction

Chapter 1

Introduction

1.1 General

Global warming and increasing pollution levels have emerged as major challenges for humanity. To ensure sustainable future, United Nations (UN) has laid 17 sustainable development goals (SDGs). The primary focus of these goals is to ensure and promote sustainable technological development. Electrification plays a key role in achieving this aim. Induction heating (IH) has been identified as the most propitious technology for decarbonization. In IH, a high frequency supply is given to the IH coil which produces high frequency flux. This high frequency flux induces eddy currents in the work-piece to be heated as shown in Figure 1.1. IH technology offers several advantages as compared to the conventional heating methods.

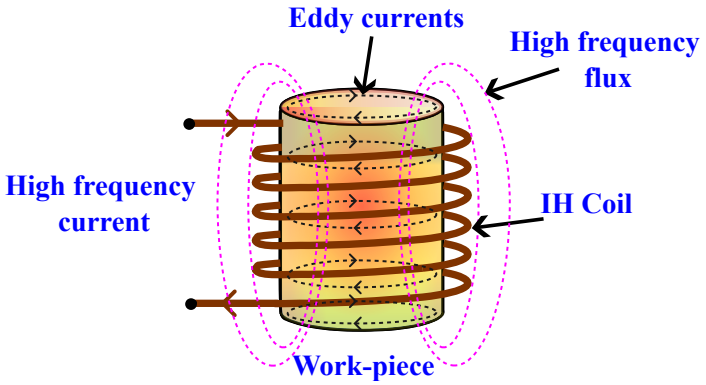

Figure 1.1: Induction heating

Key advantages of IH technology:

- It is a very clean technology as there is no emission of smoke, dirt, ash etc.
- It offers a safe heating solution as there are no open flames and heat is directly produced in the work-piece to be heated. It does not have any gas leakage issues which are common with conventional heating approach.

- The efficiency offered by IH system is high, typically more than 90%.
- It can be used for very high power generation as heat is directly produced in the work-piece while IH coil remains unheated.
- Due to high power operations, IH work-piece can be heated very fast.
- IH offers a very precise temperature control.

With the above mentioned advantages, IH technology also have some challenges and limitations which are listed below:

- IH load is a non-linear load. This results in drawing of non-sinusoidal currents from the power supply and hence injects harmonics in the power supply. This may lead to interference with communication lines, protective device failure and audible noise from transformer.
- As IH load is inductive in nature, it will lead to poor power factor.
- Output power is dependent on the type of IH load material.

To overcome the above mentioned limitations, several solutions are presented in the past with different control techniques and inverter topologies which are described in Chapter2 of the thesis. There are multiple applications of IH technology. Some of the common heating applications through IH are cooking, surface hardening, melting of metals, annealing, forging, cap sealing, etc. Overview of industrial and domestic IH applications is described in the following sections.

1.2 Overview of Industrial Applications of Induction Heating

The industrial applications of IH technology can be categorized mainly into induction bonding, induction forging, induction melting and induction thermal treatment of metals. Bonding of metals is done in different applications such as brazing, shrink fitting, welding and heat sealing. Induction brazing uses a filler metal with lower melting point than that of metals that are to be joined. A very precise control of heat is required for this application, which is realised by using IH. It is commonly used in automotive, electro-mechanical and electric motor industries. Shrink fitting find applications in gear pinions, couplings, electric motor shafts and discs for motor and turbine. It requires complete control over area to be heated. With induction shrink fitting, heat can be generated precisely on any desired area and it makes the shrinking operation fast and accurate. It minimizes the risk of deformation by protecting the parts from over stress. Induction welding is used for joining pipes, tubes and other closed profiles. It offers

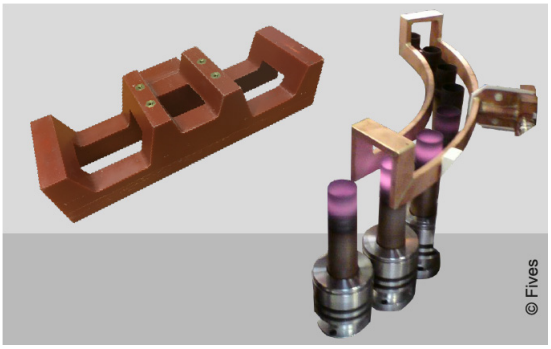

(a) Brazing

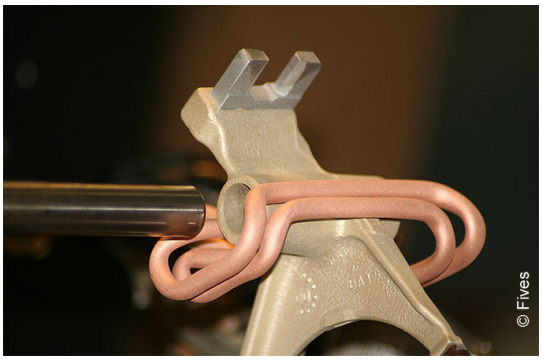

(b) Shrink fitting

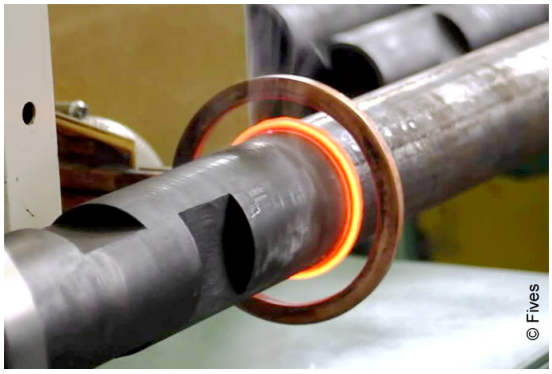

(c) Induction welding

(d) Heat sealing

Figure 1.2: Bonding of metals using IH. *Courtesy Fivesgroup*.

(a) (b)

Figure 1.3: Induction forging. *Courtesy Fivesgroup*.

high efficiency. IH is also used for sealing different products such as food, pharmaceutical etc. The images showing different industrial bonding techniques are presented in Figure 1.2.

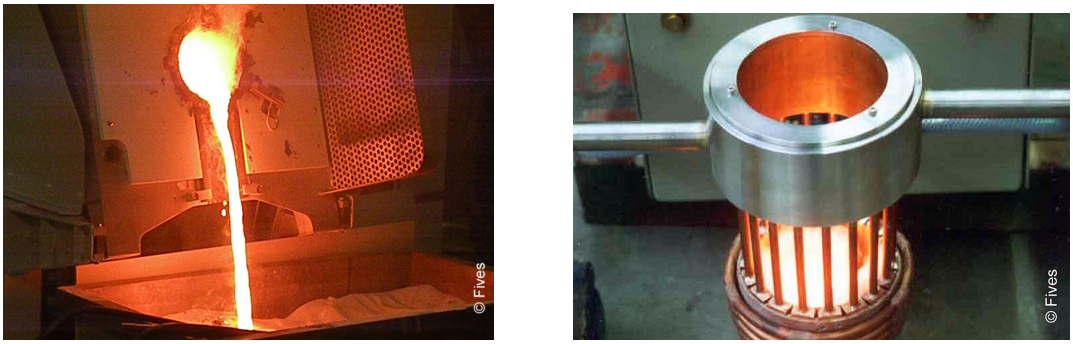

(a) Hot crucible (b) Cold crucible

Figure 1.4: Induction melting. *Courtesy Fivesgroup*.

Induction forging heats the metals prior to forming. It can selectively heat the metal part which is being shaped. And no energy is lost in heating other parts which do not need forming. It increases the efficiency and also ensures integrity without compromising metal quality. The images showing industrial induction forging are presented in Figure 1.3. Induction melting is used for producing homogeneous mixture by fast and controlled melting of materials. Homogeneity of the mixture is ensured by automatic stirring with the help of electromagnetic field. This is mainly categorized into hot crucible induction melting and cold crucible induction melting. In hot crucible induction melting, crucible is being heated to melt variety of metals. Whereas in cold crucible induction heating, crucible remains cold while heat is directly produced in the material to be melted. Cold crucible induction melting is used for corrosive or reactive materials. It is ideal for treatment of very high purity metals as it naturally prevents the contamination of material by preventing deterioration of crucible. Images of hot and cold crucible induction melting for industrial applications are shown in Figure 1.4.

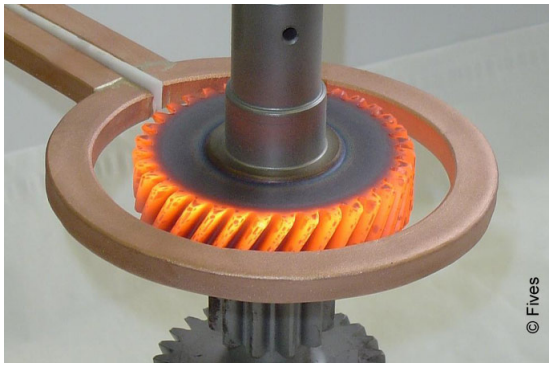

(a) Annealing

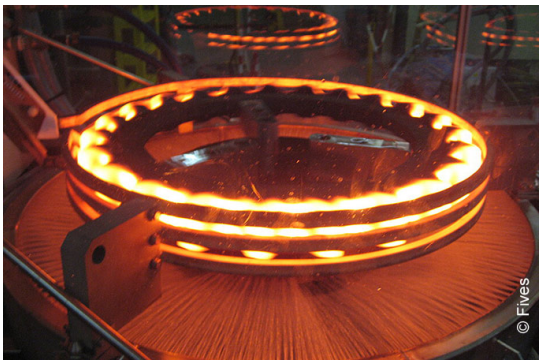

(b) Quenching

(c) Tempering

Figure 1.5: Thermal treatment using IH. *Courtesy Fivesgroup*.

IH is also used for thermal treatment of the materials. Annealing is used for treating highly processed metals. It softens the metal, reduces the internal stress and improves the ductility of the metal. Quenching is used for modifying mechanical characteristics of the metal or a portion of the metal. It helps in improving the hardness of the material. After quenching, tempering is done for internal mechanical stress relief. It helps in making material strong. The industrial examples of thermal treatment are shown in Figure 1.5.

1.3 Overview of Domestic Induction Heating

Traditionally, for domestic cooking applications, heat is generated by burning natural resources such as coal, petrol, wood etc. These conventional heating methods are less efficient, increases pollution, not safe and do not offer controllable heating. Whereas, induction cookers offer multiple advantages over traditional approach. Some of the key advantages are high efficiency, quick heating, controllable heating, safety and cleanliness. With these advantages, induction cookers have gained popularity in consumer domestic appliance market. In IH, available low frequency utility supply (50/60 Hz) is converted into high frequency (20-30 kHz)

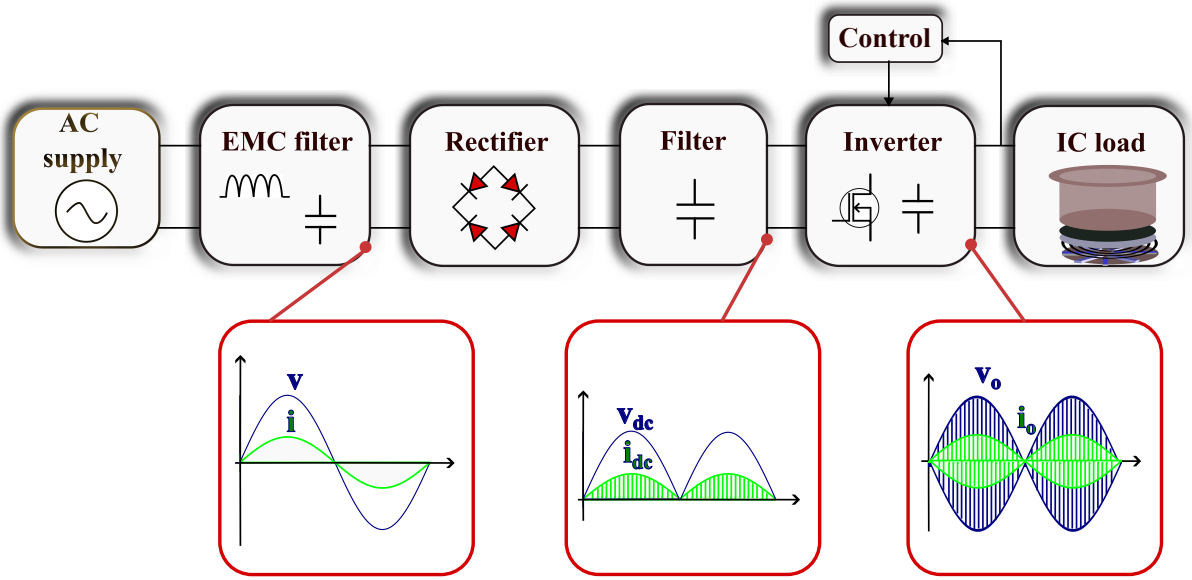

Figure 1.6: Power conversion stage and typical voltage-current waveforms for IC system.

voltage supply. The typical power conversion stages with respective voltage-current waveforms are presented in Figure 1.6. The high frequency supply produces high frequency flux which generates eddy currents at a skin depth (δ) from the vessel surface and it can be given as

$$\delta = \sqrt{\frac{\rho}{\pi \mu f_s}} \tag{1.1}$$

where ρ is resistivity and μ is magnetic permeability of the vessel material to be heated. And f_s is the switching frequency of inverter. Due to these eddy currents, ohmic losses will occur in the vessel. These losses will produce heat in it. As heat is directly produced in the vessel, IH systems operates at very high efficiency. The electrical output power to the vessel is expressed as

$$P = (NI)^2 \sqrt{\rho \mu \pi f_s} \tag{1.2}$$

Where, 'N' is the number of turns of induction heating coil and 'I' is the rms current flowing through it.

The exploded view of a typical induction cooker and its equivalent circuit diagram is shown in Figure 1.7. Figure 1.7(a) shows the generalised induction cooker in detail. Vitroceramic glass and isolator is used to physically separate the coil and other electrical components from corrosive kitchen environment. It also helps in preventing it from heat of the vessel. Electrical isolation is ensured by keeping an isolator. Shielding and ferrites are kept below the IH coil to minimize the radiated flux and to improve the magnetic coupling between the vessel and IH coil [1]. The equivalent electrical modelling of induction cooker is presented in Fig-

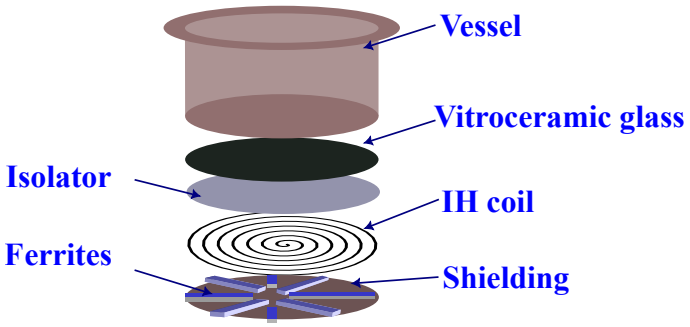

(a) Induction cooker system detail

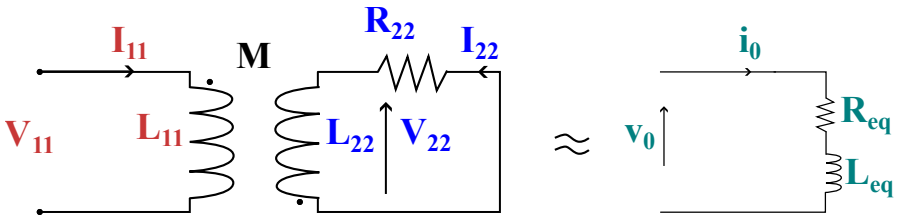

(b) Electrical equivalent circuit of induction cooker

Figure 1.7: Induction cooker coil arrangement and its electrical equivalent circuit.

Table 1.1: Characteristic of IH load materials at 20 kHz

Parameter	Iron	Aluminum
Resistivity	$9.8 \times 10^{-8} \Omega m$	$2.5 \times 10^{-8} \Omega m$
Relative permeability	100	1
Skin depth	0.11 mm	0.56 mm
Surface resistance	$8.8 \times 10^{-4} \Omega$	$0.45 \times 10^{-4} \Omega$

ure 1.7(b). The induction coil and the vessel to be heated can be represented by a transformer model by considering their lumped electrical parameters. The primary of the transformer represents n-turn induction coil. V_{11} is the high frequency voltage supply given to the IH coil. And I_{11} is the high frequency supply current flowing through the IH coil. L_{11} represents the lumped inductance of the IH coil. The transformer secondary side represents the vessel. The vessel to be heated is modelled by a single turn coil whose ends are shorted. It can be modelled as a combination of R_{22} and L_{22}. Where, R_{22} is the lumped resistance of the vessel and L_{22} is the lumped inductance of the vessel. V_{22} represents the electromagnetically induced emf and I_{22} represents the eddy currents generated in the vessel. Finally, by referring all the parameters to the primary side, IH load (vessel) can be modelled as a series combination of resistance (R_{eq}) and inductance (L_{eq}). v_0 and i_0 represents the high frequency supply voltage supply and IH load current referred to coil side respectively. Different IH coils available in the market are presented in Figure 1.8.

Figure 1.8: Different size induction coils used in the domestic market [1].

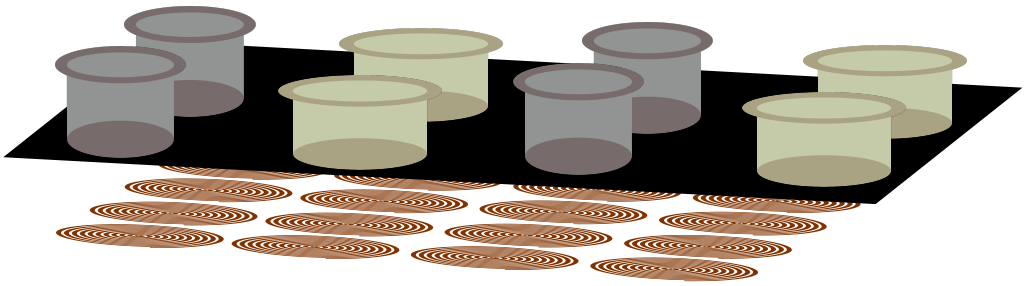

Figure 1.9: Multiple load induction cooking system.

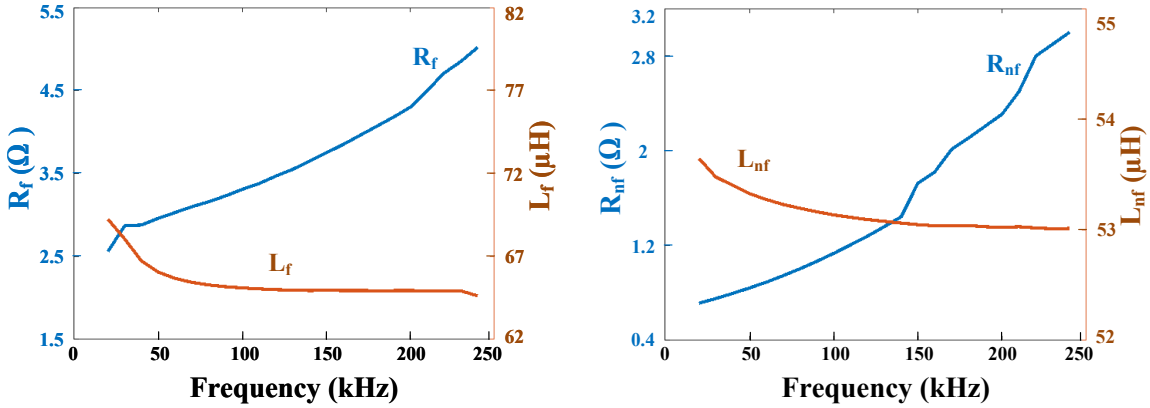

(a) FM steel load

(b) N-FM aluminum load

Figure 1.10: IC load characteristics with frequency

Heating multiple vessels at a time with an independent control is a common requirement of induction cooking system (ICS). The multiple load ICS is presented in Figure 1.9. The typical characteristic of ferromagnetic (FM) and non-ferromagnetic (N-FM) materials at 20 kHz operation is given in Table 1.1. Iron and aluminum vessels are considered as FM and N-FM IH loads respectively. It can be observed that FM material vessels offer high resistance and high relative permeability at operating frequency of 20 kHz. So, these can be easily heated (powered) by operating in 20-30 kHz. Whereas, N-FM vessels offer low resistivity and low relative permeability at 20 kHz. So, the current requirement for powering these vessels will be very high. In order to power at 1 kW, nearly 150 A rms current is required which is unreasonable. But these load parameters are dependent on operating frequency. The variation of parameters of FM and N-FM loads with frequency is plotted in Figure 1.10. Figure 1.10(a) shows the FM steel load parameter variation over frequency. R_f and L_f are respectively resistance and inductance of the FM steel load. Figure 1.10(b) shows the N-FM aluminum load parameter variation over frequency. R_{nf} and L_{nf} are respectively resistance and inductance of the N-FM aluminum load. It can be observed that the resistances of both the loads increases with the operating frequency. N-FM load resistance is very low at 20-30 kHz frequency range. But at frequencies higher than 100 kHz, it offers a significant resistance. Hence, higher frequency operation is preferred for heating N-FM loads.

1.4 Motivation

From the literature review of different inverter topologies for IH application, the following major observations are drawn:

- Most of the inverter topologies available in the literature are suitable only for single IH load application.
- Only some of the inverter topologies available in the literature are capable to power multiple IH loads with simultaneous and independent control.
- Many of the multiple IH load inverter topologies use electro-menchanical switches.
- Only few of the multiple IH load inverter topologies are capable of providing simultaneous as well as independent power control for different material IH loads.

These inverter topologies suffer one or many of the following limitations:

- High component count
- Use of electro-mechanical switches

- Lack of simultaneous as well as independent power control
- Not suitable for heating vessels of different materials
- Lack of soft-switching

Hence, there is an enough scope for further research in the area of multiple load IH application for different material IH loads.

1.5 Thesis Objectives

The research work focuses on the design of the resonant inverter topologies for multiple load IH applications with following features:

[i] Powering multiple IH loads.

[ii] Simultaneous and independent power control of IH loads.

[iii] Suitability for different material IH loads.

[iv] High efficiency.

[v] Low component count.

[vi] Soft-switching.

1.6 Contribution

The main contributions of the research work are discussed below:

[I] Three Switch Resonant Inverter for Multiple Load Induction Cooking Application.
This inverter configuration is provides a feasible solution for multiple load IH application. The key advantages of the proposed inverter are as below:

- Reduced switch to load ratio for multiple ferromagnetic IH load control
- Simultaneous and independent control of IH loads with simple asymmetrical duty cycle control technique
- High efficiency (96.3%)
- Soft-switching operation during both turn-ON and turn-OFF

Hence, the proposed three switch inverter is suitable for multiple load IH application. It can also be extended for more loads by adding another three switches per two loads. The extended topology can be used for heating vessels of different materials.

[II] Full-bridge Based Multi-load Inverter Configuration for Vessels of Different Material Induction Cooking Application.
This inverter provides a feasible solution for different material multiple load IH applications. Following are the key advantages of the proposed inverter:

- Simple control
- Simultaneous and independent control of different material IH loads
- Easy extension for multiple IH loads application
- Soft-switching during turn-ON of switching devices
- High efficiency (94.3%)

Hence, the proposed inverter configuration is suitable for multiple different material IH load application.

[III] Three Switch Dual Frequency Resonant Inverter for Different Material Induction Cooking Application.
This inverter provides a feasible solution for different material multiple load IH applications. Following are the key advantages of the proposed inverter:

- Reduced switch count for heating two IH loads of different materials
- Simultaneous and independent control of different material IH loads
- Soft-switching operation during turn-ON
- High efficiency (96.11%)

Hence, the proposed three switch dual frequency resonant inverter is suitable for powering two different material IH loads.

[IV] Dual Half-bridge Resonant Inverter for Different Material Induction Cooking Application.
This inverter provides a feasible solution for different material multiple load IH applications. Following are the key advantages of the proposed inverter:

- Reduced component count
- Removal of lossy split capacitor arrangement
- Simultaneous and independent control of different material IH loads
- Soft switching operation during turn-ON

- High efficiency(97.38%)

Hence, the proposed inverter offers a compact solution for powering two IH loads of different materials.

1.7 Thesis Organization

The thesis has been organized into seven chapters.

Chapter 1 briefly introduces the principle of induction heating and its applications. Industrial and domestic applications of induction heating technology are discussed in detail. It provides a brief description of the work done and the chapter wise summary of the thesis.

Chapter 2 presents a comprehensive literature review on existing inverter topologies and control techniques for IH applications. This sets the motivation carried out in this thesis.

Chapter 3 describes the analysis and implementation of the proposed three switch resonant inverter for induction heating application. The circuit operation, analysis and design procedure are presented. Independent power control is achieved by using ADC control technique. Simulation and experimental results for the proposed inverter are presented.

Chapter 4 details the analysis and implementation of the proposed resonant inverter for different material multiple load induction heating application. The circuit operation, analysis and design procedure are presented. Independent power control is achieved by using ON-OFF control technique. Simulation and experimental results for the proposed inverter are presented.

Chapter 5 describes the analysis and implementation of the proposed dual frequency resonant inverter for induction heating application. The circuit operation, analysis and design procedure are presented. Duty cycle and frequency based controls are discussed in detail. Simulation and experimental results for the proposed inverter are presented.

Chapter 6 describes the analysis and implementation of the proposed series resonant inverter for induction heating application. The circuit operation, analysis and design procedure are presented. Duty cycle and frequency based controls are discussed in detail. Simulation and experimental results for the proposed inverter are presented.

Chapter 7 concludes the thesis which highlights the main findings of the research work reported in this thesis and suggests scope for future work.

Chapter 2

Literature Review

Chapter 2

Literature Review

2.1 Introduction

This chapter presents the overview of inverter topologies and different control techniques available in the literature for induction heating applications. Merits and limitations of these topologies and control techniques are also discussed.

2.1.1 Commonly used topologies and control techniques

A typical induction heating system layout is presented in Figure 2.1. It consists of an electromagnetic compatibility (EMC) filter, rectifier, capacitor filter, inverter with control and an induction cooking load. A small value of capacitive filter is used after rectification which does not affect the input power factor. The rectified and filtered voltage is supplied to the inverter. In the literature, the most commonly used inverter configurations for induction heating applications are typically of three types: single switch inverter, half-bridge inverter and full-bridge inverter. Single switch inverter is used up to 2 kW power rating. Half-bridge inverter is used for powering IH load up to 5 kW rating. For powering more than 5 kW, full-bridge inverter is used. These commonly used inverter topologies are presented in Figure 2.2.

For power control in IH load, various control techniques have been proposed in the literature. The most commonly used control techniques are phase-shift control (PSC), asymmetrical duty cycle control (ADC), asymmetrical voltage cancellation control (AVC) and square wave

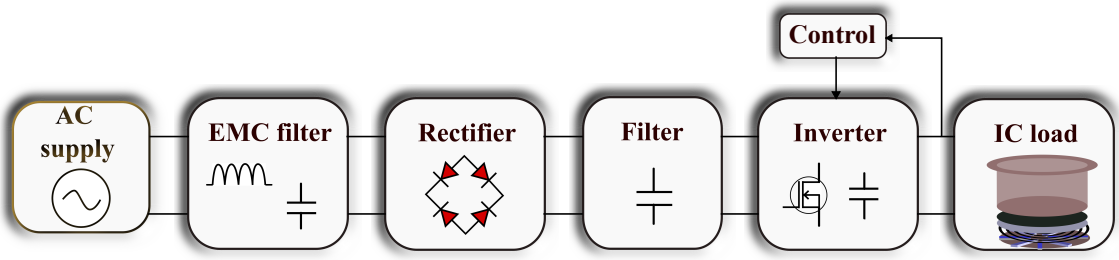

Figure 2.1: Typical induction heating system layout

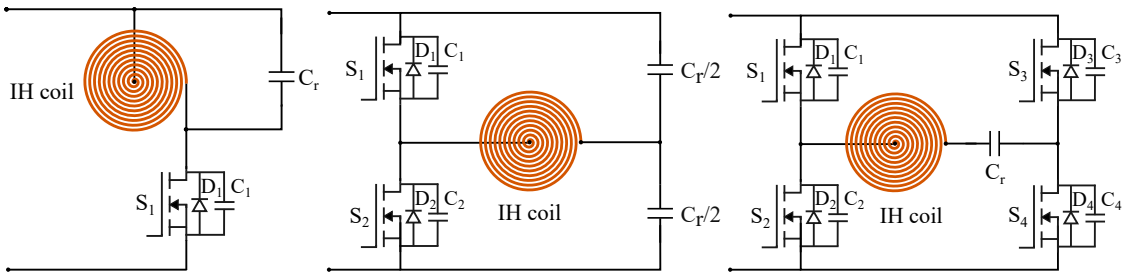

(a) Single switch (b) Half-bridge (c) Full-bridge

Figure 2.2: Commonly used inverter topologies for IH application

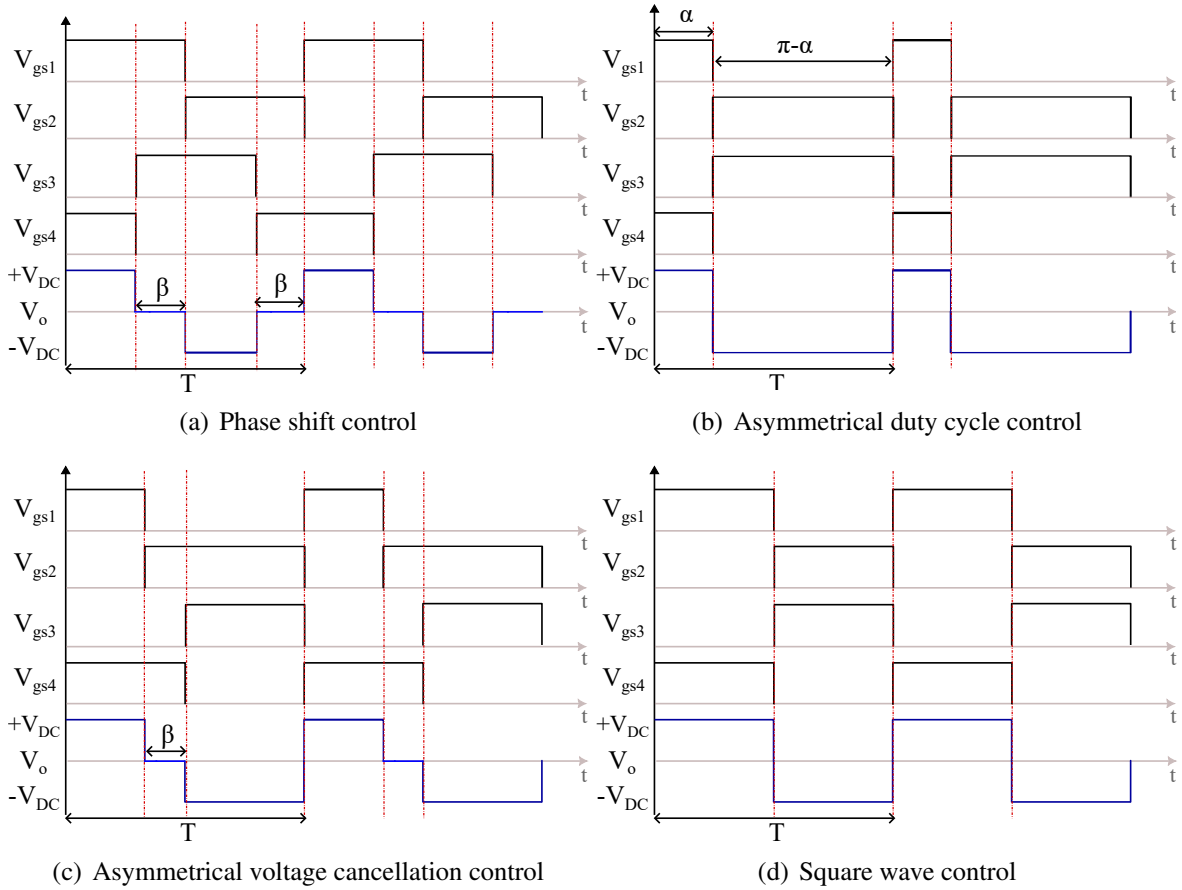

(a) Phase shift control (b) Asymmetrical duty cycle control

(c) Asymmetrical voltage cancellation control (d) Square wave control

Figure 2.3: Commonly used control techniques in IH application

based control techniques. These techniques can be categorised in to variable frequency control and constant frequency control. In variable frequency control as shown in Figure 2.3(d), the operating frequency of the inverter is varied for a constant resonant frequency of IH load. This affects the soft-switching and the load impedance. In constant frequency based control, the operating frequency of the inverter is fixed and the duty cycle is varied to control power in IH load. PSC, ADC, AVC and pulse density modulation (PDM) control technique are constant frequency based control techniques. In phase-shift control as shown in Figure 2.3(a), by controlling the phase-shift in the two inverter leg pulses, symmetrical output voltage is obtained. It gives a wider power control. But the zero voltage switching of the inverter devices at lower duty cycle gets affected. In asymmetrical duty cycle control as shown in Figure 2.3(b), duty cycle is varied in an asymmetrical manner and hence the IH load is also fed with an asymmetric voltage. For lower duty cycles, it offers a better power control range with ZVS when compared to that of phase-shift control. In asymmetrical voltage cancellation technique as shown in Figure 2.3(c), one inverter leg is controlled with respect to other leg. Hence, the inverter output voltage is varied only in positive half cycle. The AVC control provides better ZVS range when compared to PSC and ADC control techniques. In pulse density modulation control, the average power is controlled by turning ON and OFF inverter output square wave voltage pulses. Hybrid control techniques by combining some of these techniques are also used in the literature to get best performance of the inverter.

2.2 DC-AC Topologies

This section details various inverter topologies proposed in the literature with DC based supply. From utility supply, a DC supply is obtained with the help of a rectifier unit and a filter capacitor and then it is fed to the inverter circuit. These topologies are further categorised into single load, multiple load and different material IH load topologies. The detailed description of different inverter topologies available in the literature is presented below:

2.2.1 Single load inverter topologies

A single ended half bridge topology along with auxiliary resonant circuit is proposed in [2]. Figure 2.4 shows the proposed single ended HB topology. Additional third switch is connected in parallel with the high side switch of half-bridge. This ensures ZVS and ZCS during switching of high side switch of half-bridge. Hence, switching losses are reduced and efficiency is improved. But this suffers with the restriction on minimum power control. It also increases the component count and hence the cost of the system.

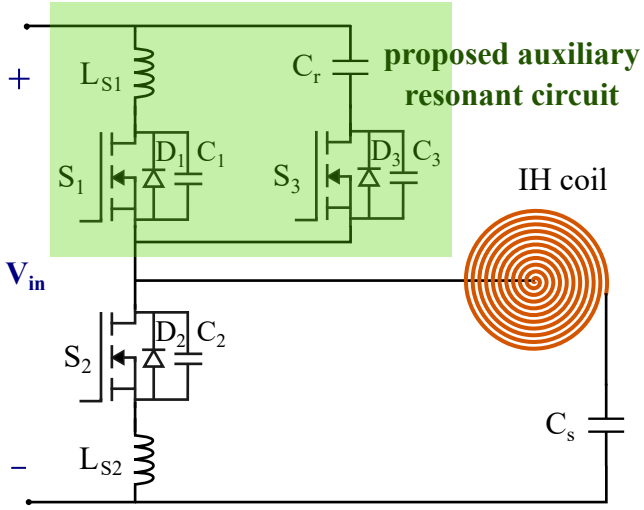

Figure 2.4: Single ended HB topology [2]

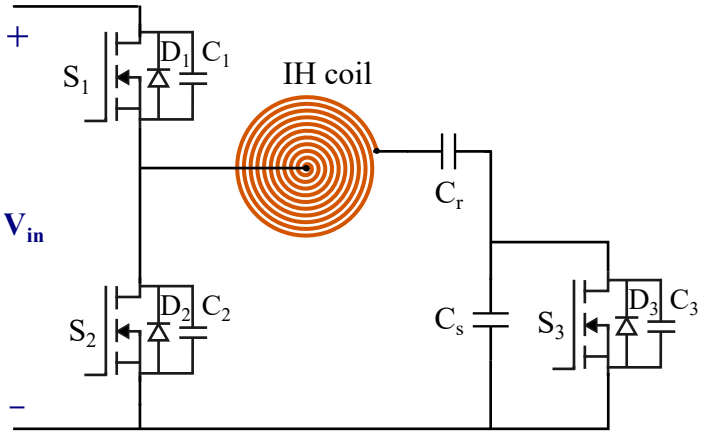

Figure 2.5: Half bridge based resonant inverter with high power density [3]

In [3], a capacitor and switch is used along with the HB topology to increase the power density of inverter. The proposed topology is depicted in Figure 2.5. Energy is stored in the capacitor and then dissipated through the IH load. However this makes the load current discontinuous and affects the soft switching operation of the inverter which will ultimately leads to low efficiency.

In [4], class-D and class-DE modes of half-bridge inverter operation are combined to power an IH load. When class-E mode conditions are achieved along with ZVS and zero voltage derivative switching, it is called as class-DE mode of operation. Class-D mode is used for high power operation while class-DE mode is used for medium to low power operation. Two sets of snubber capacitors and resonant capacitors are used for this dual mode operation. This approach increases the efficiency of the system but suffers with increased component count. Also, use of electro-mechanical switches may cause electromagnetic interference.

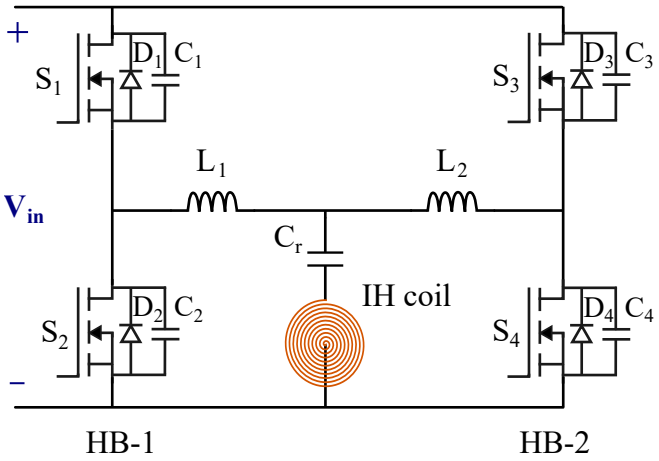

Figure 2.6: Two HB based resonant inverter with phase-shift control [5]

IH load is controlled by current phase control in [5]. The proposed inverter is depicted in Figure 2.6. Phase-shift between two HB units is changed. This widens the soft-switching range for the switching devices. Also, for low power operation, asymmetrical PWM and phase-shift angle control are implemented. This improves the overall efficiency when compared to conventional approach but suffers with increased component count.

When IH load is changed, the inverter operation also gets affected. In order to overcome this, a HB based load adaptive modulation (LAM) technique is proposed in [6]. Frequency limit and power level algorithms are incorporated. Power level algorithm operates with better efficiency at low and medium power operation whereas frequency limit algorithm operates with low flicker. Both the algorithms are based on square wave and pulse density modulation.

In [7], an enhanced pulse density modulation (EPWM) scheme for high frequency IH inverters is proposed. Conventional PDM scheme suffers with output current ripples when operated with low quality factor loads or at low power mode. This can increase the losses and may lead to lack of control. This has been overcome by incorporating new EPDM control. With EPDM, the output current ripple reduces by 50% and inverter performance also improved in terms of accurate frequency tracking and efficiency.

A technique for monitoring different operating conditions of an IH resonant power converter is proposed in [8]. The resonant capacitor voltage is sampled at a low frequency. Based on that information, input voltage, output power and soft-switching conditions of the resonant power converter are measured.

In [9], a multiple frequency inverter is proposed. The proposed inverter is shown in Figure 2.7. It uses a center tapped capacitor and split capacitor arrangement along with the FB topology. IH load is connected at the output of the transformer. The operating frequency of the switches remains half than that of the transformer output frequency. The switches also

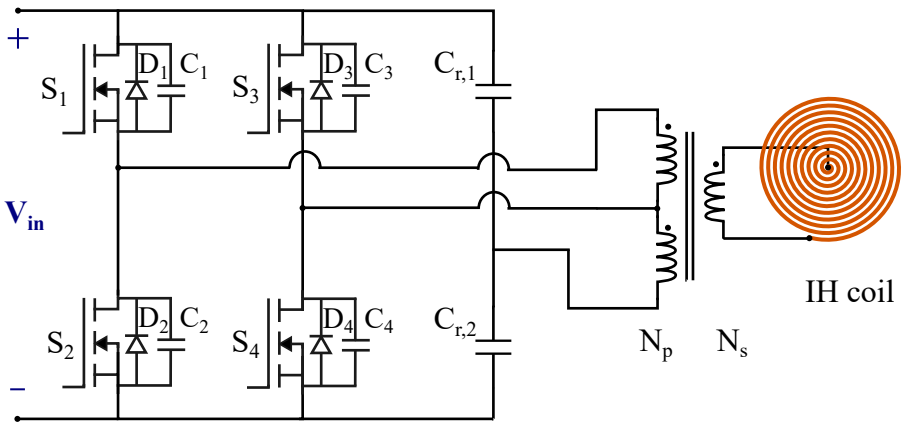

Figure 2.7: Multi-frequency inverter [9]

operate with zero voltage during turn-ON. However, the component count is increased with this approach which makes the system bulky and costly.

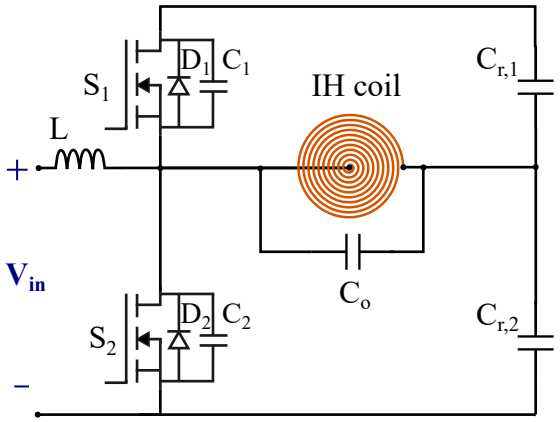

Figure 2.8: HB inverter with boosting stage [10]

In [10], boost converter and HB inverter is combined to increase the output voltage and power of IH load. Boosting and half bridge zero voltage switching is obtained with two switches as depicted in Figure 2.8. The efficiency of the system is less for low power but increases as the operating power is increased.

In [11], previously proposed inverter [10] is modified and an AC input based converter along with a boosting stage is proposed. Figure 2.9 shows the modified inverter. It uses a rectification stage. Boosting and high frequency inversion stages are combined using a HB topology. The performance of the previously proposed inverter is improved for low power operation by using dual mode control scheme i.e., asymmetrical PWM and PDM control.

In [12], an online parameter estimation method for variable IH load is proposed. The algorithm is designed only for ferromagnetic type materials. It turns off the power when non-ferromagnetic material vessel is placed on the cooktop. Parameter variation of IH load based

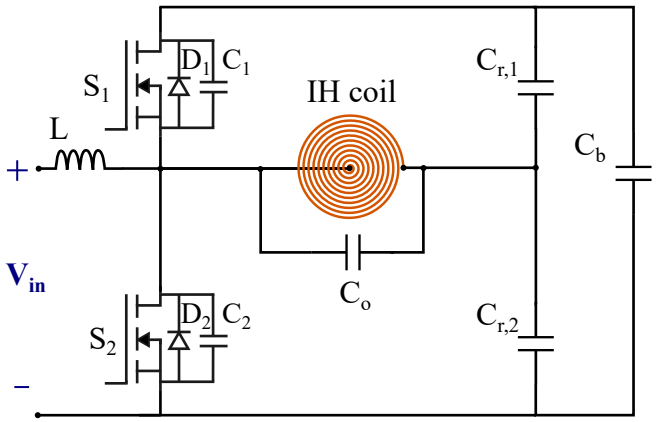

Figure 2.9: HB inverter with boosting stage [11]

on frequency and equivalent heating coverage rate is studied. It is observed that inductance of IH load remains almost constant while resistance of IH load varies significantly. The resistance and inductance of IH load is estimated by measuring resonant current value at the beginning of resonant period, peak value of resonant current during negative half cycle and zero crossing time in the begining of negative half cycle. The estimation is carried out at every 10 ms.

A multi-MOSFET cell is incorporated in classical HB topology [13]. High side and low side devices in half bridge are replaced with three MOSFETs. This reduces the drain-source resistance when compared to the classical HB approach with IGBTs. Hence, conduction losses are also reduced. High switching frequencies of MOSFETs also reduces the switching losses. Hence, overall efficiency of the system will increase. But this suffers with increased component count and design complexity.

In [14], concept of inductive power transfer is combined with conventional IH approach for heating small loads with more distance from the IH coil. This leads to heating of vessels without using conventional glass in between the vessel and the coil. The vessel is directly mounted on the kitchen surface, with an additional secondary inductor coil with series capacitor. This presents a good solution for heating cookware at a high distance but it suffers with increased design complexity.

An FPGA based gain controller for variable load IH system is proposed in [15]. It uses modulation parameter information and online estimation of IH load identification. It improves the dynamic performance of the total system and ensures safe inverter operation.

Phase shifted PWM technique along with pulse frequency modulation for IH system is implemented in [16]. Phase shifted PWM technique is used for regulation of the output power. Pulse frequency control is used simultaneously for soft switching during dynamic IH load conditions. This hybrid control is implemented using FPGA.

2.2.2 Multiple load inverter topologies

In the literature, inverter topologies are also available to power more than one load at a time.

In [17], operating principle of multi-load IH system for low power applications is studied. The proposed single inverter multi-load IH system solution is shown in Figure 2.10. It uses one master and one slave IH load. Master load operates with fixed capacitance while slave load power is varied using capacitor switching. This solution uses three electro-mechanical switches and three resonant capacitors.

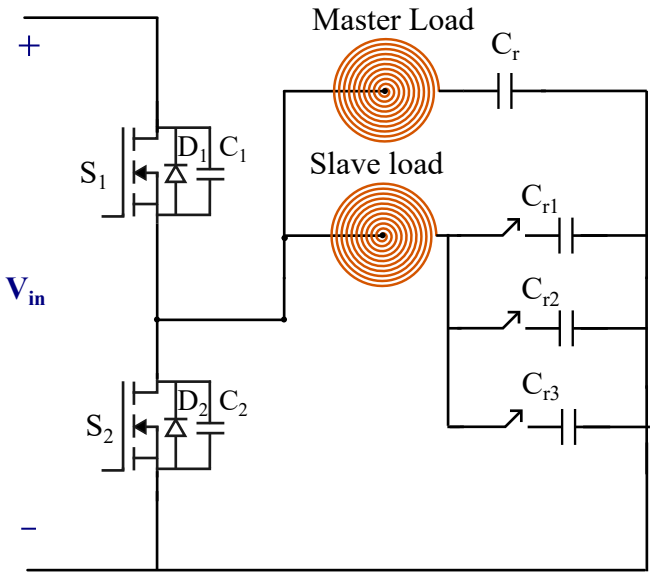

Figure 2.10: HB based multi-load IH system [17]

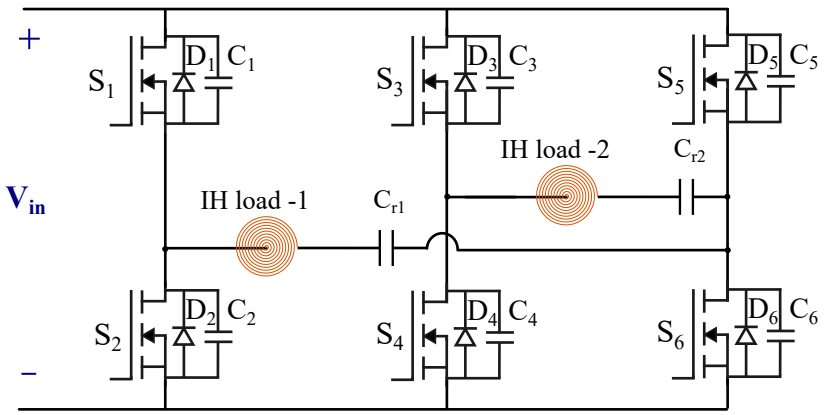

Figure 2.11: Three leg inverter for two load IH system [18]

In [18], a three leg inverter is used to control two IH loads. The proposed three leg inverter is as shown in Figure 2.11. Two loads are simultaneously as well as independently

controlled with AVC technique. This is a simple approach but it suffers with restrictions on ZVS due to AVC control.

In [19], buck converter and HB inverter topology are combined and a solution for multiple IH loads is proposed. The performance of the proposed topology is investigated under mutual magnetic coupling conditions among different IH coils. A new current phase control is proposed for a wider power range regulation in IH loads. This solution is suggested for semiconductor processing industry.

In [20], power factor correction rectifier is proposed for multiple HB resonant inverter based multi-output IH system. Its operation in HB, FB and hybrid mode is analysed. Hybrid mode of operation (HB and FB both) for power factor correction is chosen for better input current profile.

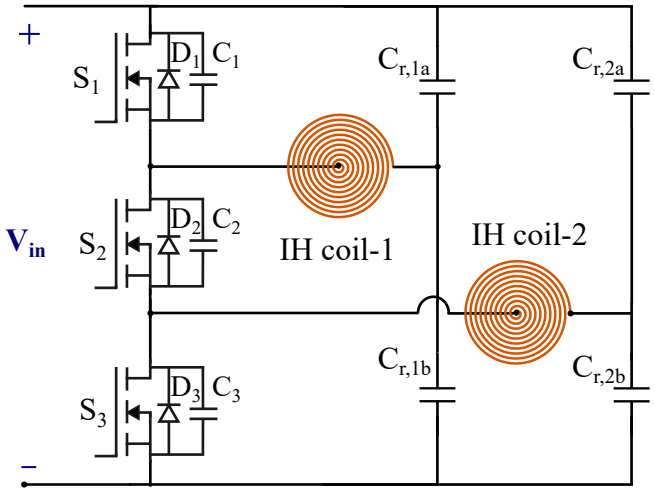

Figure 2.12: Three switches series-resonant half-bridge [21]

In [21], two IH loads are controlled by using three switches. The proposed inverter is depicted in Figure 2.12. With top high side switch ON, other two switches are alternately driven to power one IH load. Similarly, with low side switch ON, other two switches are alternately driven to power other IH load. In this, power control is not completely independent. To obtain independent power control, two different frequency operation is used which leads to increase in control complexity.

In [22], a cyclic load control with three leg inverter for three IH loads is proposed. The proposed inverter is as shown in Figure 2.13. Three loads are simultaneously and independently controlled by using the proposed control technique. Different control intervals are pre-calculated based on the power requirement of each IH load and then the control is realised. It offers a wider ZVS operating range. It uses a simple control for three load IH application. However, for more than three loads, the control complexity will be increased.

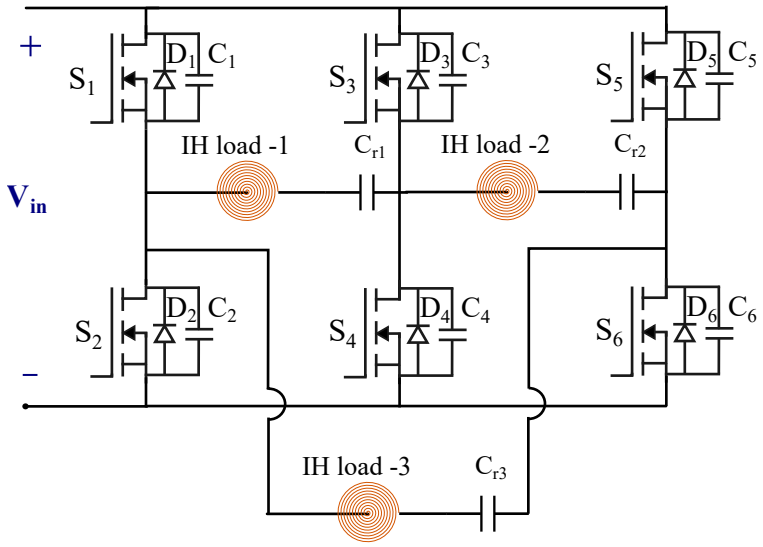

Figure 2.13: Three leg inverter with cyclic control [22]

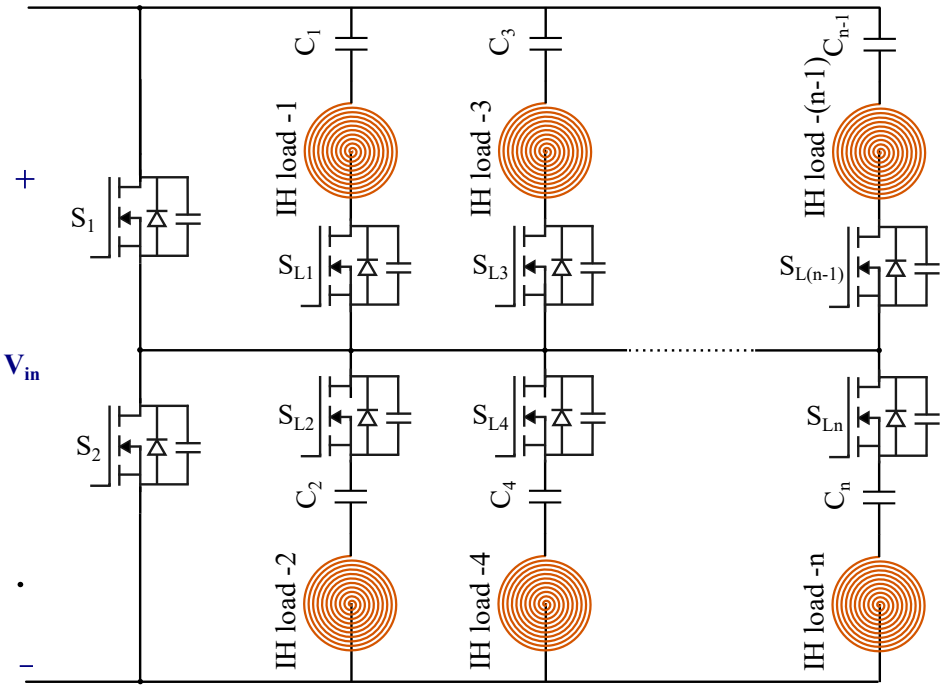

Figure 2.14: HB based multi-inverter topology [23]

In [23], a HB based multi-inverter topology is proposed for multiple loads. An IH load with a series switch is added in parallel to high side and low side switches of HB inverter as shown in Figure 2.14. Each IH load is independently controlled by using PDM technique. This topology has low power handling per converter, low switching device count and better controllability when compared with a classical multiple HB topology for IH application. But the conduction losses in this topology is more. Also, the disconnection of the series IH load results in the voltage spike across the switch due to residual resonant capacitor voltage. In

order to overcome this, a soft-stop control with optimal trajectory is proposed in [24]. With this technique, ON period of common inverter switch is reduced before load disconnection. This will lead to reduction or elimination of the capacitor voltage.

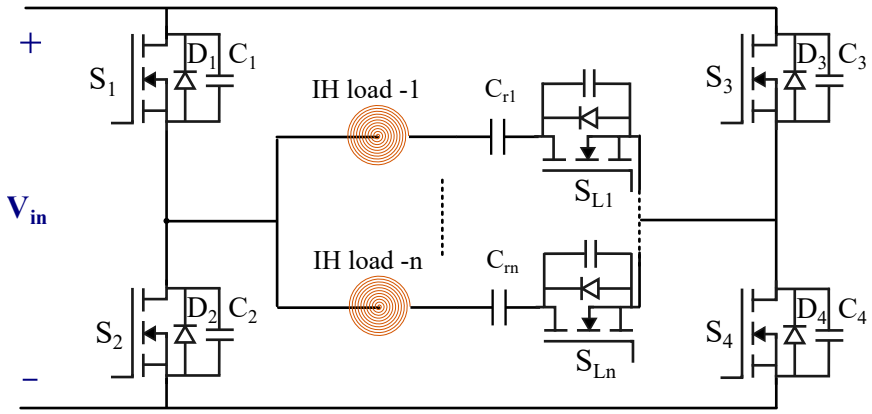

Figure 2.15: FB based multi-load IH system [25]

In [25], a SiC MOSFET based solution for IH is evaluated. The proposed FB based multi-load IH system is as shown in Figure 2.15. It uses a single switch per IH load. Each load is controlled by means of ON-OFF control. The device count and complexity are less for this configuration. Also, it can also be extended for multiple loads by a simple addition of a series switch per additional load. However, it suffers with the limitation on power control as the series switch with IH load can not be turned off until the current is zero.

A multi coil IH system for wireless electric iron is investigated in [26]. A cord less electric iron by using wireless power transfer principle of IH is proposed. The developed prototype gives a uniform heating over the entire electric iron surface.

A non-planar inductor system for flexible surface ICS is proposed in [27]. It uses conventional HB topology for multiple loads. The design of non-planar inductor system is complex.

In [28], a multi-phase series resonant inverter for multiple loads is proposed. It uses multiple vertically aligned and mutually coupled coils for heating multiple IH loads. For multi-load IH system, 'n' number of HBs are used. For power regulation, phase-shift control and duty cycle modulation are implemented. Design of the system is complicated.

In [29], deep learning algorithm based magnetic coupling detection for multi-coil flexible surface heating application is proposed. For multiple load ICS, the algorithm determines the area of overlap between coils and vessel irrespective of its size. Data for neural network is generated by using data augmentation method. The training of convolutional neural netwok is very complex. And with ageing, these neural networks are to be trained again which is not feasible in IH application.

A matrix type inverter as shown in Figure 2.16, is presented in [30]. It can power multiple

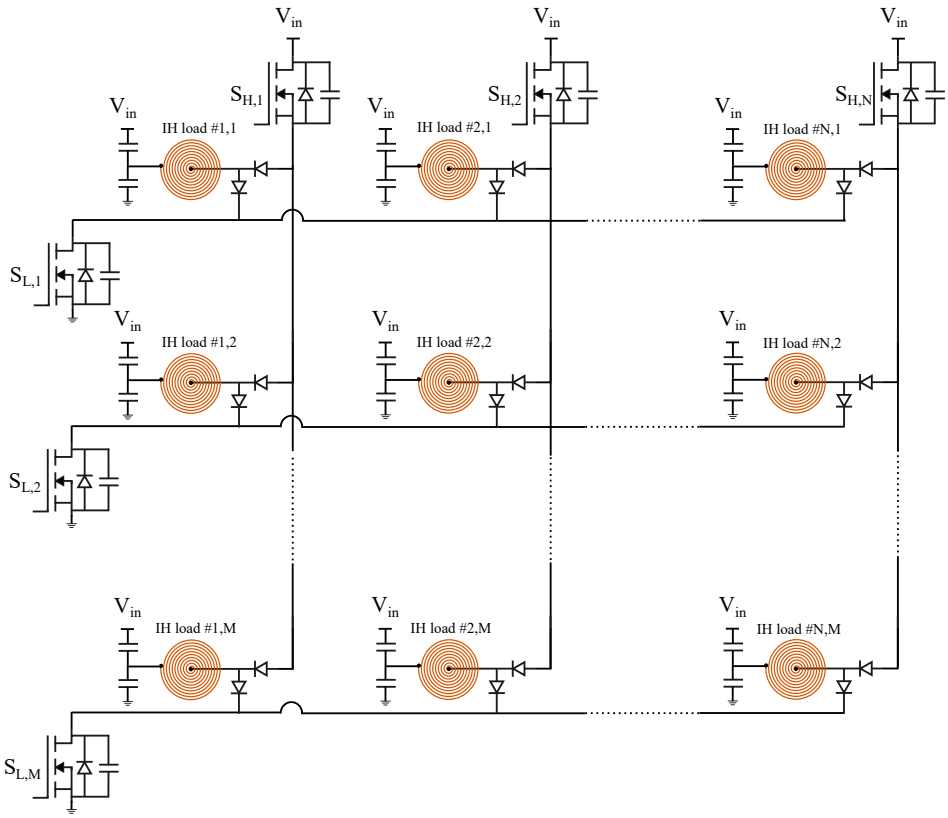

Figure 2.16: A matrix inverter for IH application [30]

loads with reduced power device count. Each IH load is connected with two diodes in a matrix arrangement. Where each load can be powered independently based on the switching state of a row and a column switching device. However, the amount of power control is restricted as complete independent and simultaneous power control is not possible. In [31], same matrix type series resonant inverter with asymmetrical modulation technique is proposed. The equivalent AC resistance seen from the mains varies with the supply. Hence, the input current profile gets affected which leads to low power factor. This problem is overcome using asymmetrical non-complimentary PWM control technique. But this may affect the ZVS operating range.

In [32], PDM technique is applied to the same matrix topology and its performance for multi-load output application is studied. The algorithm for ZVS operation of pre-selected IH coils is implemented.

2.2.3 Different material load inverter topologies

In the literature, some inverter topologies have been proposed for different material induction heating.

An inverter configuration which is suitable for FM and N-FM IH loads with load detec-

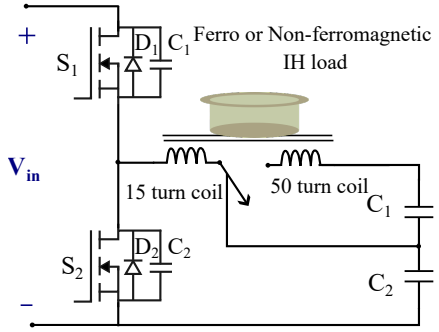

Figure 2.17: HB based all-metal IH solution [33]

tion control in [33]. The proposed HB based all-metal IH solution is depicted in Figure 2.17. By varying number of turns of coil, different material vessels were heated. The prototype weight is 10 kg. And hence it is a bulky and heavy solution.

A double layer coil solution has been proposed in [34] which increases the frequency of the flux produced when two 180° phase shifted currents are passed through it. It generates magnetic flux of frequency twice to that of feeding current of coil. This has limitation of complexity in the design.

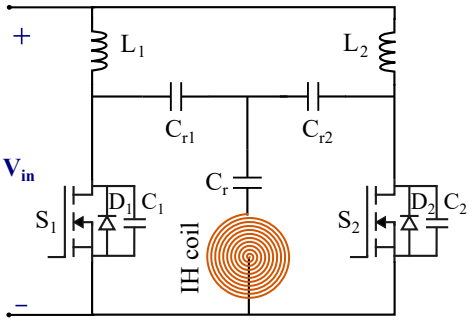

Figure 2.18: Time-sharing high-frequency multiple-resonant soft-switching inverter [35]

Time sharing technique is used in [35,36] to meet different material heating requirement. As shown in Figure 2.18, it uses electro-mechanical switch which has its limitation. The number of components is also high.

In [37], a selective harmonic approach is used for all metal heating. The proposed solution is presented in Figure 2.19. But the current requirement for N-FM vessel heating is high. FM loads were powered at selected fundamental frequency while N-FM load is controlled at the respective third harmonic frequency. The current for N-FM load is high and the control is not flexible.

A dual frequency approach is used with a FB circuit in [38]. It acts as a combination of two HB circuits operated at two different frequencies. This meets two different frequency requirement of different material IH loads. But soft switching is affected due to dual frequency.

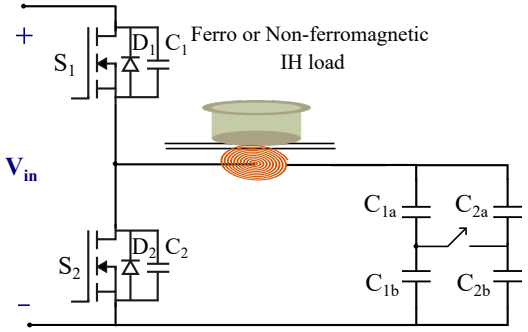

Figure 2.19: HB inverter with selective harmonic approach [37]

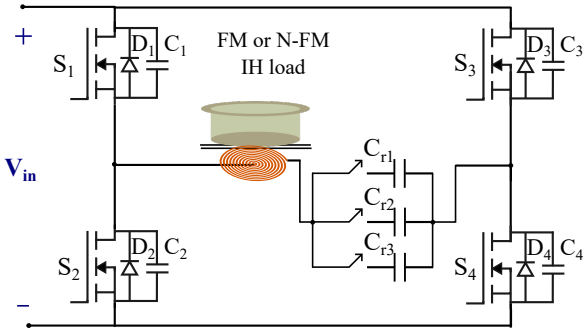

Figure 2.20: FB inverter with LAM technique [39]

In [39], load adaptive modulation technique with FB and HB inverters is proposed. The proposed FB inverter with LAM technique is shown in Figure 2.20. Frequency doubler and tripler mode is used as per the type of material. This also uses electro-mechanical switches for capacitor selection.

Single frequency double layer coil approach is used in [40]. By using double layer coil with transformer action, current induced in the vessel is increased. This reduces the current requirement of the inverter. But the design complexity is increased.

With similar concept as above, multi-phase coupled coil approach is proposed in [28]. HB based multiple load approach is used. Power control is done with phase-shift control. It suffers with increased number of component and complex design.

Cascaded FB topology is used in [41] for heating all metal. Two full bridges are cascaded. Two inverter legs of one FB are operated at two different frequencies and second FB is operated at other frequency. Frequencies are selected based on IH load. But this approach suffers with increased component count. Soft-switching range is also decreased with this approach.

A dual resonant inverter topology has been proposed in [42]. It uses series and series-parallel resonance for heating FM and N-FM material respectively. It uses electro-mechanical switch.

An all metal IH solution with sand-witch coil structure is proposed in [43]. Along with one resonant capacitor, it also uses different switched capacitor arrangement to achieve magnetic resonance coupling for different material vessels. Burst firing control is used for output power regulation. The design complexity is more as well as component count is increased with this approach.

In [44], the operating frequency of inverter is varied as per the selected type of IH load. Load power is controlled by using flexible load modulation. The effect of shape and size of material is also investigated.

2.3 AC-AC Topologies

This section details different inverter topologies available in the literature with direct conversion of AC utility supply of 50/60Hz to high frequency AC of 20-30 kHz. These topologies have been subdivided into single load, multiple load and different material IH load topologies.

2.3.1 Single load AC-AC converter topologies

In this subsection, AC-AC topologies available in the literature for powering one load at a time are discussed in detail.

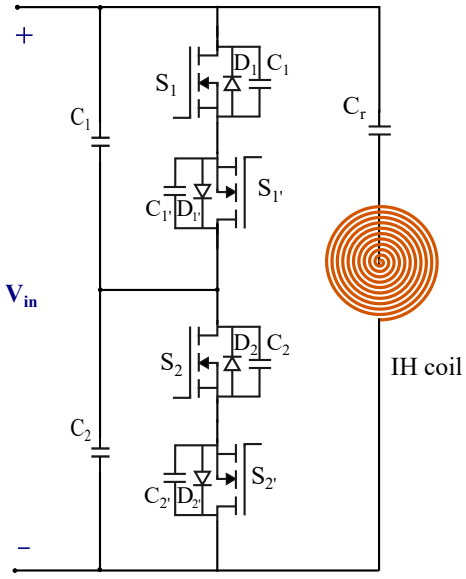

Figure 2.21: HB based four switch AC-AC converter [45]

In [45], a HB based four switch AC-AC converter with split capacitor arrangement is used for direct ac-ac conversion and is depicted in Figure 2.21. It does not require any recti-

fication stage. Utility frequency supply is directly converted into high frequency AC supply. Synchronous rectification and zero voltage switching are realised with two half bridges. For output power regulation, phase-shift control is implemented. But it suffers with voltage unbalancing in split capacitors.

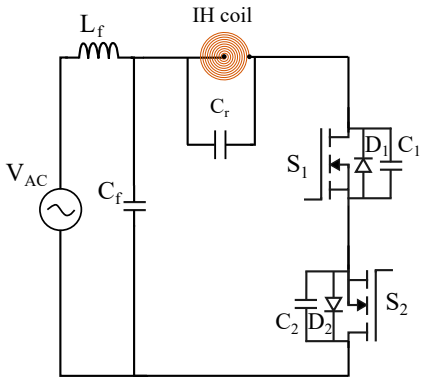

Figure 2.22: Class E based direct AC to AC converter [46]

In [46], class-E based direct AC to AC converter is proposed. It uses conventional class-E inverter approach with a bidirectional and bipolar equivalent switches for direct AC-AC conversion as shown in Figure 2.22. The control of multi-cycle modulation is used for power regulation which reduces peak voltage and provides better power control. It also operates with ZVS during turn-on of switches. However, this topology uses parallel resonance for IH load which has some limitations such as circulating current flow which will affect the overall efficiency.

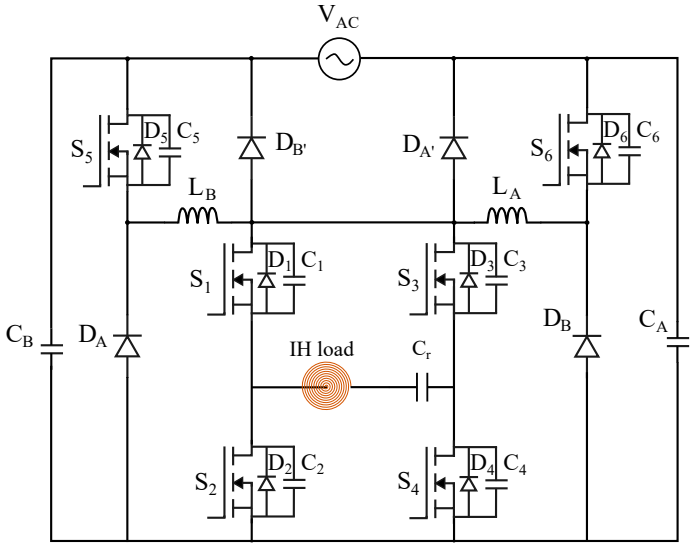

Figure 2.23: AC-AC buck-boost converter [47]

In [47], an AC-AC buck boost inverter with full bridge at its output is proposed. The proposed converter is as shown in Figure 2.23. During each half cycle, respective buck-boost

converter is operated for regulating the dc link voltage. This voltage is inverted again by the full bridge circuit. It has relatively higher component count. Also, due to hard switching in buck-boost devices, power losses will be high. So, overall efficiency for the system will be reduced.

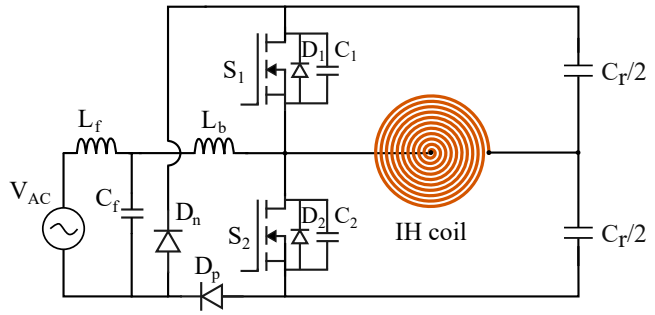

Figure 2.24: HB based bridge less AC-AC converter with voltage boosting [48]

In [48], an AC to AC converter is proposed with boosting stage. It uses a half-bridge circuit along with two diodes as shown in Figure 2.24 to convert utility frequency AC supply to high frequency AC supply. Boosting stage is also combined with HB circuit operation. It uses an asymmetric PWM technique for power regulation. The soft switching operation of the devices is affected at low power operation mode. Also, the gate pulse generation complexity increases as the pulses are to be changed as per the AC mains half cycle to ensure same boosting levels during positive and negative half cycles.

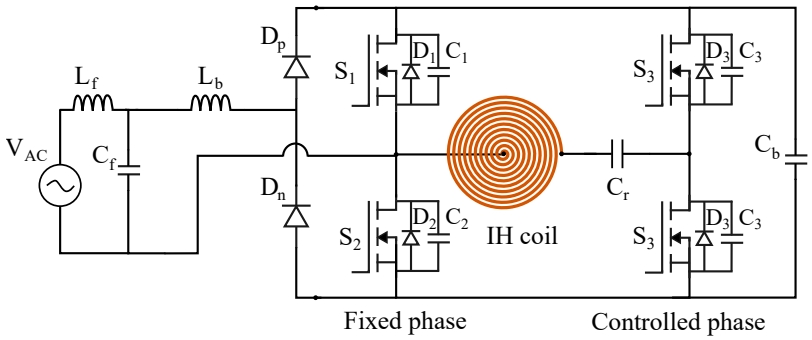

Figure 2.25: FB based AC-AC converter [49]

In [49, 50], a direct AC to AC full-bridge base converter is proposed. Boosting operation is combined with the first leg of FB circuit as depicted in Figure 2.25. For power control, phase-shift control is implemented. It has been observed that this converter with the proposed control technique operates with a better ZVS range. Hence, the operational efficiency for high power operation is increased. But the control gets a bit complicated as same boosting voltage is to be maintained during positive and negative cycles of input mains.

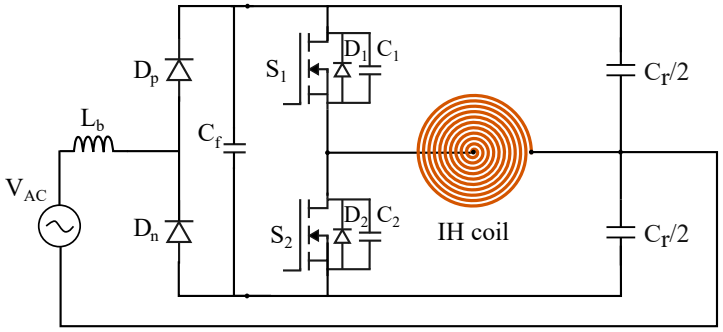

Figure 2.26: HB based AC-AC converter [51]

In [51], a half-bridge series resonant converter with direct AC to AC conversion and voltage doubling capacity is proposed. The proposed converter is presented in Figure 2.26. As the voltage is doubled, current in the circuit is reduced. This helps in better efficiency when compared with the classical HB topology approach. The performance of the converter is investigated with square wave control with variable frequency and asymmetric duty cycle control. Square wave control gives poor efficiency for low power mode while ADC control operates with soft-switching restrictions on its duty cycle. Also, boosting will be affected with ADC control. In this converter, low frequency AC current also flows in the IH load which is undesirable.

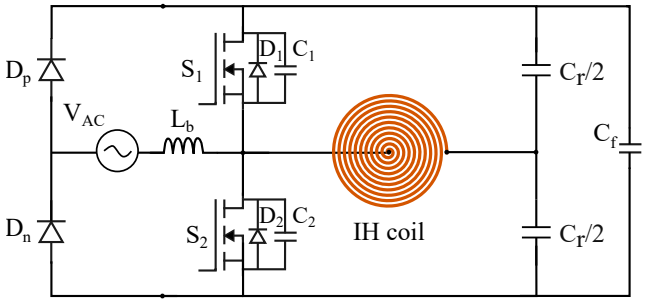

Figure 2.27: HB based improved direct AC-AC converter [52]

In [52], previously proposed circuit is further modified to overcome its limitations. The modified converter is as shown in Figure 2.27. It also proposes a boost type HB inverter with direct AC-AC conversion. Due to voltage boosting, current levels will be less which aids in efficiency improvement. Also, soft-switching range for the inverter switching devices is increased when compared to the previous work. Power regulation is done by using AVC control. In this circuit, low frequency currents are not flowing through IH load. Hence, peak current levels are reduced. However, in order to maintain same boosting during positive and negative half cycle, the control pulses for high side and low side switches are to be interchanged. This makes the control a little complex.

2.3.2 Multiple load AC-AC converter topologies

In this subsection, AC-AC based topologies available in the literature for powering multiple loads at a time are discussed.

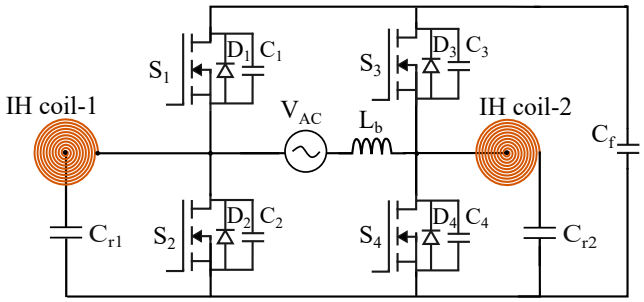

Figure 2.28: Dual output AC-AC converter [53]

In [53], a dual-output AC to AC converter with boosting operation in full-bridge mode is proposed. The proposed converter is depicted in Figure 2.28. It combines two HB branches. In each half cycle of AC mains, one HB is used for boost operation while the other is used for powering the load. Compared to previous approaches, it can power two IH loads by using single boost inductor. Generation of control pulses becomes a bit complicated as boosting and HB modes are changed as per zero crossing of source voltage. It gives 8.15% THD when operating at 2 kW with 50 kHz switching frequency. Mains synchronised PDM, variable frequency and variable duty cycle controls have been investigated.

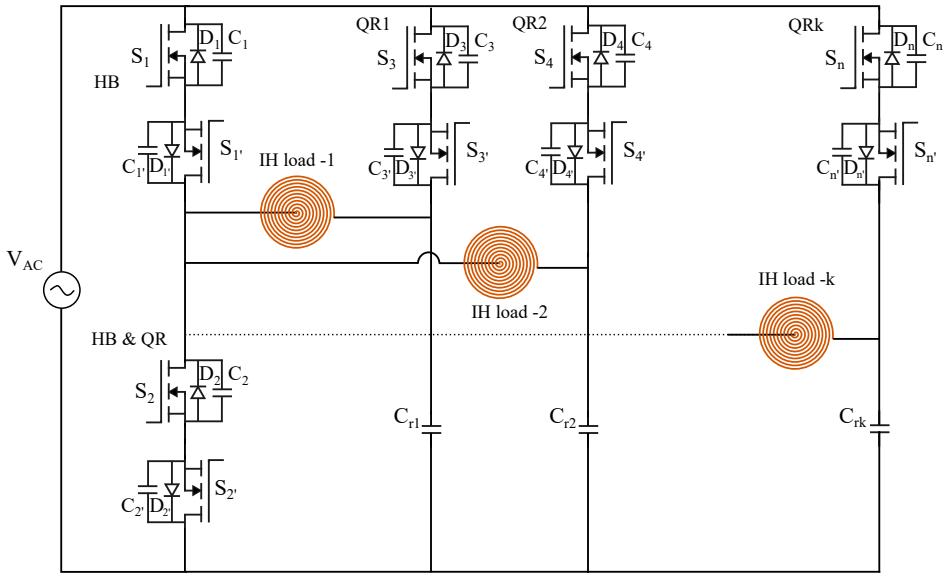

Figure 2.29: Multiple output AC-AC converter [54]

In [54], a multiple output IH converter is proposed with direct AC to AC conversion. It

is the combination of half-bridge and single switch quasi-resonant configurations as shown in Figure 2.29. First leg consists of four devices which are forming two bidirectional switches. For each IH load, an additional leg with two anti-series switches is used. Power control is realised with HB and quasi-resonant operating modes. HB based control is used for controlling power from 50 W to 2000W while quasi-resonant mode is used for power control between 1000 W to 2000 W. The component count for this topology is high. Also, it is investigated that it becomes difficult to meet the EMI standards defined in IEC 55,014–1.

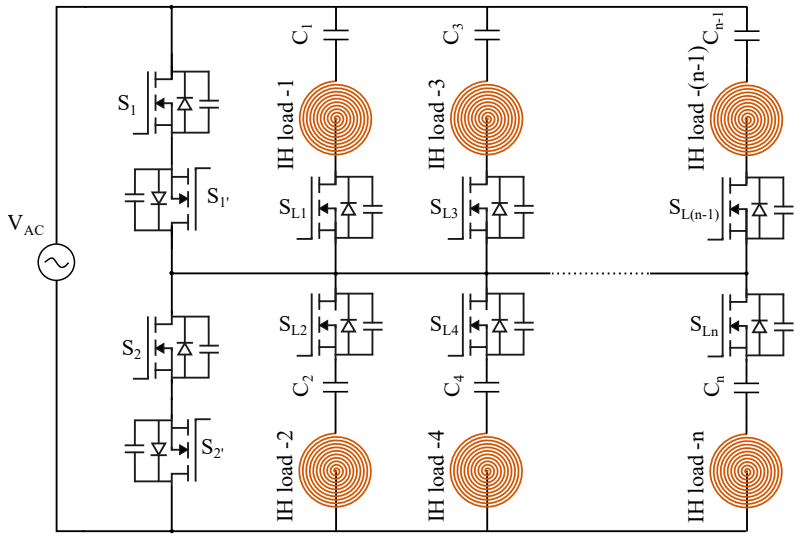

Figure 2.30: Matrix type multiple output AC-AC converter [55]

In [55], a matrix based multiple output resonant converter with direct AC-AC conversion is proposed. Figure 2.30 depicts the proposed AC-AC converter. It uses four switching devices for direct AC-AC conversion. Two sets of anti-series switches are connected to feed a HB topology per each half cycle of low frequency mains supply. IH load with a series switch is connected in parallel to each high side and low side switch of HB circuit. Multiple IH loads can be connected in parallel to high and low side switches of HB. Each IH load is controlled using ON-OFF control of series device in the respective IH load. This is a simple solution for multiple load IH. But this approach will lead to unbalance in the input supply which eventually increases the filter requirement.

2.3.3 Different material load AC-AC converter topologies

In this subsection, the AC-AC based converter topologies available in the literature for powering different material IH loads are discussed.

In [56], an AC-AC resonant converter with a boosting stage and FB operation is proposed

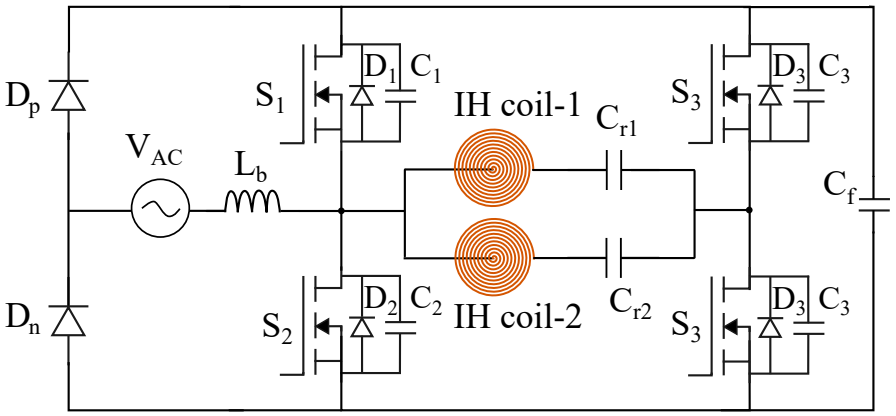

Figure 2.31: FB based AC-AC resonant converter for different material IH loads [56]

for heating FM and N-FM material based vessels. The proposed AC-AC resonant converter for different material heating is as shown in Figure 2.31. Two different material vessel IH loads are resonated at two different frequencies. FM load is resonated at low frequency while N-FM load is resonated at a high frequency. Two inverter legs of FB topology are operated at low and high switching frequencies as per the IH load requirements. Asymmetric duty cycle control is used for realising independent power control. Even though high switching frequency operation is used, soft switching is not ensured in this solution. This affects the efficiency of the overall system.

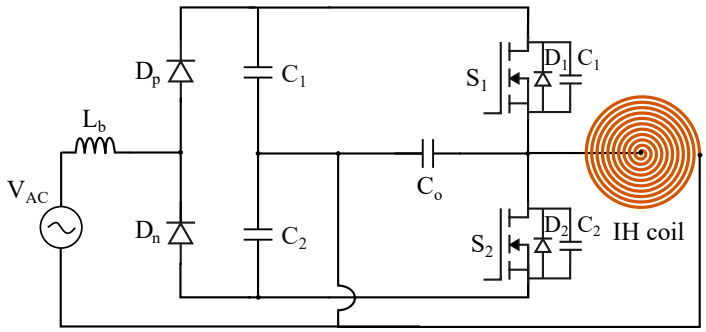

Figure 2.32: Boost type AC-AC converter for different material IH loads [57]

In [57], a direct AC to AC converter is proposed by using two diodes and two switching devices as shown in Figure 2.32. For control, asymmetrical duty cycle and mains synchronised pulse density modulation are proposed. ZVS is obtained for the wider range of power control using this dual control. PDM offers a better ZVS control for the entire operating region. However, input current profile gets deteriorated for lower duty cycle of PDM control.

2.4 Summary

In this chapter, a comprehensive overview of different inverter topologies available in the literature for IH application, have been discussed in detail. Single load, multiple load and different material IH load topologies for DC-AC and AC-AC conversion based approaches have been discussed in detail. The advantages and short comings of these topologies also have been discussed.

For multiple load IH application, the main requirements are simultaneous and independent power control, easier extension of multiple loads with reduced component count, soft-switching operation and high efficiency. Most of the proposed inverter topologies for multiple load do not meet all these requirements. Ability to heat different material IH loads is also a desirable feature of IHS. Few inverter topologies are available in the literature which meet the multiple load requirement of different material IH loads. And they also have their own advantages and limitations. Hence, there is a good scope for research in this area. In order to meet the above mentioned requirements of multiple load IH application, four inverter topologies have been proposed, investigated in detail and are presented in the following chapters.

Chapter 3

Three Switch Resonant Inverter for Multiple Load Induction Cooking Application

Chapter 3

Three Switch Resonant Inverter for Multiple Load Induction Cooking Application

3.1 Introduction

Multiple load heating is a common requirement for induction cooking (IC) application. The major requirements of multiple load IH applications are simultaneous and independent power control, low component count and easier extension for additional loads. In this chapter, a three switch resonant inverter (3SI) configuration has been proposed for multiple load induction cooking application. The proposed inverter is suitable for multiple load IC applications. It uses three switches to control two similar IH loads. And the extension of this inverter configuration is suitable for heating multiple vessels of FM as well as N-FM materials. Reduced component count and high efficiency are the key benefits of the proposed inverter. Asymmetric duty cycle (ADC) control is used to obtain independent control over two loads simultaneously. The operation of the proposed 3SI has been verified by rigorous simulations in OrCAD PSpice software and by experimenting with designed hardware prototype of 550W.

Following is the section-wise outline of this chapter. Section 3.2 details the proposed inverter and its different operating modes. Section 3.3 comprises of the analysis and derivation of equations related to the inverter output power. Section 3.4 shows the detailed efficiency analysis of the inverter. Section 3.5 focuses on simulation, experimental setup and experimental results of the inverter. Extension of the proposed inverter for multiple loads is discussed in Section 3.6. The important conclusions of this chapter are presented in Section 3.7.

3.2 Proposed Three Switch Inverter Configuration

Figure 3.1 shows the circuit diagram of the proposed 3SI configuration for multiple load IH applications. A DC source V_{DC} with two split capacitors, supplies power to two IH loads (Load-1 and Load-2) through three MOSFETs (S_1, S_2 and S_3). An IH load is modeled as series combination of a R and L. Where R is the equivalent resistance and L is the equivalent inductance of IH load as measured from the coil side. Load-1 is modeled with R_1 and L_1. Load-

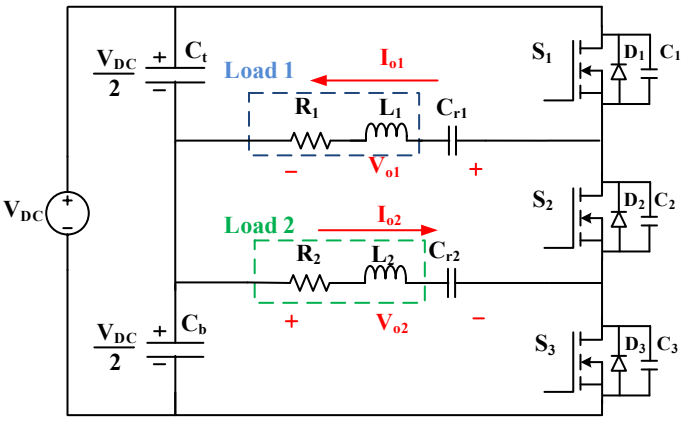

Figure 3.1: Proposed three switch inverter configuration

2 is modeled with R_2 and L_2. Resonant capacitors C_{r1} and C_{r2} are used to resonate load-1 and load-2 respectively. Value of resonant capacitors are selected such that both loads will operate in slightly inductive mode to ensure ZVS operation. V_{01}, I_{o1} and V_{o2}, I_{o2} are output voltages and currents for load-1 and load-2 respectively. Conventions of currents and voltages indicated in Figure 3.1 are taken as the reference.

Fig 3.2 shows the waveforms of the switching pulses of devices S_1, S_2 and S_3 (V_{g1}, V_{g2} and V_{g3} respectively) and output voltages. V_{g2} is generated by logical EX-OR of V_{g1} and V_{g3}. Figure 3.3 shows different operating modes of the proposed three switch inverter.

3.2.1 Mode-1 $(0 - t_1)$

As shown in Figure 3.2, S_2, S_3 switches are ON and switch S_1 is OFF during this mode. Voltage across S_1 in its OFF state is V_{DC}. S_3 is being turned ON from Mode-3 to Mode-1. Negative current flowing through body diode D_3 ensures ZVS during turn-on of S_3. Bottom capacitor (C_b) in split capacitor arrangement powers both the IH loads in this mode. Load-1 current flows through switches S_2 and S_3 where as load-2 current flows through switch S_3 only. Flow of currents through the loads is as shown in the Figure 3.3.

3.2.2 Mode-2 $(t_1 - t_2)$

During this mode, switches S_1, S_3 are ON and S_2 is OFF. The voltage across S_2 in its OFF state is V_{DC}. S_1 is being turned ON from Mode-1 to Mode-2. Freewheeling of load-1 current through body diode D_1 assures ZVS turn-on of S_1. Load-1 and load-2 are powered by top and bottom split capacitors (C_t and C_b) respectively. Load-1 output voltage polarity and current direction reverses whereas load-2 output voltage polarity and current direction remains

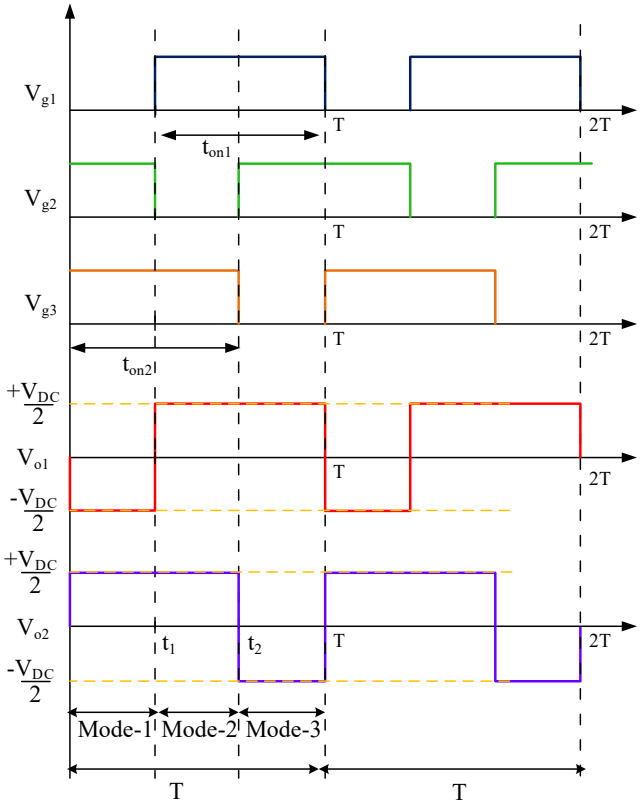

Figure 3.2: Proposed 3SI waveforms. From top to bottom: gate pulses, load-1 output voltage (V_{o1}) and load-2 output voltage (V_{o2})

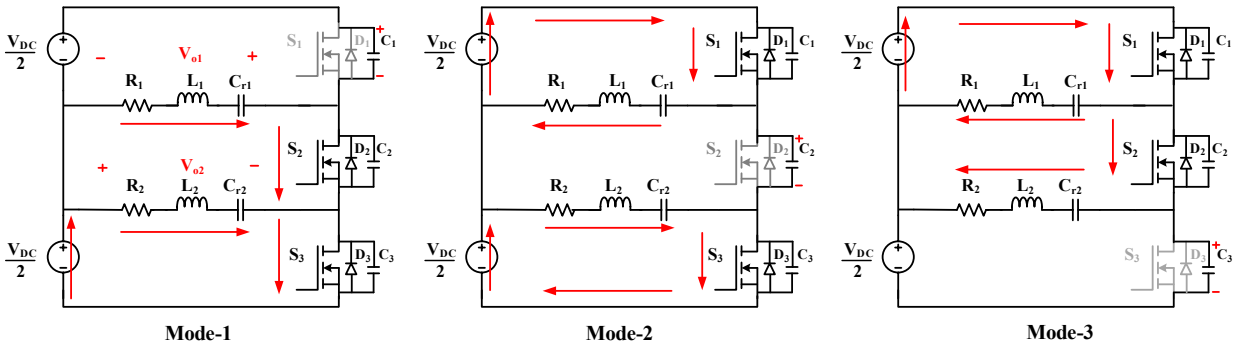

Figure 3.3: Modes of operation

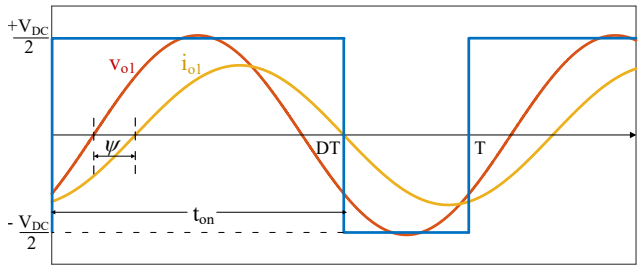

Figure 3.4: Output voltage-current waveform

the same as Mode-1. Flow of currents through the loads is as shown in the Figure 3.3.

3.2.3 Mode-3 ($t_2 - T$)

During this mode, switches S_1, S_2 are ON and S_3 is OFF. C_t powers both the IH loads. The voltage across S_1 in its OFF state is V_{DC}. S_2 is being turned ON from Mode-2 to Mode-3. ZVS during turn-on of S_3 is ensured as the negative current flows through body diode D_3. Load-1 and load-2 currents flow through switches S_1 and S_2 respectively. Load-2 output voltage polarity and current direction is reversed in this mode. The flow of currents through the loads is as shown in the Figure 3.3.

3.3 Output Power Calculations

By doing Fourier analysis on the output load voltage waveform depicted in Figure 3.4, the expression for output voltage is obtained as:

$$v_o(t) = \frac{V_{DC}(2d-1)}{2} + \sum_{n=1}^{\infty} \frac{2V_{DC}}{n\pi} \sin(n\pi d)\cos(n\omega t - n\pi d) \tag{3.1}$$

where $d = \frac{t_{on}}{T}$, t_{on} is the ON time period of the switching devices and $0.5 \leq d < 1$. The fundamental voltage component is:

$$v_{o1}(t) = \frac{2V_{DC}}{\pi} \sin(\pi d)\cos(\omega t - \pi d) \tag{3.2}$$

Peak and rms output voltages can be expressed as:

$$V_m = \frac{2V_{DC}}{\pi} \sin(\pi d) \tag{3.3}$$

$$V_{rms} = \frac{\sqrt{2}V_{DC}}{\pi} \sin(\pi d) \tag{3.4}$$

The fundamental current can be derived as:

$$i_o = I_m \sin(\omega t - \pi d - \psi) \tag{3.5}$$

where I_m is the peak current and ψ is the phase angle between current and voltage. Now, $I_m = \frac{V_m}{|Z|}$, where $Z = R + j\omega L - \frac{j}{\omega C}$ = impedence of the load. Resistive part of the load, $R = |Z|\cos\psi$ and inductive part of the load $X = |Z|\sin\psi$. And,

$$\cos\psi = \frac{1}{\sqrt{1 + Q_L^2(\frac{\omega}{\omega_o} - \frac{\omega_o}{\omega})^2}} \tag{3.6}$$

where Q_L = quality factor of the load, ω_o = resonant frequency. Load rms current can be derived as:

$$I_{o,rms} = \frac{\sqrt{2}V_{DC}\sin(\pi d)}{\pi}\frac{\cos\psi}{R} \tag{3.7}$$

Now, output load power $P_o = I_{o,rms}^2 R_i$. Hence,

$$P_o = \frac{2V_{DC}^2\sin^2(\pi d)}{\pi^2 R^2} \times \frac{R_i}{1 + Q_L^2(\frac{\omega}{\omega_o} - \frac{\omega_o}{\omega})^2} \tag{3.8}$$

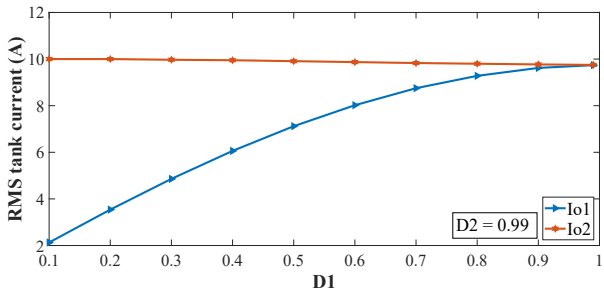

(a)

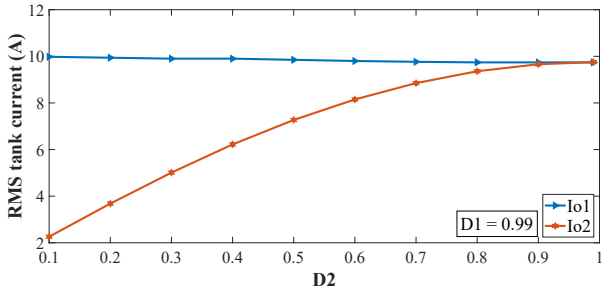

(b)

Figure 3.5: Variation of RMS tank current with duty cycle. (a) D_1 varied with D_2 constant at D_{2max}, (b) D_2 varied with D_1 constant at D_{1max}.

where $R = R_i + r_{DS} + r_L + r_C$. R_i is the effective resistance of IH load, r_{DS} is average equivalent ON state resistance of MOSFET, r_L and r_C are parasitic resistances offered by inductor and capacitor respectively.

The proposed 3SI must be operated with t_{on} greater than $|T/2|$ with ADC control. So duty cycle for control is defined as:

$$D = \frac{T - t_{on}}{T/2} \tag{3.9}$$

where t_{on} is ON time duration of the switch which is greater than $|T/2|$. Duty cycles D_1 and D_2 are obtained for switches S_1 and S_3 using expression (3.10) and (3.11) as below:

$$D_1 = \frac{T - t_{on1}}{T/2} \tag{3.10}$$

$$D_2 = \frac{T - t_{on2}}{T/2} \tag{3.11}$$

The control over load-1 and load-2 power is obtained by varying D_1 and D_2 respectively. The change in IH load rms currents over duty cycle is as per Figure 3.5. Figure 3.5(a) depicts the change in load rms currents when D_1 is varied by keeping D_2 at 99%. Figure 3.5(b) shows the change in load rms curents when D_2 is varied by keeping D_1 at 99%.

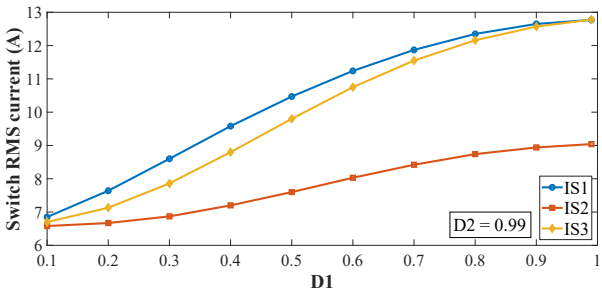

(a)

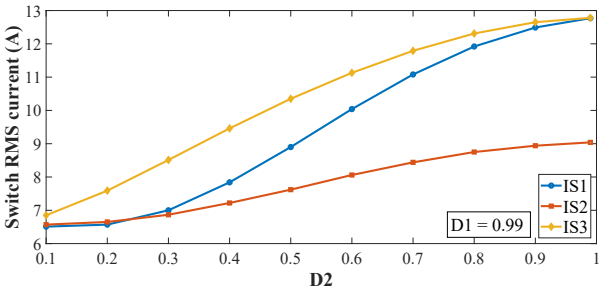

(b)

Figure 3.6: Variation of switch RMS current with duty cycle. (a) D_1 varied with D_2 constant at D_{2max}, (b) D_2 varied with D_1 constant at D_{1max}.

3.4 Efficiency Analysis

For the proposed 3SI, the efficiency(η) can be obtained as the ratio between its output to input power. Output power is the net power delivered to the load after losses. Losses in the inverter can be categorised as conduction losses, P_{con} and switching losses, P_{sw}.

$$\eta = \frac{P_o}{P_{in}} = \frac{P_{in} - P_{losses}}{P_{in}} = \frac{P_{in} - (P_{con} + P_{sw})}{P_{in}} \tag{3.12}$$

3.4.1 Conduction losses

Conduction losses are summation of the losses in the switching devices ($P_{con,sw}$), losses in the resonant capacitors ($P_{con,rc}$) and losses in the IH coil ($P_{con,coil}$).

3.4.1.1 Conduction losses in switches

The current flowing through the switches are part of the load currents. Expressions for the currents flowing through switch-1 (i_{S1}), switch-2 (i_{S2}) and switch-3 (i_{S3}) can be expressed as below:

$$i_{S1} = \begin{cases} 0 & 0 < t < t_1 \\ i_{o1} & t_1 < t < t_2 \\ i_{o1} + i_{o2} & t_2 < t < T \end{cases} \tag{3.13}$$

$$i_{S2} = \begin{cases} i_{o2} & 0 < t < t_1 \\ 0 & t_1 < t < t_2 \\ i_{o2} & t_2 < t < T \end{cases} \tag{3.14}$$

$$i_{S3} = \begin{cases} i_{o1} + i_{o2} & 0 < t < t_1 \\ i_{o2} & t_1 < t < t_2 \\ 0 & t_2 < t < T \end{cases} \tag{3.15}$$

Where t_1 = (1-D_1)T and t_2 = (1-D_2)T. Load currents can be expressed using expression (3.5) as below:

$$i_{o1} = I_{m1} \sin(\omega t - \pi D_1 - \psi_1) \tag{3.16}$$

$$i_{o2} = I_{m2} \sin(\omega t - \pi D_2 - \psi_2) \tag{3.17}$$

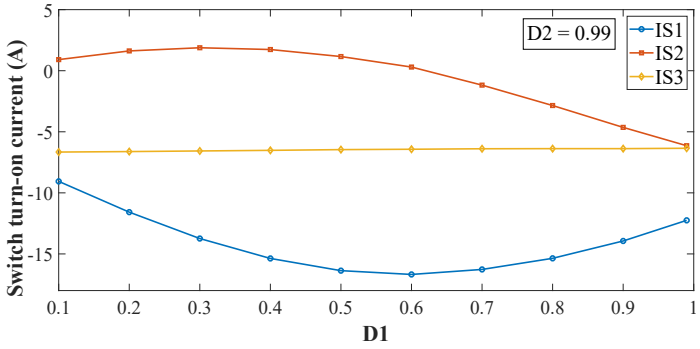

(a)

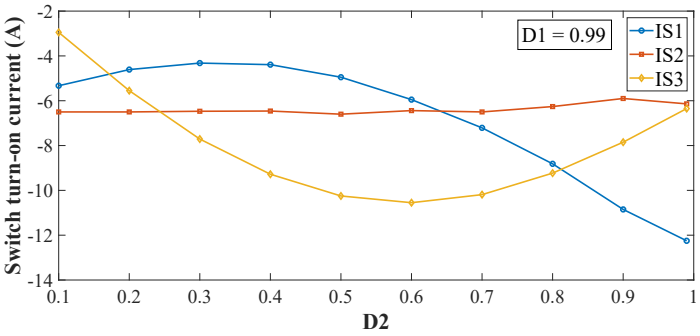

(b)

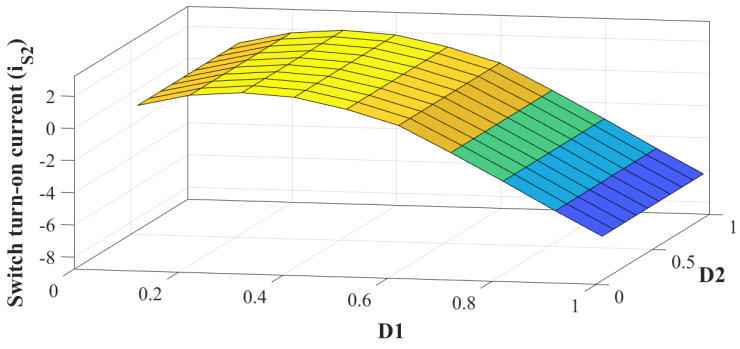

(c)

Figure 3.7: Variation of switch turn-on current with duty cycle. (a) D_1 varied with D_2 constant at D_{2max}, (b) D_2 varied with D_1 constant at D_{1max} and (c) switch S_2 turn-on current with variation in D_1 and D_2.

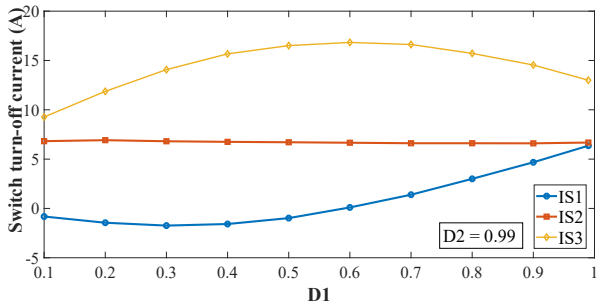

(a)

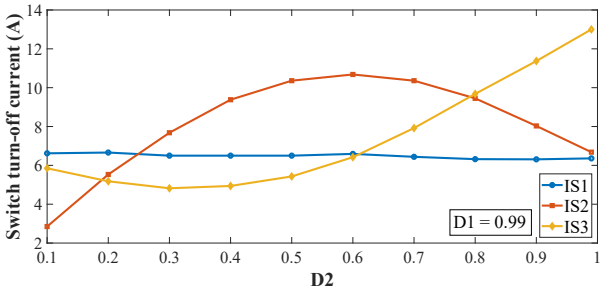

(b)

Figure 3.8: Variation of switch turn-off current with duty cycle. (a) D_1 varied with D_2 constant at D_{2max}, (b) D_2 varied with D_1 constant at D_{1max}.

where i_{o1} is load-1 current and i_{o2} is load-2 current. Instantaneous turn-on and turn-off currents and rms currents for the devices can be obtained using equations (3.13) to (3.15). Conduction loss in switching devices can be expressed as:

$$P_{con,sw} = [(I_{S1})^2 + (I_{S2})^2 + (I_{S3})^2] \times r_{DS} \tag{3.18}$$

where r_{DS} is drain to source resistance of each MOSFET. I_{S1}, I_{S2} and I_{S3} are rms currents flowing through switches S_1, S_2 and S_3 respectively. The variations in switch rms currents with duty cycle is shown in Figure 3.6. Figure 3.6(a) depicts change in switch rms currents when D_1 is varied by keeping D_2 at 99%. Figure 3.6(b) shows the change in switch rms curents when D_2 is varied by keeping D_1 at 99%.

3.4.1.2 Conduction losses in resonant capacitors and induction coil

Equivalent Series Resistance (ESR) of resonant capacitors will lead to conduction losses which can be given as:

$$P_{con,rc} = (I_{rc,rms})^2 \times r_{RC} \tag{3.19}$$

where $I_{rc,rms}$ is the rms current flowing through the resonant capacitor and r_{RC} is the ESR of resonant capacitor. The parasitic resistance of the IH coil also leads to power losses as

$$P_{con,coil} = (I_{coil,rms})^2 \times r_{coil} \tag{3.20}$$

where r_{coil} and $I_{coil,rms}$ are the resistance and rms current which flows through the IH coil respectively. In the proposed inverter, the current which flows through the resonant capacitors and the IH coil are same as the respective load currents.

3.4.2 Switching losses

Switching losses are related to the turn-on and turn-off of the devices. In the proposed 3SI, soft switching has been achieved for both the switching transitions of each device. Lagging nature of the load current ensures ZVS during turn-on of the devices. The variation of switch turn-on current with duty cycle is shown in Figure 3.7. Figure 3.7(a) depicts change in switch turn-on currents when D_1 is varied by keeping D_2 at 99%. Figure 3.7(b) shows the change in switch turn-on currents when D_2 is varied by keeping D_1 at 99%. Figure 3.7(c) shows the variation of switch S_2 turn-on current with duty cycles D_1 and D_2. The switch current has to be negative in order to ensure ZVS turn-on of switches. The ZVS turn-on range for the duty cycle can be observed from Figure 3.7.

To ensure ZVS during turn-off, snubber capacitors, C_s, are connected across the drain-source terminal of each device and they are operated with a fixed deadtime, $t_{deadtime}$. The criteria for the selection of the snubber and deadtime is given as:

$$t_{snubber} = \frac{V_{DC}C_s}{i_{off}} < t_{dead-time} < t_{diode,min}. \tag{3.21}$$

where $t_{snubber}$ is the time for the snubber capacitor to reach V_{DC} voltage, $t_{diode,min}$ is the minimum diode conduction time and i_{off} is the turn-off current. The variation of switch turn-off currents with duty cycle is shown in Figure 3.8. Figure 3.8(a) depicts change in switch turn-off currents when D_1 is varied by keeping D_2 at 99%. Figure 3.8(b) shows the change in switch turn-off currents when D_2 is varied by keeping D_1 at 99%.

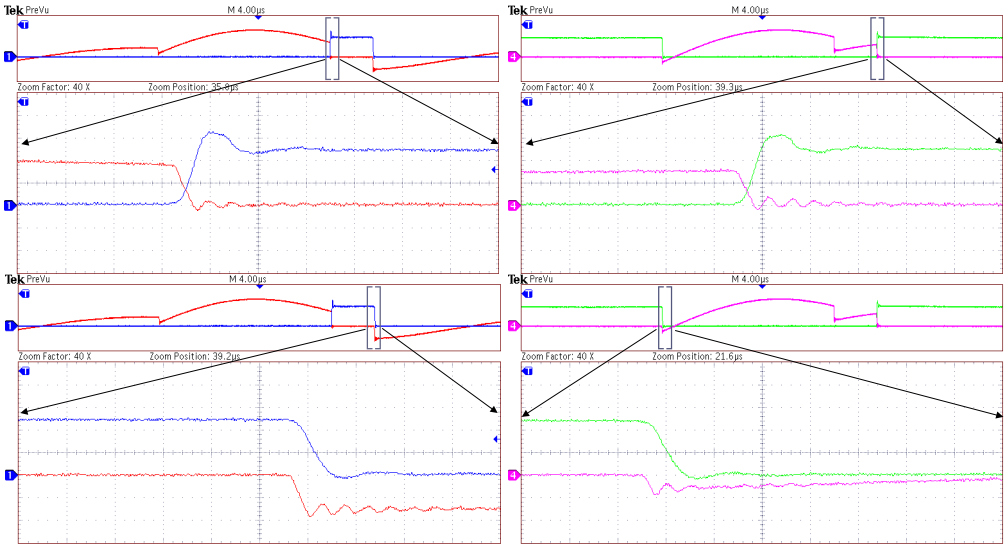

(a) (b)

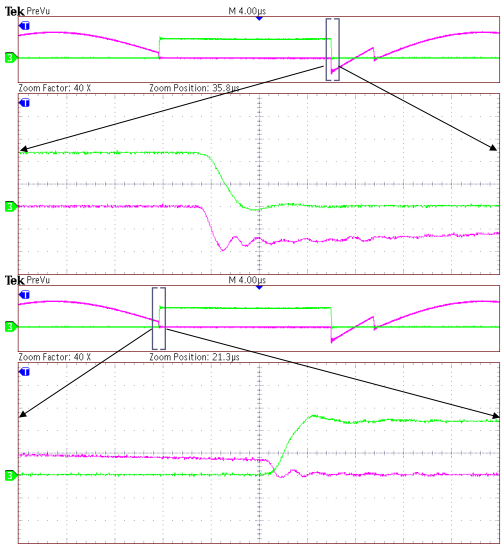

(c)

Figure 3.9: Experimental voltage-current waveforms of switches. Turn-off and turn-on transitions of switches (a) S_1 (b) S_2 and (c) S_3. Scale: voltage (25 V/div), current (4 A/div) and time (100 ns/div)

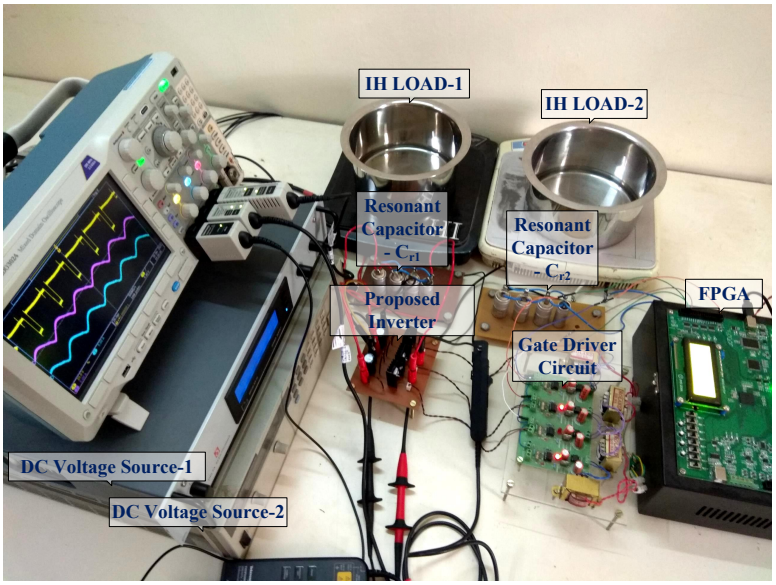

Figure 3.10: Experimental setup

Table 3.1: Parameters of the proposed 3SI.

Component	**Value**
source voltages, $2 \times \frac{V_{DC}}{2}$	2×30 V
equivalent resistance of IH loads, $R_1 = R_2$	2.8 Ω
equivalent inductance of IH loads, $L_1 = L_2$	70.34 μH
resonant capacitors $C_{r1} = C_{r2}$ (MKV-B25834)	0.52 μF
(3*0.1 μF + 0.22 μF)	
ESR for 0.1 μF capacitor	33 mΩ
ESR for 0.22 μF capacitor	17 mΩ
parasitic resistance of IH coils	112 mΩ
switching frequency, f_{SW}	28 kHz
switching devices, MOSFETs	IRF540N
drain-source resistance of MOSFET, r_{DS}	40 $m\Omega$

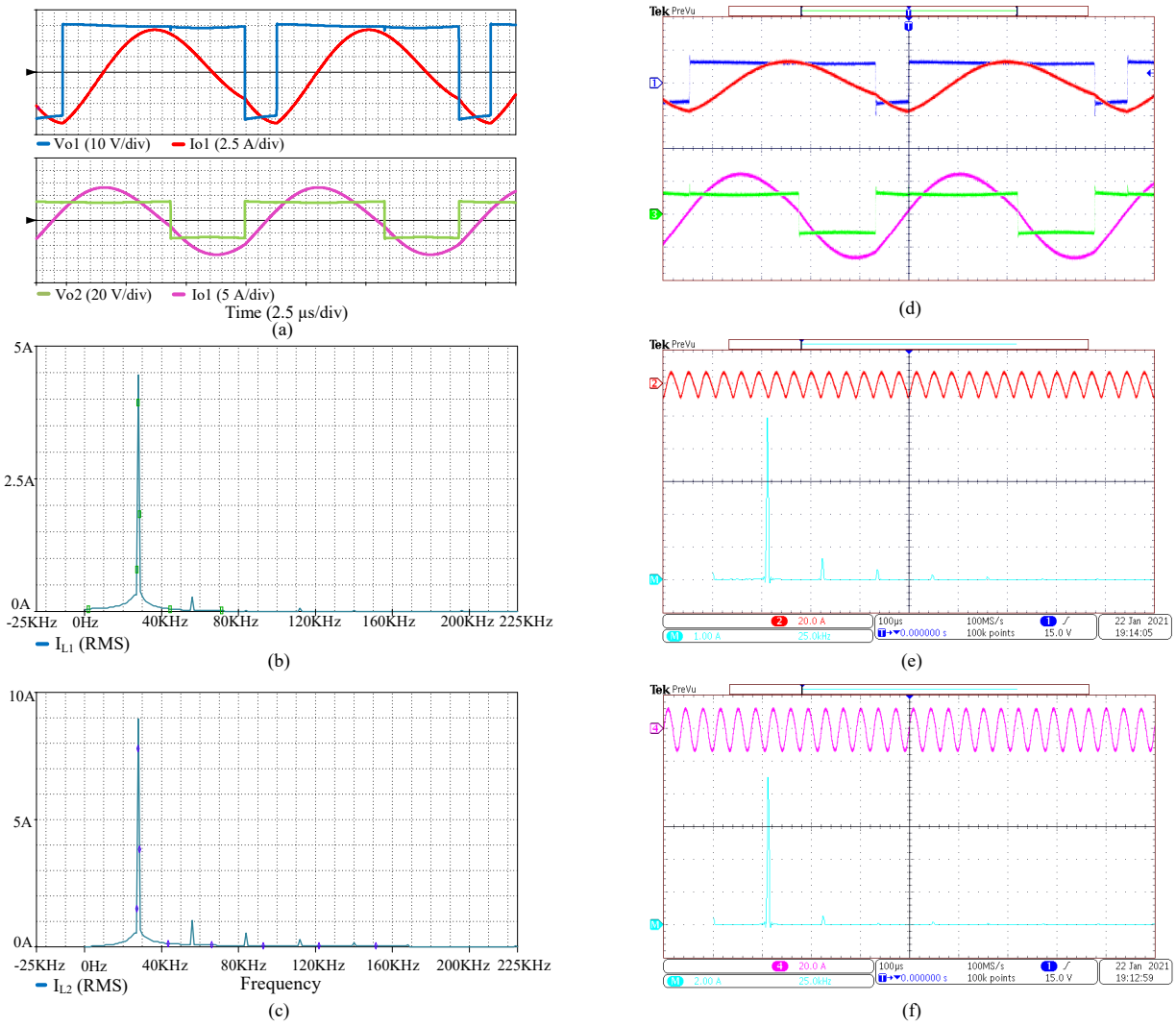

Figure 3.11: Simulation and experimental results with D_1 = 30% and D_2 = 70%. For load-1 and load-2 (a) Simulation waveforms of voltages and currents, (b) and (c) FFTs for load currents under simulation, (d) experimental waveforms of voltages and currents (voltage: 50 V/div, current: 10 A/div), (e) and (f) FFTs for load currents under experimentation.

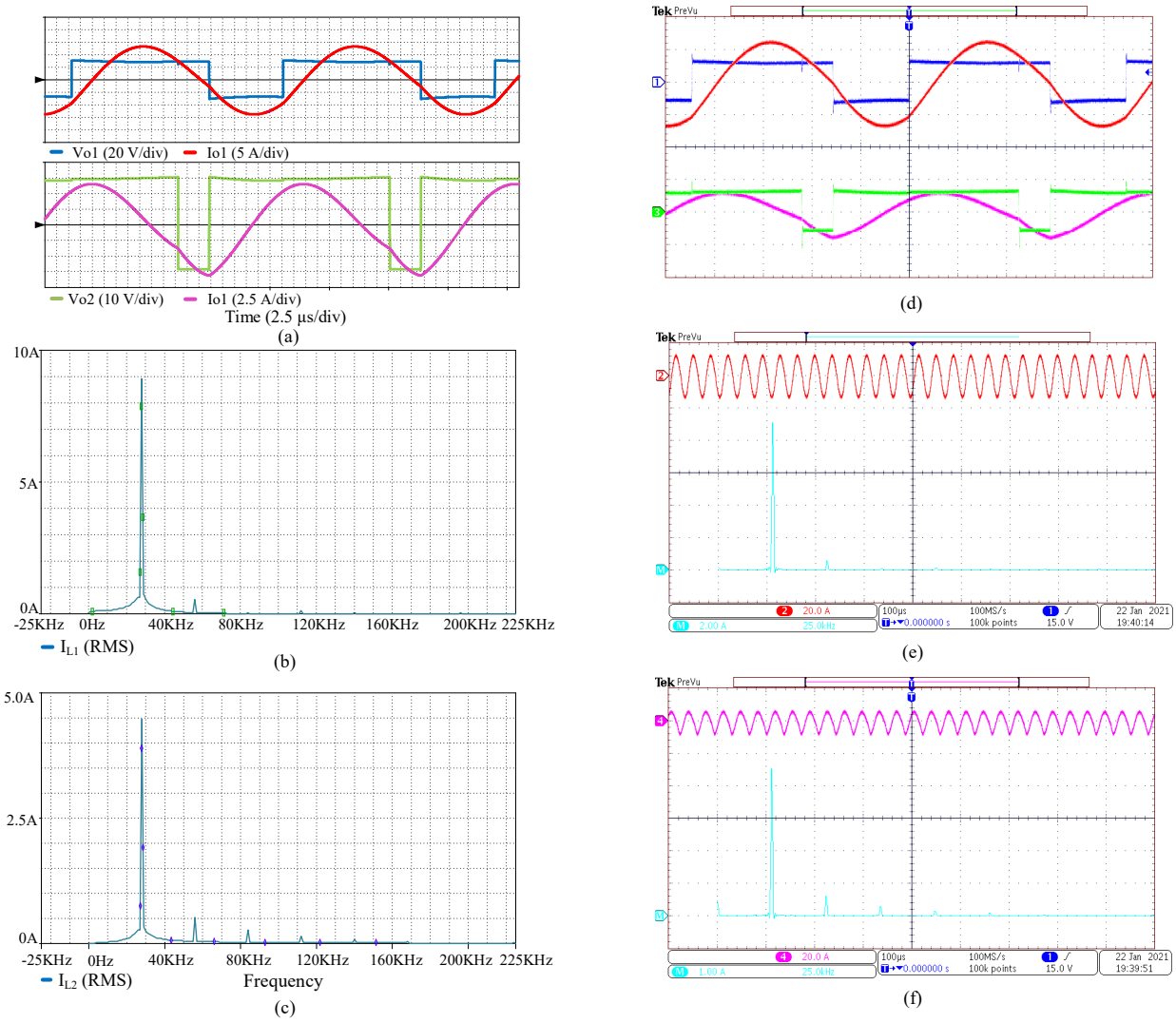

Figure 3.12: Simulation and experimental results with D_1 = 70% and D_2 = 30%. For load-1 and load-2 (a) Simulation waveforms of voltages and currents, (b) and (c) FFTs for load currents under simulation, (d) experimental waveforms of voltages and currents (voltage: 50 V/div, current: 10 A/div), (e) and (f) FFTs for load currents under experimentation.

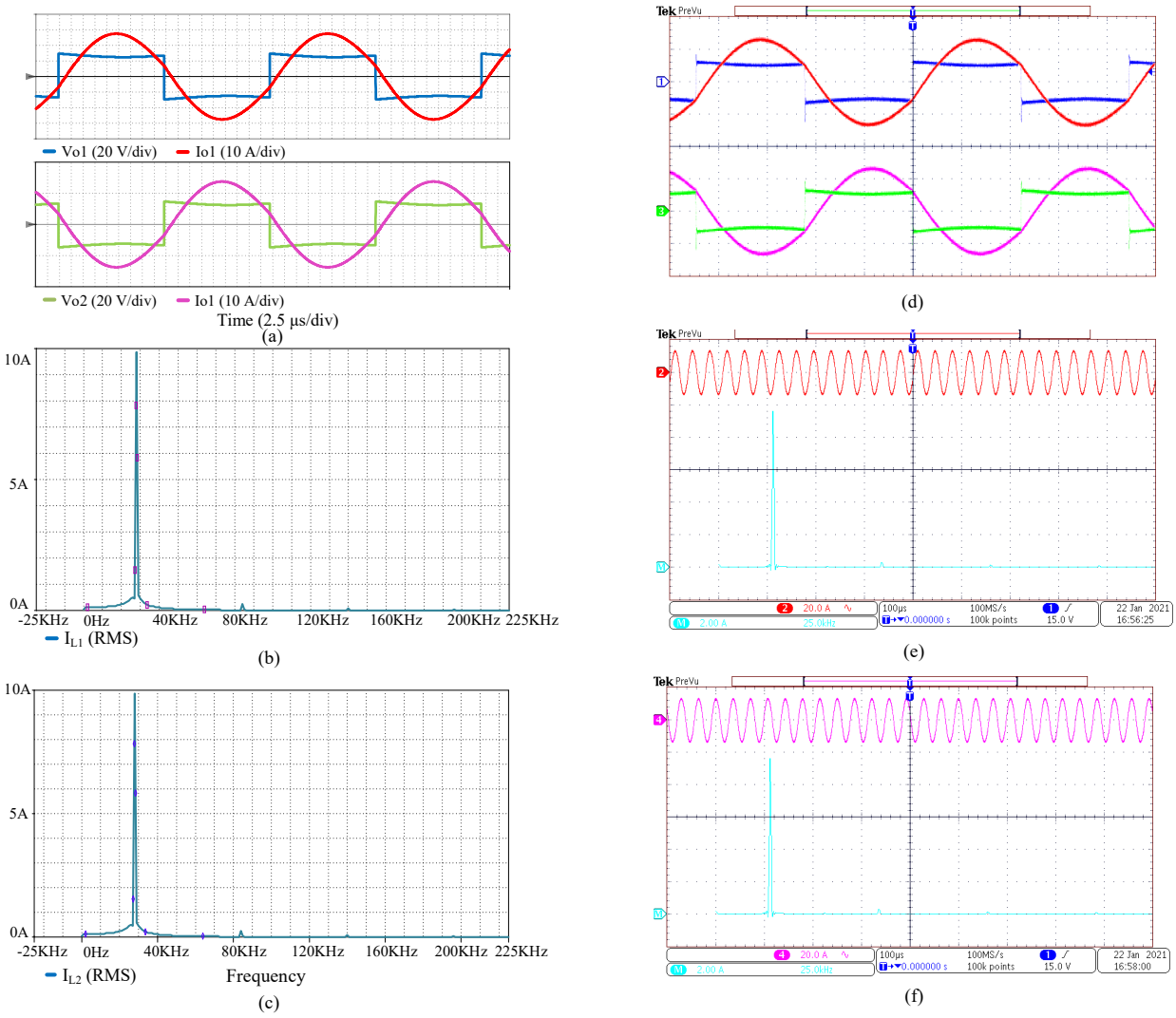

Figure 3.13: Simulation and experimental results with $D_1 = D_2 = 99\%$. For load-1 and load-2 (a) Simulation waveforms of voltages and currents, (b) and (c) FFTs for load currents under simulation, (d) experimental waveforms of voltages and currents (voltage: 50 V/div, current: 10 A/div), (e) and (f) FFTs for load currents under experimentation.

3.5 Simulation and Experimental Results

The proposed three switch inverter is simulated in OrCAD PSpice software and verified experimentally with parameters given under Table 3.1. The complete experimental setup for the proposed 3SI is shown in Figure 3.10. Though a single source with split capacitors can be used, two DC sources, Delta SM100-AR-75 and Agilent-35V have been used for experimentation. In PV based IH applications, dc sources can directly be obtained. A combination of steel vessel and an induction heating coil is realised as an IH load. It is modelled as an equivalent R-L load. Two identical steel vessel loads are used for experimentation. Required capacitance to resonate each load is obtained by the series-parallel combination of MKV type capacitors. The proposed 3SI is controlled using a field programmable gate array (FPGA).

Independent power control in two IH loads is obtained using ADC control technique. The results for simulation and experimentation with duty cycle of load-1 as 30% and load-2 as 70% are shown in Figure 3.11. Load-1 and load-2 are controlled at powers 56.7 W and 222 W respectively. Figure 3.11(a), Figure 3.11(b) and Figure 3.11(c) are simulation results. Figure 3.11(a) shows voltage-current waveforms of IH loads. Figure 3.11(b) and Figure 3.11(c) show FFTs for currents of respective loads. Figure 3.11(d), Figure 3.11(e) and Figure 3.11(f) are experimental results. Figure 3.11(d) shows voltage-current waveforms of IH loads. Figure 3.11(e) and Figure 3.11(f) show FFTs for currents of respective loads.

Figure 3.12 depicts the simulation and experimentation results with duty cycle of load-1 as 70% and load-2 as 30%. Load-1 and load-2 are controlled at powers 222 W and 56.7 W respectively. Figure 3.12(a), Figure 3.12(b) and Figure 3.12(c) are simulation results. Fig 3.12(a) shows voltage-current waveforms of IH loads. Figure 3.12(b) and Figure 3.12(c) show FFTs for load-1 and load-2 currents respectively. Figure 3.12(d), Figure 3.12(e) and Fig 3.12(f) are experimental results. Figure 3.12(d) shows voltage-current waveforms of IH loads. Figure 3.12(e) and Figure 3.12(f) show FFTs for currents of respective loads.

Figure 3.13 depicts the simulation and experimentation results with duty cycle of 99% for both the loads. These two loads are operated at 275 W individually. Figure 3.13(a), Figure 3.13(b) and Figure 3.13(c) are simulation results. Figure 3.13(a) shows voltage-current waveforms of loads. Figure 3.13(b) and Figure 3.13(c) show FFTs for currents of load-1 and load-2 respectively. Figure 3.13(d), Figure 3.13(e) and Figure 3.13(f) are experimental results. Figure 3.13(d) shows voltage-current waveforms of IH loads. Figure 3.13(e) and Figure 3.13(f) show FFTs for currents of respective loads.

From the above results, it can be perceived that simulation results are in harmony with the experimental results. It can be observed from FFTs that load currents contain fundamental

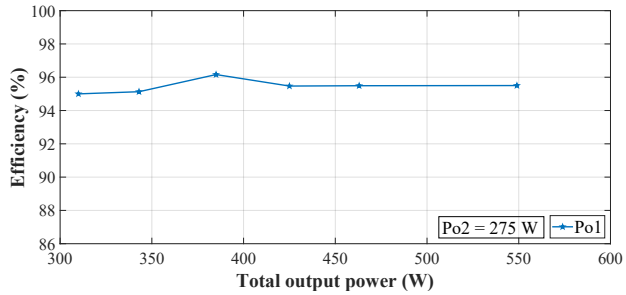

(a)

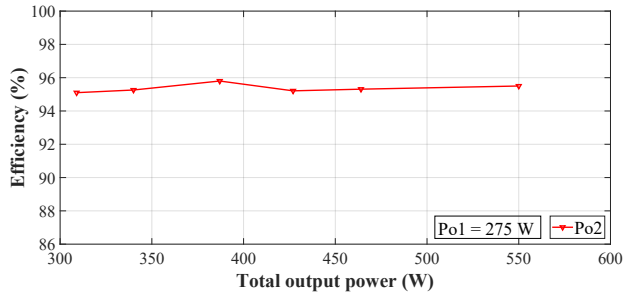

(b)

Figure 3.14: Overall efficiency of the system with variation in total output power. (a) P_{o1} varied with P_{o2} constant at 275W, (b) P_{o2} varied with P_{o1} constant at 275W.

component with negligible proportion of other harmonics. The experimental ZVS waveforms for the proposed 3SI is shown in Figure 3.9. It can be observed that all three MOSFETs operates in ZVS. The experimental efficiency for variable load powers is calculated and is as indicated in Figure 3.14. The total system efficiency for the variation in load-1 power is calculated by keeping load-2 at constant maximum power and vice versa. Figure 3.14(a) shows the efficiency of the system while power of load-1 is varied keeping load-2 constant at 275 W.

Figure 3.14(b) shows the efficiency of the system while load-2 power is varied with load-1 power maintained constant at 275 W. The proposed novel 3SI operates at greater than 95% efficiency over the entire range of operation with peak efficiency of 96.3%. Figure 3.15 shows the simulation and experimental plots for output power variation as a function of duty cycle. Variation in load-1 power P_{o1} is plotted in Figure 3.15(a), by maintaining duty cycle D_2 as constant at 99% and varying duty cycle D_1. Similarly, the variation in load-2 power P_{o2} is plotted in Figure 3.15(b), by maintaining duty cycle D_1 as constant at 99% and varying duty cycle D_2. The simulation and the experimental results for output power variation with change in duty cycle are in accord with one another.

Figure 3.16 shows thermal images of both the steel vessels which are used as loads after powering them at different duty cycle for one minute. Figure 3.16(a) and Figure 3.16(b)

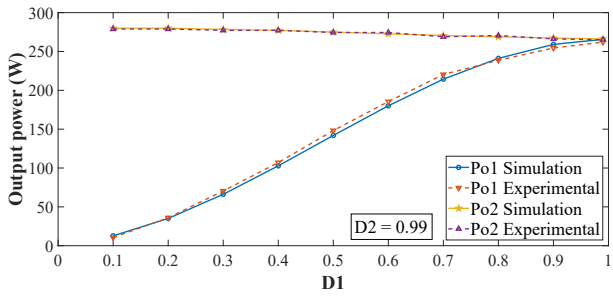

(a)

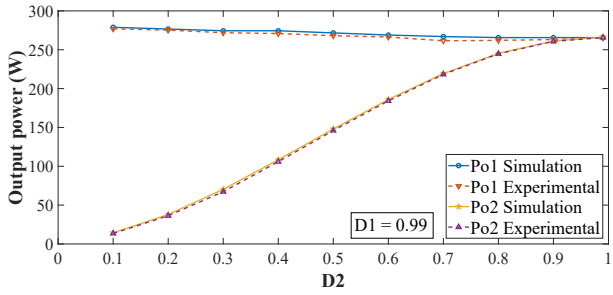

(b)

Figure 3.15: Simulation versus experimental results of output power variation with duty cycle. (a) D_1 varied with D_2 constant at D_{2max}, (b) D_2 varied with D_1 constant at D_{1max}

are thermal images for both the steel loads powered at 30%-70% and 70%-30% duty cycle combinations for one minute. Figure 3.16(c) are the thermal images of both the loads operated at 90% duty cycle.

3.6 Extension of the Proposed 3SI

The proposed configuration can be extended for multiple loads by adding three switches per two loads. Figure 3.17 shows extended configuration for four IH loads. Leg-1 with switches S_1, S_2 and S_3 can be used to control powers in load-1 and load-2. Leg-2 with switches S_4, S_5 and S_6 can be used to control powers in load-3 and load-4. Powers in each load can be independently controlled by using ADC control. Duty cycles of switches S_1, S_3, S_4, S_6 controls powers in load-1, load-2, load-3 and load-4 respectively. Each of these connected legs can be operated at different frequencies which makes this toplogy suitable for heating magnetic as well as non-magnetic materials.

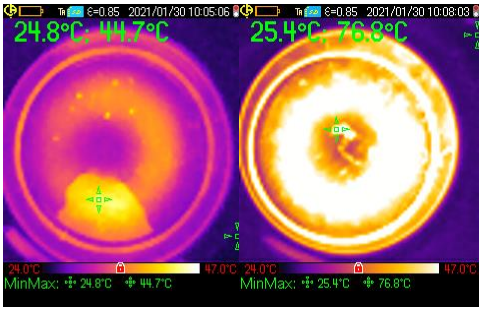

(a)

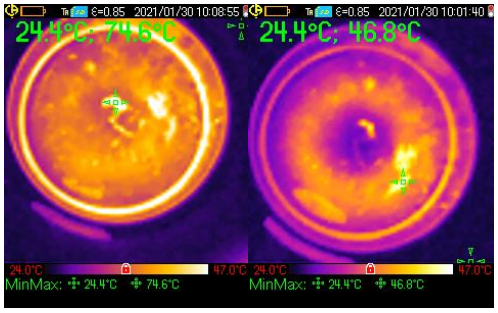

(b)

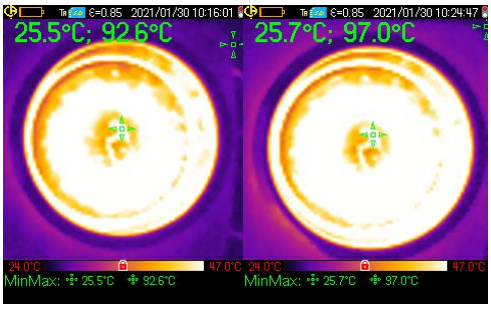

(c)

Figure 3.16: Thermal images for different duty cycles for load-1 and load-2. D_1 - D_2 combinations of (a) 30% - 70%, (b) 70% - 30%, (c) 90% - 90%.

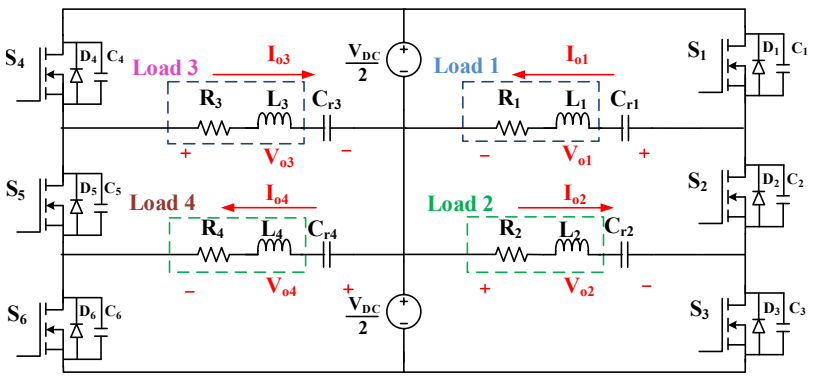

Figure 3.17: Extension of the proposed 3SI

Table 3.2: Comparison of the IH inverters

Sr. No.	No. of switches and diodes	Operating frequency (kHz)	Soft switching	Peak efficiency (%)	Independent control	Simultaneous control	Switch to load ratio	Suitable for IH load material type
[18]	8	48	Yes	-	Yes	Yes	4	FM
[58]	6	30	Yes	95	No	Yes	2	FM
[38]	4	30,150	Yes	92	Yes	Yes	2	FM and N-FM
[39]	5	25-125	Yes	96.5	Yes	No	5	FM and N-FM
[37]	3	23-75	No	96	Yes	No	3	FM and N-FM
[41]	8	20,100,400	No	$\geq$92	Yes	Yes	2.67	FM and N-FM
[42]	4	30/78	Yes	94.32	Yes	No	2	FM and N-FM
Proposed 3SI	3	28	Yes	96.3	Yes	Yes	1.5	FM
Extension of the proposed 3SI	3	28 and 150	Yes	-	Yes	Yes	1.5	FM and N-FM

3.7 Summary

In this chapter, the proposed three switch inverter configuration has been described in detail. Reduced number of components and high efficiency are the main benefits of the proposed inverter. ADC control technique has been used to independently and simultaneously regulate powers in two loads. The 3SI has been analysed and analytical expressions for output current, power and power losses have been derived. The 3SI operates at more than 95 % efficiency over the entire range of operation and it offers peak efficiency of 96.3 %. Also, it offers switch to load ratio of 1.5 which is lowest for multi-load IH applications. The extension of the proposed inverter for more loads is possible with low switch to load ratio of 1.5. The extended topology has an added advantage of operating each leg at different frequencies. And this makes it suitable for heating magnetic as well as non-magnetic materials. But with the extension, minimum component count for heating two different material IH loads is high. Comparison of the proposed 3SI with existing IH inverters has been presented in Table 3.2. The proposed 3SI offers compact and efficient solution to the multi-load IH applications.

Chapter 4

Full-bridge Based Multi-load Inverter Configuration for Vessels of Different Material Induction Cooking Application

Chapter 4

Full-bridge Based Multi-load Inverter Configuration for Vessels of Different Material Induction Cooking Application

4.1 Introduction

Most of the inverter topologies available in the literature are mostly suitable for FM loads only. Now, there is an increase in research for proposing inverter topologies suitable for heating FM as well as N-FM type vessels. In this chapter, a FB based multi-load inverter (FB-MI) configuration has been proposed which can heat FM and N-FM material vessels. The proposed inverter topology uses a basic FB inverter which can power any number of IC loads with an additional low frequency operated switching device and a diode for each IC load. A simple ON-OFF control is used for obtaining simultaneous as well as independent control for both the loads. It offers a linear power control. The range of power control for N-FM load is increased by using frequency based control. The proposed inverter circuit has been simulated in OrCAD PSpice and experimentally verified with a prototype for 1624 W. The proposed scheme for multiple load ICS for vessels of different material is presented in Figure 4.1.

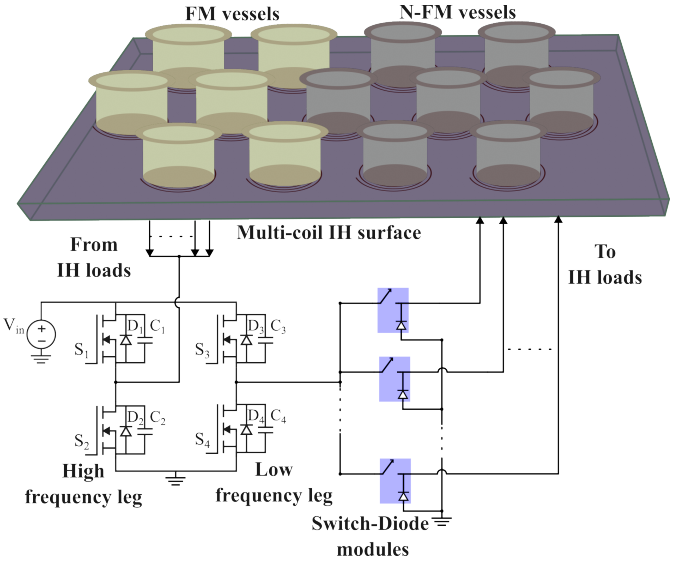

Figure 4.1: Proposed scheme for multi-load ICS for vessels of different material

Some key features of the proposed IC system solution are:

- Ability to heat both FM and N-FM loads, independent and simultaneous power control in multiple loads of different materials
- Independent and simultaneous power control in multiple loads of different materials
- Linear output power regulation with ON-OFF control technique
- Possibility for extension to more than two loads by a series low frequency operated switch and diode combination for each additional IC load.

Further, the chapter is subdivided into Section 4.2 to Section 4.5. Section 4.2 describes the proposed inverter circuit, gate pulses and modes of operation. Section 4.3 details the analysis of the inverter and its power control. In Section 4.4, simulation and experimental results are presented and operation of the proposed circuit is evaluated. Finally, important conclusions for the research work is presented in Section 4.5.

4.2 Proposed FB based Multi-load Inverter

The proposed inverter configuration for different material IC application is shown in Figure 4.2. It comprises of dc source (V_{dc}), six MOSFETs ($S_1, S_2, S_3, S_4, S_5, S_6$), two diodes ($D_7, D_8$) and two different material IC loads. Ferromagnetic load is modelled as 'R_f, L_f' and is resonated at a frequency $f_{r,lf}$ using resonant capacitor C_{r1}. Non-ferromagnetic load is modelled as 'R_{nf}, L_{nf}' and is resonated at a frequency $f_{r,hf}$ using resonant capacitor C_{r2}. As depicted in Figure 4.2, 'V_f, I_f' and 'V_{nf}, I_{nf}' are respective voltages and currents for FM and N-FM loads. The switches (S_1, S_2, S_3, S_4) forms two legs of the inverter. Leg-1 devices (S_1, S_2) are operated at a low frequency f_{lf} ($= 1/T_{lf}$), which is required for FM load. Leg-2 devices (S_3, S_4) are

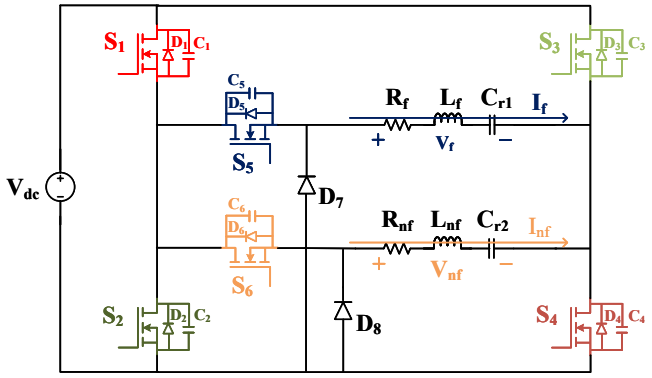

Figure 4.2: Proposed FB-MI configuration

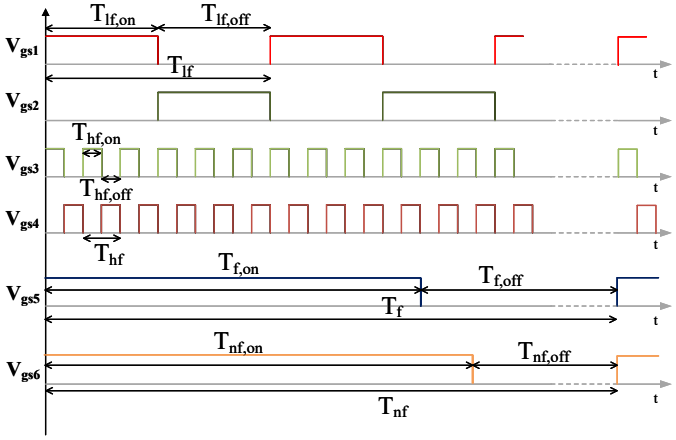

Figure 4.3: Gate pulses for the inverter switches

operated at a high frequency f_{hf} $(= 1/T_{hf})$, to meet the heating requirement of N-FM load. The powers in these two different loads are controlled using a series switch and a diode combination per load. The switch-diode combinations 'S_5, D_7' and 'S_6, D_8' are used to obtain independent power control in FM and N-FM loads respectively as shown in Figure 4.2.

The gate pulses for the proposed inverter circuit are shown in Figure 4.3. Low frequency gate pulses V_{gs1} & V_{gs2} are used for switching S_1 & S_2 respectively. T_{lf} is the time period of V_{gs1} and V_{gs2}. $T_{lf,on}$ and $T_{lf,off}$ are the on and off-time periods for V_{gs1} and V_{gs2} respectively. High frequency gate pulses V_{gs3} & V_{gs4} are used for switching S_3 & S_4 respectively. T_{hf} is the time period of V_{gs3} and V_{gs4}. $T_{hf,on}$ and $T_{hf,off}$ are the on and off-time periods for V_{gs3} and V_{gs4} respectively. The on-time periods $T_{lf,on}$ and $T_{hf,on}$ are fixed for the entire operation of the inverter, i.e., $T_{lf,on} = T_{lf}/2$ and $T_{hf,on} = T_{hf}/2$. V_{gs5} & V_{gs6} are used for switching S_5 & S_6 respectively. T_f is the time period of V_{gs5} and T_{nf} is the time period of V_{gs6}. $T_{f,on}$ and $T_{f,off}$ are the on and off time periods for V_{gs5}. $T_{nf,on}$ and $T_{nf,off}$ are the on and off time periods for V_{gs6}.

4.2.1 Operating modes

The operating modes of the proposed inverter are shown in Figure 4.4. Figure 4.4(a) to Figure 4.4(j) which correspond to Mode-1 to Mode-10 respectively.

Mode-1:

In this mode, switches S_1, S_4, S_5 and S_6 are ON. The FM load is powered by dc source through S_1, S_5 and S_4. The N-FM load is powered by dc source through S_1, S_6 and S_4. The current flow and the state of this mode is shown in Figure 4.4(a).

Mode-2:

In this mode, both the loads are disconnected from the supply as S_4 is turned OFF. Switches

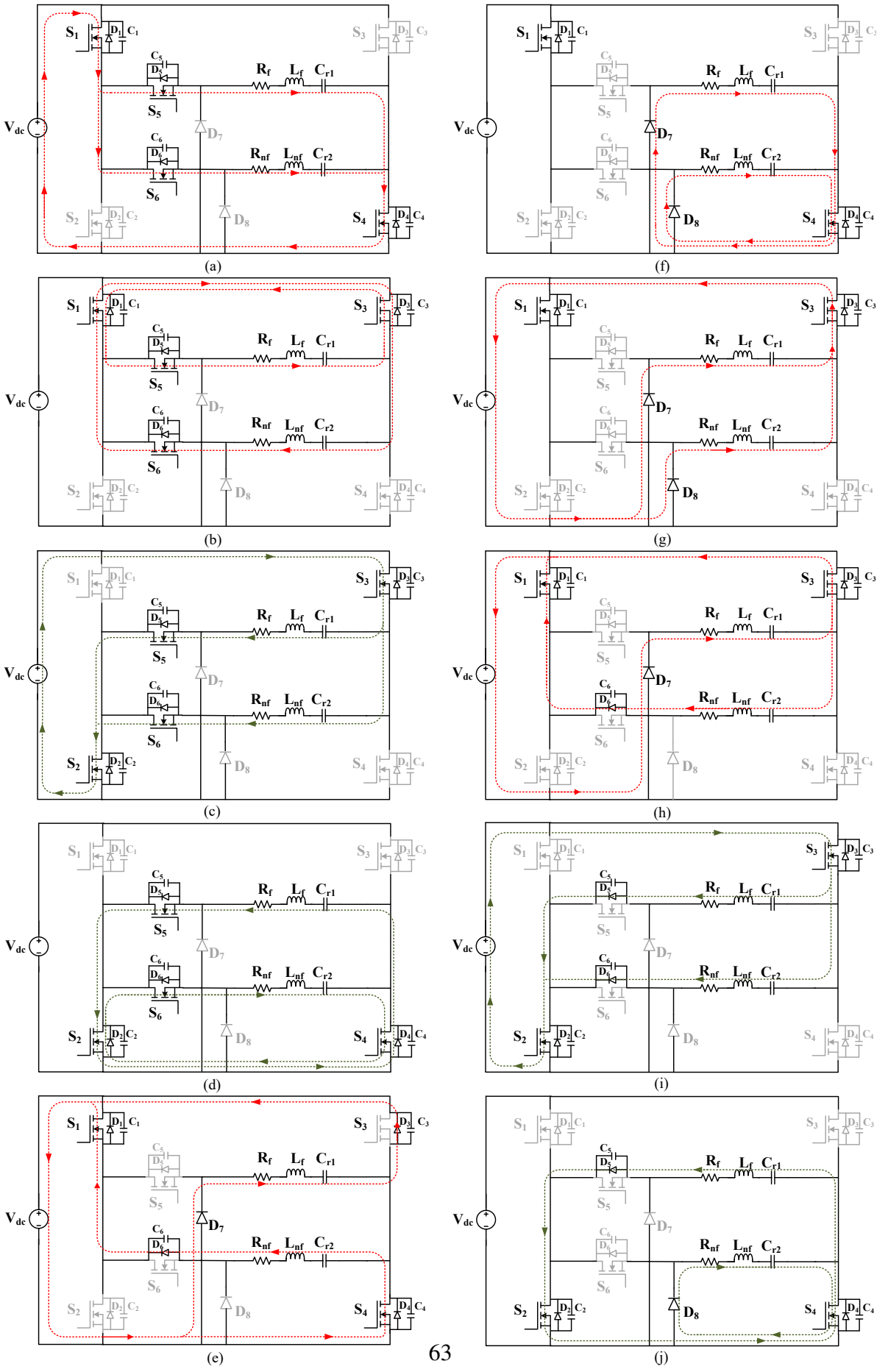

Figure 4.4: Operating modes of the proposed FB-MI

S_1, S_3, S_5 and S_6 are ON. FM load is freewheeling through S_1, S_5 and S_3. N-FM load current direction is reversed as the resonant capacitor C_{r2} discharges. The current in N-FM load flows through switches S_6, S_1 and S_3. The state of the circuit for this mode is depicted in Figure 4.4(b).

Mode-3:

In this mode, both the loads are powered from the supply as S_1 is turned OFF and S_2 is turned ON. The switches S_2, S_3, S_5 and S_6 are ON. The FM load is powered by dc source through S_3, S_5 and S_2. The N-FM load is powered by dc source through S_3, S_6 and S_2. The direction of the current flow in the FM and N-FM loads is reversed from the previous mode. The current flow and the state of this mode is shown in Figure 4.4(c).

Mode-4:

In this mode, both the loads are disconnected from the supply as S_3 is turned OFF. Switches S_2, S_4, S_5 and S_6 are ON. FM load is freewheeling through S_5, S_2 and S_4. N-FM load current direction is reversed as the resonant capacitor C_{r2} discharges. The current in N-FM load flows through switches S_6, S_2 and S_4. The state of the circuit along with the current flow directions for this mode is depicted in Figure 4.4(d).

Mode-5:

Switches S_1 and S_4 are ON in this mode. FM load current flows through D_3, V_{dc} and D_7. N-FM load current flows through D_6, S_1 and S_4. The flow of currents and the state of the inverter circuit for this mode are shown in Figure 4.4(e).

Mode-6:

Both the loads are freewheeling in this mode. Switches S_1, S_4 and diodes D_7, D_8 are conducing in this mode. FM load is freewheeling through S_4 and D_7. N-FM load is freewheeling through S_4 and D_8. The flow of load currents is shown in Figure 4.4(f). The series switches for both loads are OFF in this mode. As both the series switches are controlled independently, one can be ON and the other can be OFF at the same time. The direction of current will vary depending on the case.

Mode-7:

In this mode, switches S_1 and S_3 are ON. The current in FM load flows through D_7-S_3-V_{dc}. The magnitude of this current is low as FM load is tuned to low frequency. N-FM load current flows through D_8-S_3-V_{dc}. The operating state for this mode is shown in Figure 4.4(g).

Mode-8:

In this mode, switches S_1 and S_3 are ON. FM load current continues to flow as in the previous mode. Resonant capacitor C_{r2} drives the load current through D_6-S_1-S_3. The direction of the current flow and the operating state for the inverter is shown in Figure 4.4(h).

Mode-9:

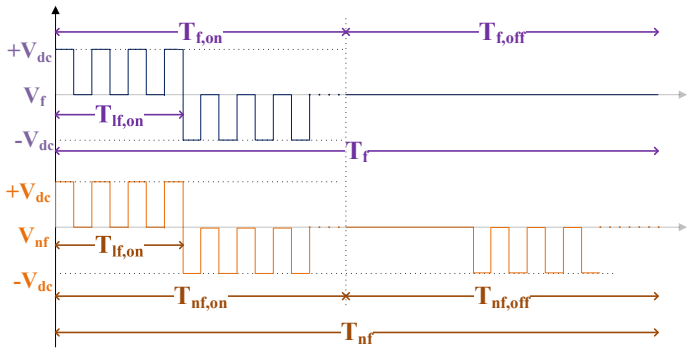

Figure 4.5: Approximated load voltage waveforms

In this mode, switches S_2 and S_3 are ON. The current in FM load flows through supply V_{dc}-S_3-D_5-S_2. The magnitude of this current will be low as FM load is tuned to low frequency. N-FM load is powered by dc source in this mode. The current flows through dc supply V_{dc}-S_3-D_6-S_2. The operating state of this mode is shown in Figure 4.4(i).

Mode-10:

In this mode, switches S_2 and S_4 are ON. FM load freewheels through D_5-S_2-S_4. Resonant capacitor C_{r2} discharges through S_4-D_8. The direction of the load current flow and the operating state for the inverter is shown in Figure 4.4(j).

From the different operating modes of the proposed inverter circuit, the following key observations can be made:

1. For Mode-1 to Mode-4, the inverter circuit operates as a full-bridge circuit with two legs operating at different frequencies.

2. By controlling series switches (S_5 and S_6), power can be controlled in both loads independently.

3. Even with a series switch in OFF condition, during negative half cycle i.e., when S_3 is ON, there is no control over current. However, current through FM load in this case is of very low magnitude as it is tuned to low frequency while $S_3 - S_4$ are switched at high frequency.

4. When series switch for N-FM load is OFF, it gets powered only during the negative half cycle i.e., when S_3 is ON. Whereas it discharges when S_3 is turned OFF and S_4 is ON. This leads to variation in current magnitude through N-FM load.

4.3 Output Power Control

For experimentation, FM steel vessel and N-FM aluminum vessel have been selected. The load parameters for the above mentioned loads are obtained using NumetriQ phase sensitive multimeter-PSM 1735. The characteristics showing variation of load equivalent inductance and equivalent resistance with operating frequencies are presented in Figure 1.10 of introduction

chapter.

4.3.1 Frequency selection

The operating frequencies of the loads are selected such that they offer nearly equal resistance. From Figure 1.10, it is observed that the equivalent resistance is 2.8 Ω for FM load at 30 kHz and for N-FM load at 220 kHz. Hence, FM load is operated at 30 kHz and N-FM load is operated at 220 kHz. These two different loads are resonated using series resonant capacitors C_{r1} and C_{r2} respectively such that the loads have resonant frequencies which are a little lower than their respective operating frequencies. The resonant frequencies for FM and N-FM loads respectively can be expressed as:

$$f_{r,lf} = \frac{1}{2\pi\sqrt{L_f C_{r1}}} \tag{4.1}$$

$$f_{r,hf} = \frac{1}{2\pi\sqrt{L_{nf} C_{r2}}} \tag{4.2}$$

As FM load is tuned at low frequency, it will not respond to high frequency and it offers high impedance for high frequency component. Similarly, as N-FM load is tuned at high frequency, it does not respond to low frequency and it offers high impedance for low frequency component.

4.3.2 Inverter analysis

The proposed circuit is analysed mathematically with the following assumptions: all the components are in their ideal state, current in FM load is zero when series switch S_5 is OFF and only fundamental frequency current is present in the loads.

4.3.2.1 FM load power

FM load is powered only when its series switch S_5 is ON. The fundamental component of the output voltage v_f shown in Figure 4.5, can be expressed during ON state as:

$$v_{f,1} = \frac{2V_{dc}}{\pi}\cos(\omega t - \pi\frac{T_{lf,on}}{T_{lf}}) \tag{4.3}$$

The rms current of the fundamental component can be represented as:

$$I_{f1,rms} = \frac{V_{f1,rms}}{|Z_{f1}|} = \frac{\sqrt{2}V_{dc}}{\pi|Z_{f1}|} \tag{4.4}$$

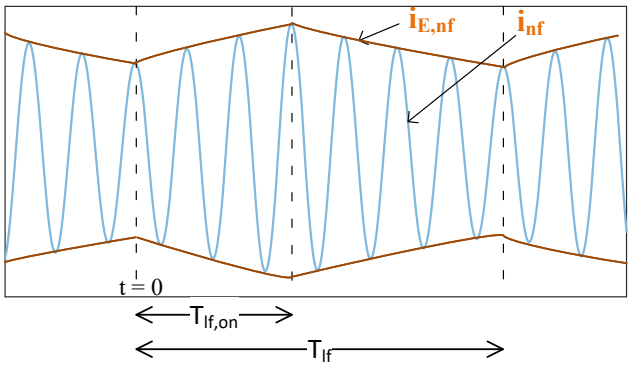

Figure 4.6: N-FM load current envelope when S_6 is OFF

The average power responsible for heating steel load is given by:

$$P_{st} = I_{f1,rms}^2 \times R_f \times d_1 = \frac{2(V_{dc})^2}{\pi^2 |Z_{f1}|^2} \times R_f \times D_1 \tag{4.5}$$

where, d_1 is the duty cycle for ON-OFF control in steel load and is:

$$D_1 = \frac{T_{f,on}}{T_f} \tag{4.6}$$

Z_{f1} is the impedance for the fundamental current component in the steel load and can be given as

$$Z_{f1} = R_f + j\left(\omega L_f - \frac{1}{\omega C_{r1}}\right) \tag{4.7}$$

4.3.2.2 N-FM load power

N-FM load is powered fully when S_6 is ON. When S_6 is turned OFF, the N-FM load is partially powered. The detailed analysis is described as follows:

When S_6 is ON, the output voltage waveform is shown in Figure 4.5. The fundamental component of the output voltage v_{nf} shown in Figure 4.5, can be expressed during ON state as

$$v_{nf,1} = \frac{2V_{dc}}{\pi} \cos(\omega t - \pi \frac{T_{hf,on}}{T_{hf}}) \tag{4.8}$$

The rms current of the fundamental component is given as

$$I_{nf1,rms} = \frac{V_{nf1,rms}}{|Z_{nf1}|} = \frac{\sqrt{2}V_{dc}}{\pi |Z_{nf1}|} \tag{4.9}$$

The average power delivered to N-FM load with S_6 ON is:

$$P_{al,ON} = I_{nf1,rms}^2 \times R_{nf} \times d_2 = \frac{2(V_{dc})^2}{\pi^2 |Z_{nf1}|^2} \times R_{nf} \times D_2 \tag{4.10}$$

where, d_2 is the duty cycle for ON-OFF control in aluminium load and is given as:

$$D_2 = \frac{T_{nf,on}}{T_{nf}} \tag{4.11}$$

Z_{nf1} is the impedance for the fundamental component current in the aluminium load and represented as:

$$Z_{nf1} = R_{nf} + j\left(\omega L_{nf} - \frac{1}{\omega C_{r2}}\right) \tag{4.12}$$

During the OFF duration of S_6, the N-FM load is not powered as long as S_1 is ON. During this state, N-FM load is freewheeling and it returns power back to the source for a very short duration. This clamps the output voltage at $\pm V_{dc}$ which can be observed in the simulation and experimental results. As the average power returned to the source is very low, it is not considered in power calculations. The approximated waveforms are shown in Figure 4.5. When S_1 turns OFF and S_2 is ON, N-FM load is again powered which leads to an increase in load current. Due to the above mentioned reason, the N-FM load current exhibits oscillatory envelope ($i_{E,nf}$) as shown in Figure 4.6. The time constant 'τ' of the envelope is $\frac{2L_f}{R_f}$. Using the detailed approach mentioned in [59], the average power when S_6 is OFF is given by:

$$\begin{aligned} P_{al,OFF} &= \left(\frac{V_{dc}}{\pi}\cos\theta \frac{1}{T_{lf}} \int_0^{T_{lf,on}} i_{E,nf}(t)dt\right) \times (1 - D_2) \\ &= \left[P_{al,max}\frac{T_{lf,on}}{T_{lf}} + \frac{\tau}{T_{lf}}\left(\frac{1 - e^{\frac{-T_{lf,on}}{\tau}}}{1 - e^{\frac{-T_{lf}}{\tau}}}\right)\right. \\ &\quad \left.\left(e^{\frac{-T_{lf,on}}{\tau}} - e^{\frac{-T_{lf}}{\tau}}\right)\right] \times (1 - D_2) \end{aligned} \tag{4.13}$$

where $P_{al,max} = (1/\pi)V_{dc}I_{nf1,m}\cos\theta$ is the maximum output power for aluminium when $T_{lf,on} = T_{lf}$. And θ is the angle between output voltage and load current. The maximum current can be derived using Fourier analysis and is given by:

$$I_{nf1,m} = \frac{2V_{dc}}{\pi |Z_{nf1}|} \tag{4.14}$$

Now, using equations 4.10 and 4.13, the total average power responsible for heating the

N-FM load (aluminium) is given by:

$$P_{al} = P_{al,ON} + P_{al,OFF} \tag{4.15}$$

4.3.3 Power control

For the above analysis, the gate pulses for leg-1 and leg-2 switches are operated with fixed duty cycles of 50%. Hence,

$$T_{lf,on} = \frac{T_{lf}}{2}; \qquad T_{hf,on} = \frac{T_{hf}}{2} \tag{4.16}$$

Leg-1 and leg-2 switches are operating at 30 kHz and 220 kHz respectively. From equations 4.5 and 4.13, it can be observed that output powers of both the loads are related to the duty cycles of their respective series switches. So, for the respective load regulation, ON-OFF control is realised by varying respective series switch duty-cycles. Series switches S_5 and S_6 are operated

Table 4.1: Parameters for proposed FB-MI circuit.

Component	**Value**
DC supply voltage, V_{dc}	150V
equivalent resistance of FM load, R_f	2.8 Ω
equivalent inductance of FM load, L_f	65.8 μH
parasitic resistance of FM IH coil, $r_{f,coil}$	90 $m\Omega$
resonant capacitor of FM load, C_{r1}	0.52 μF
equivalent series resistance of C_{r1}, r_{cr1}	6.7 $m\Omega$
equivalent resistance of N-FM load, R_{nf}	2.8 Ω
equivalent inductance of N-FM load, L_{nf}	54.3 μH
parasitic resistance of N-FM IH coil, $r_{nf,coil}$	90 $m\Omega$
resonant capacitor of N-FM load, C_{r2}	10 nF
equivalent series resistance of C_{r2}, r_{cr2}	1.5 $m\Omega$
low switching frequency, f_{lf}	30 kHz
high switching frequency, f_{hf}	220 kHz
load ON-OFF control frequencies, f_{st} and f_{al}	1 kHZ
switching devices, MOSFETs	IRFP4127PbF
drain-source resistance for MOSFETs	17 $m\Omega$
diodes, D_7 and D_8	RURG5060

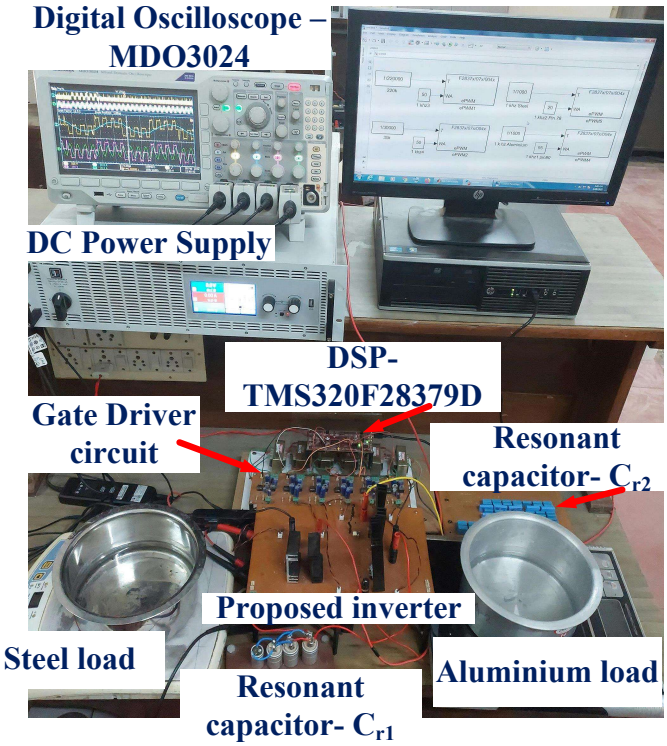

Figure 4.7: Laboratory experimentation setup

at 1 kHz. For FM load, full range power control is possible using 4.5. But for N-FM load, some minimum power is present even when the respective duty cycle is zero 4.13. Hence, for increasing the range of power control, frequency based control is implemented. By varying the operating frequency of leg-2, the operating point on the respective resonant curve changes as per equation 4.2. This leads to a change in the load current. By using this frequency control, the power regulation range is increased for N-FM load.

4.4 Simulation and Experimentation

The operation of the proposed FB-MI configuration has been verified through simulation and experiments for the parameters mentioned in Table 4.1. OrCAD PSpice software has been used for simulation. The laboratory experimentation setup for the proposed inverter configuration is presented in Figure 4.7. DC source EA-PSI 9750-40 is used for testing the experimental prototype. FM load is realised by using a combination of steel vessel and an IC coil and it has been modelled as R_f-L_f combination. For N-FM load, an aluminium vessel and an IH coil is used and it has been modelled as R_{nf}-L_{nf} combination. MKV-B25834 type capacitors are used for realising resonant capacitor C_{r1}. Series-parallel combinations of MKP-B32672L type capacitors are used for obtaining the required value of C_{r2}. Digital signal processor-TMS320F28379D is used to control the proposed inverter circuit. All the experimental results are captured using

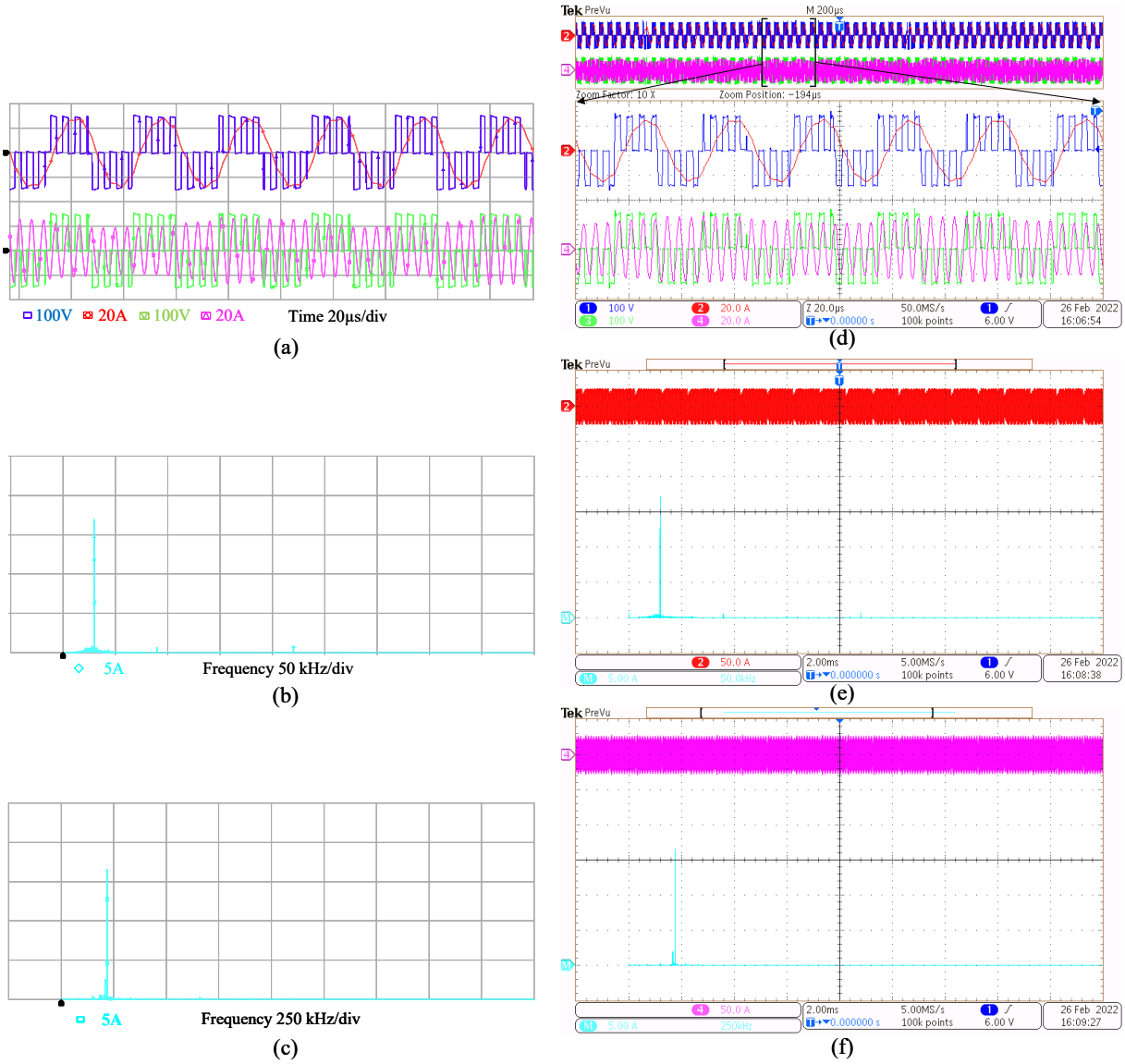

Figure 4.8: Simulation and experimentation results when P_{st} = 838 W and P_{al} = 786 W. (a) and (d): Respectively simulation and experimental voltage-current waveforms of steel and aluminum loads, (b) and (e): simulation and experimental FFTs of steel load current, (c) and (f): simulation and experimental FFTs of aluminum load current

MDO 3024 at 200 MHz bandwidth. Independent power control of FM and N-FM IC loads is obtained using ON-OFF control. With ON-OFF control, some minimum power is present in the N-FM load due to absence of control in the negative half cycle. To control power in N-FM load below the minimum value, frequency control is also implemented.

Figure 4.8 depicts the simulation and experimental results when both the loads are operated at their respective full powers. Duty cycles for both loads are at 99%. The current flowing through steel load is 17.3 A, while that of the aluminium load is 16.75 A. Steel load is powered at 838 W and aluminium load is powered at 786 W. The total output power delivered by the

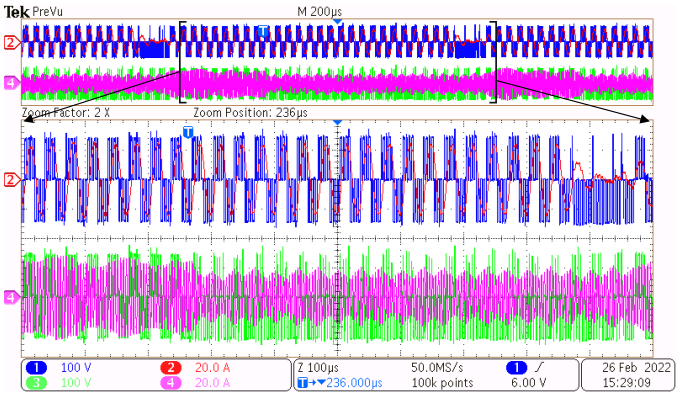

(a)

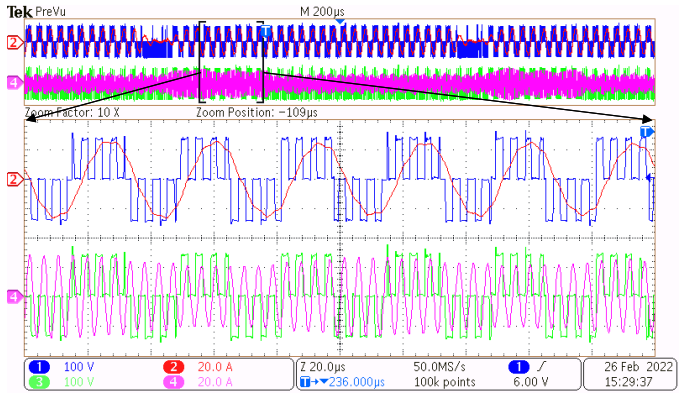

(b)

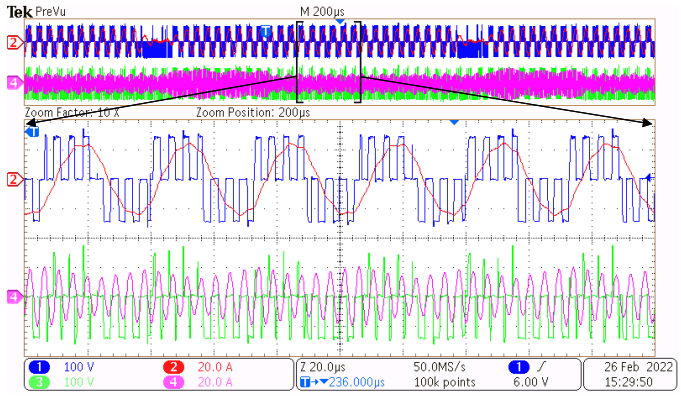

(c)

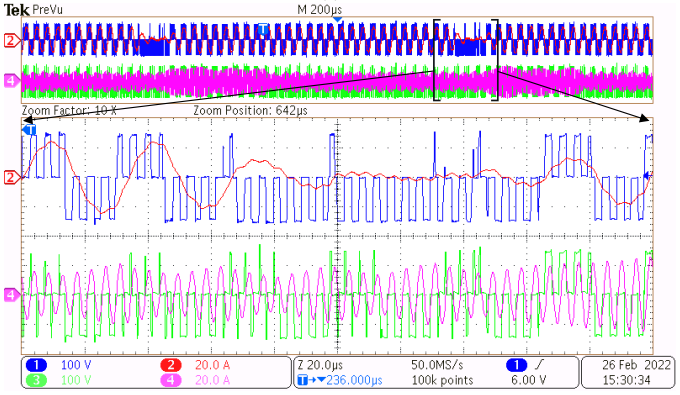

(d)

Figure 4.9: Experimental voltage-current waveforms of steel and aluminum loads when P_{st} = 744.85 W and P_{al} = 508.79 W.

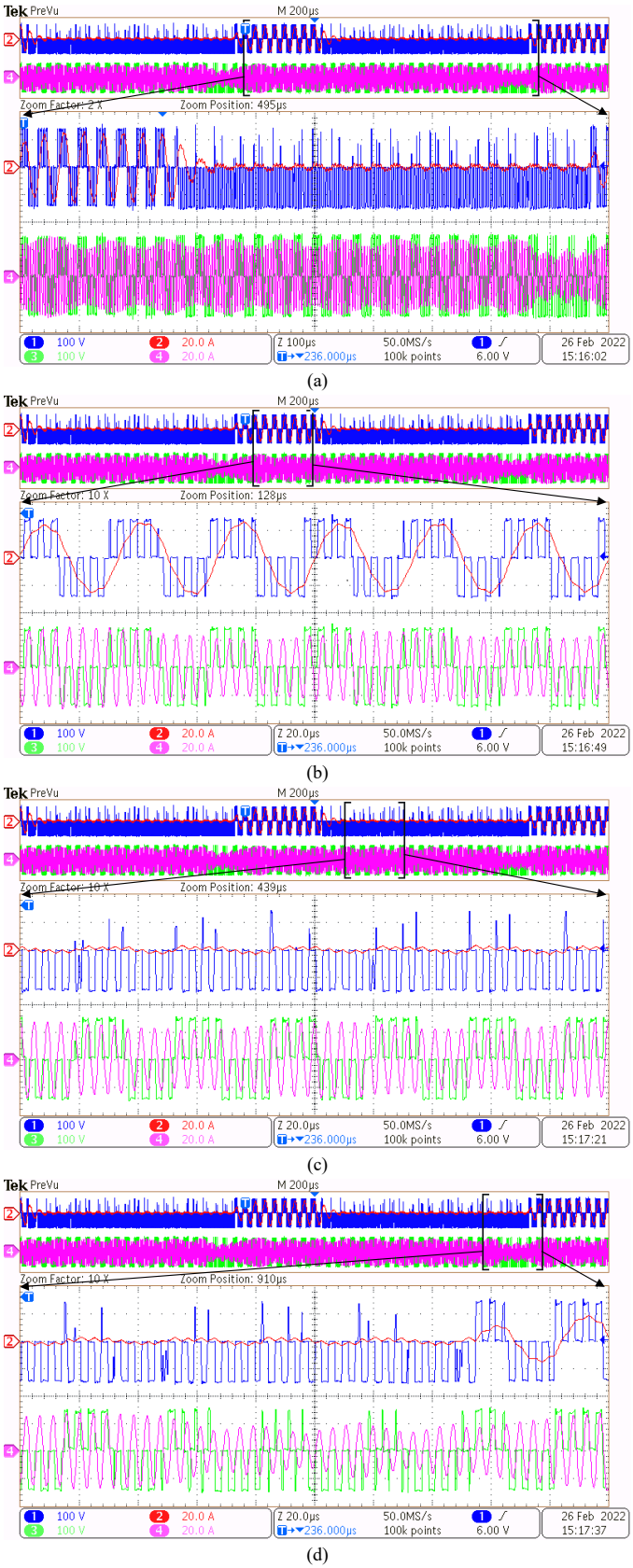

Figure 4.10: Experimental voltage-current waveforms of steel and aluminum loads when P_{st} = 261.28 W and P_{al} = 526.3 W.

inverter circuit is 1624 W. Figure 4.8(a) to Figure 4.8(c) show the simulation results while Figure 4.8(d) to Figure 4.8(f) show experimental results. Figure 4.8(a) and Figure 4.8(d) show the output voltage-current waveforms of the loads under simulation and experimentation respectively. Figure 4.8(b) and Figure 4.8(e) show FFTs of the current flowing through the steel load under simulation and experimentation respectively. Figure 4.8(c) and Figure 4.8(f) show FFTs of the current flowing through the aluminum load under simulation and experimental conditions respectively.

Figure 4.9 shows experimental results when the inverter is delivering total output power of 1253.64 W. Steel load is operated with duty cycle d_1 of 90% and rms current flowing through it is 16.31 A. It is powered at 744.85 W. Aluminium load is operated with a duty cycle d_2 of 30% and rms current flowing through it is 13.48 A. It is powered at 508.79 W. Figure 4.9(a) shows the output voltage and load current waveforms for one cycle of ON-OFF control pulses with frequency (f_{st} & f_{al}) of 1 kHz. Figure 4.9(b) shows the zoomed view of the respective output voltage and load current waveforms during experimentation when both loads are powered simultaneously. Figure 4.9(c) shows the zoomed view of the experimental output voltage and load current waveforms. It indicates the state when the series switch for steel load (S_5) is ON but series switch for aluminium load (S_6) is OFF. Figure 4.9(d) shows a zoomed view of the waveforms when series switches of both the loads are OFF.

Figure 4.10 shows the experimental results of the inverter circuit when d_1 is 30% and d_2 is 90%. The rms values of the currents flowing through steel and aluminium loads are 9.66 A and 13.71 A respectively. Steel and aluminium loads are controlled at powers of 261.28 W and 526.3 W respectively. Figure 4.10(a) shows the voltage-current waveforms of the loads for one cycle of ON-OFF control. Figure 4.10(b) shows the zoomed view of voltage-current waveforms when both the series switches are ON. Figure 4.10(c) shows the zoomed view of voltage-current waveforms when series switch of the steel load is OFF while that of aluminium load is ON. Figure 4.10(d) shows the zoomed view of voltage-current waveforms when both the series switches are in OFF state.

The variation in output power with ON-OFF control is plotted in Figure 4.11 and Figure 4.12. Figure 4.11 shows simulation and experimental results when output power is varied over d_1 by keeping d_2 constant at 99%. By varying d_1 from 10% to 99%, steel load power is varied from 84.7 W to 838 W while aluminium load power remains almost constant at its maximum value. Figure 4.12 shows simulation and experimental results when the output power is varied over d_2 keeping d_1 constant at 99%. By varying d_2 from 10% to 99%, aluminium load power is varied from 312.24 W to 786 W while steel load power remains almost constant at its maximum value. Linear power control for both loads is independently obtained by using on-off

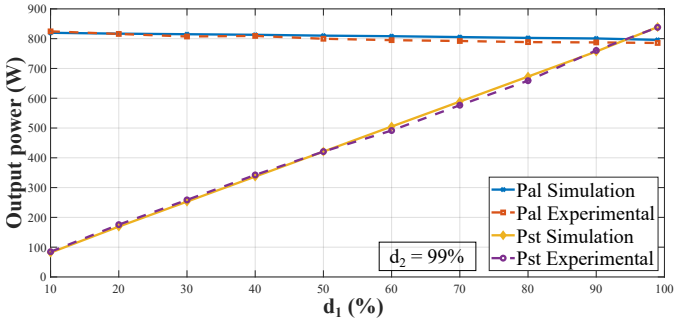

Figure 4.11: Output power variation with d_1

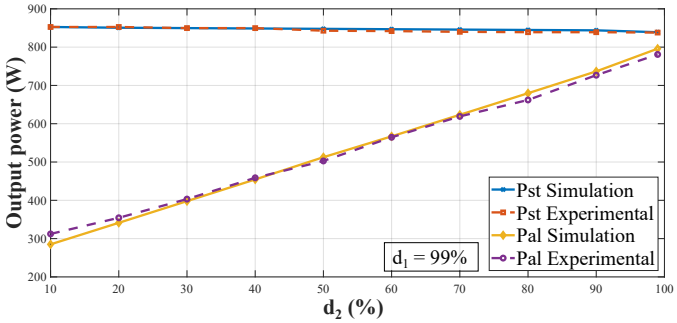

Figure 4.12: Output power variation with d_2

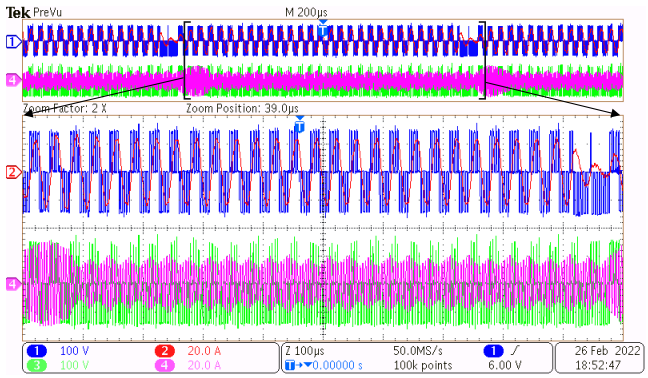

Figure 4.13: Experimental voltage-current waveforms for steel and aluminium loads at 220 kHz with $d_1 = 95\%$ and $d_2 = 10\%$.

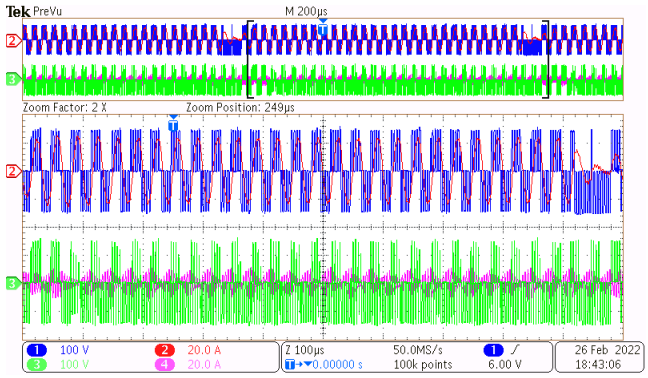

Figure 4.14: Experimental voltage-current waveforms for steel and aluminium loads at 234 kHz when $d_1 = 95\%$ and $d_2 = 10\%$.

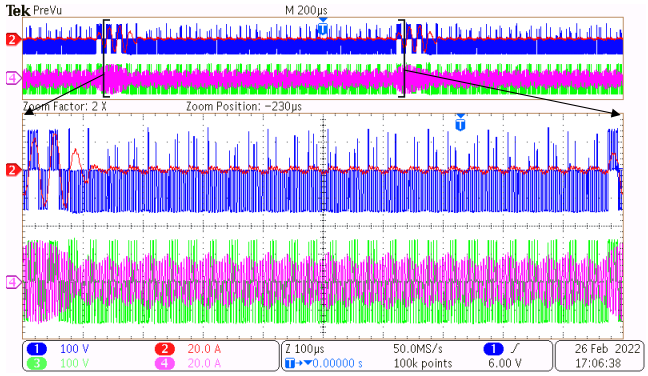

Figure 4.15: Experimental voltage-current waveforms for steel and aluminium loads at 220 kHz with $d_1 = 10\%$ and $d_2 = 10\%$.

control as shown in these graphs.

The experimental results for frequency based control of aluminium load when $d_1 = 95\%$ and $d_2 = 10\%$ are shown in Figure 4.13 and Figure 4.14. Figure 4.13 shows experimental output voltage-current waveforms when leg-2 is operated at 220 kHz. The rms current flowing through steel and aluminium loads are 17 A and 10 A respectively. Steel load is powered at 809.2 W and aluminium load is controlled at 280 W. Figure 4.14 shows the experimental waveforms for output voltage and load current when control frequency is 234 kHz. The rms current flowing through steel and aluminium loads are 17.12 A and 5.01 A respectively. Steel load is powered at 820 W and aluminium load is controlled at 70.28 W. Figure 4.15 and Figure 4.16 show the experimental voltage-current waveforms for steel and aluminium load. Both the loads are operated with duty cycle of 10% i.e., $d_1 = d_2 = 10\%$. Figure 4.15 shows waveforms when the steel load current is 5.4 A, powering it at 81.65 W and the aluminium load current is 9.7 A, controlling it at 263.45 W. Figure 4.16 shows waveforms when the steel load current is 5.41 A, powering it at 81.95 W and aluminium load current is 5.01 A, controlling it at 70.28 W. From simulation and experiment based results, it can be noted that both are in good accord with

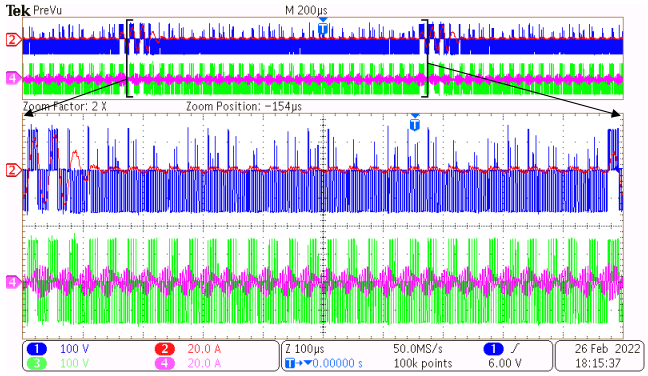

Figure 4.16: Experimental voltage-current waveforms for steel and aluminium loads at 234 kHz with $d_1 = 10\%$ and $d_2 = 10\%$.

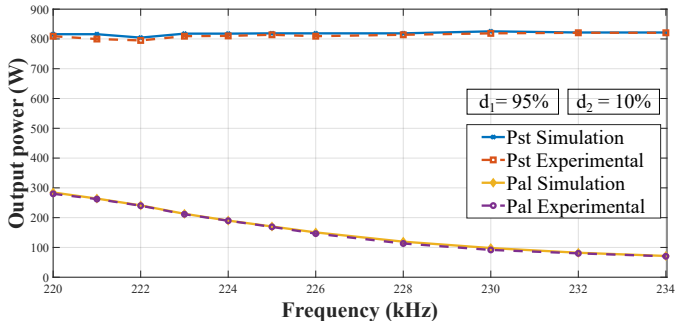

Figure 4.17: Output power variation with high frequency when $d_1 = 95\%$ and $d_2 = 10\%$

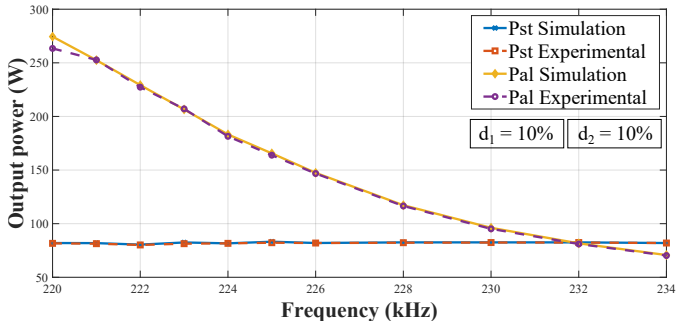

Figure 4.18: Output power variation with high frequency when $d_1 = 10\%$ and $d_2 = 10\%$

each other. It shows independent power control in steel and aluminium loads using ON-OFF control. The power control range for aluminium load is increased by incorporating frequency based control.

The frequency control for aluminum load is depicted in Figure 4.17 and Figure 4.18. Figure 4.17 shows the output power versus frequency graph for simulation and experimentation results when $d_1 = 95\%$ and $d_2 = 10\%$. The aluminium load power varies from 280 W to 70.28 W as leg-2 (S_3, S_4) frequency is varied from 220 kHz to 234 kHz. The power in the steel load reports a small variation from 809.2 W to 820 W. It can be observed that steel load power is maintained almost constant during the entire range of aluminium load power control. Figure 4.18 shows the output power variation over frequency when $d_1 = 10\%$ and $d_2 = 10\%$. The curves related to simulation and experimental results are plotted in this graph. The aluminium load power varies from 263.45 W to 70.28 W as leg-2 (S_3, S_4) frequency is varied from 220 kHz to 234 kHz. The power in the steel load has a small variation from 81.65 W to 81.95 W. It can be observed that steel load power is maintained almost constant during the entire range of aluminium load power control. Simulation and experimental data for both these graphs are in agreement with each other.

4.4.1 Loss analysis

The losses in the inverter can be categorized into conduction and switching losses. The conduction losses are due to parasitic resistances of the different components present in the circuit. Switching losses refers to the losses during the high frequency switching transitions in MOSFETs. The voltages and currents of switching devices S_1 and S_4 with $d_1 = 30\%$ and $d_2 = 90\%$ are shown in Figure 4.19. The soft switching (S) and hard switching (H) transitions are also indicated. It can be observed that due to lagging nature of load currents, soft switching (ZVS) is obtained during turn-on for most of the switching transitions. Hence, switching losses due to turn-on of devices can be ignored. Hard switching is present during turn-off of the switching devices. As the proposed inverter operation is similar to a combination of two half bridges operating at high and low frequencies, the turn-off losses can be derived using detailed explanation given in [60]. Hence, the turn-off losses can be evaluated as follows:

$$\begin{aligned} P_{\_off} = & f_{hf} V_{dc} I_{off,hf} \left(\frac{2t_{r,hf}}{3} + t_{f,hf} \right) \\ & + f_{lf} V_{dc} I_{off,lf} \left(\frac{2t_{r,lf}}{3} + t_{f,lf} \right) \end{aligned} \tag{4.17}$$

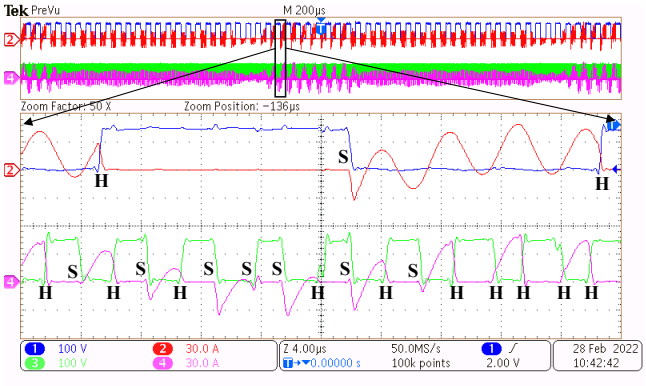

(a) S_5 and S_6 are ON

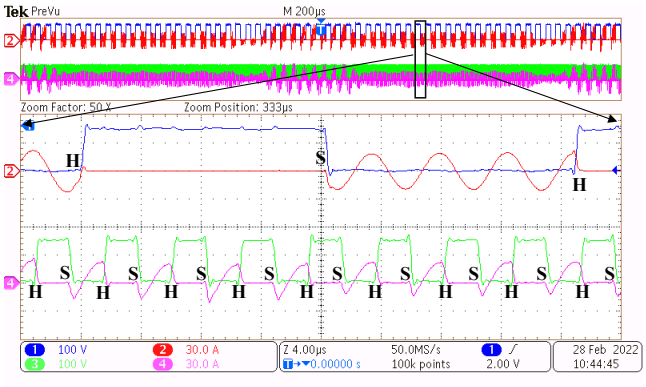

(b) S_5 is OFF and S_6 is ON

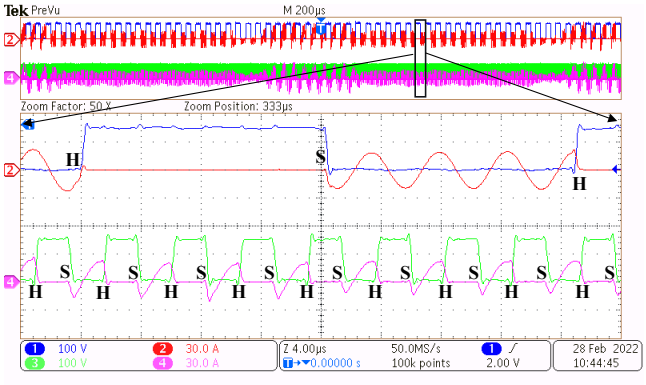

(c) S_5 and S_6 are OFF

Figure 4.19: From top to bottom: voltages and currents of switching devices S_1 and S_4. S: soft switching, H: hard switching

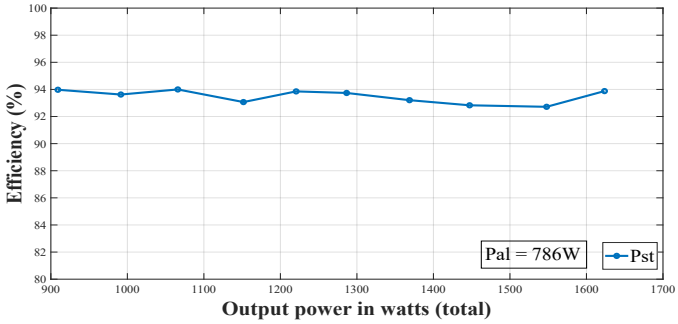

Figure 4.20: Efficiency versus output power. P_{st} is varied while P_{al} is controlled at 786 W

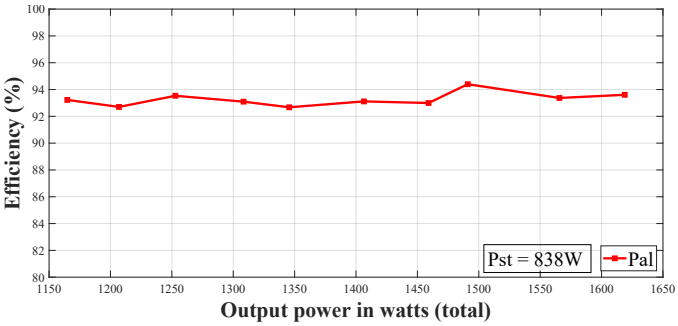

Figure 4.21: Efficiency versus output power. P_{al} is varied while P_{st} is controlled at 838 W

where, f_{hf} and f_{lf} are high and low switching frequencies respectively. $I_{off,hf}$ and $I_{off,lf}$ are turn-off currents of switching devices of high frequency and low frequency legs respectively. The $t_{r,hf}$ and $t_{r,lf}$ are rise time for device voltage of high and low frequency legs respectively. The $t_{f,hf}$ and $t_{f,lf}$ are device current fall times of high and low frequency legs respectively.

Efficiency of the proposed FB-MI over entire power range is shown in Figure 4.20 and Figure 4.21. Figure 4.20 depicts the efficiency versus steel load power while keeping aluminium load power constant at its maximum value of 786 W. It is observed that inverter efficiency is high which is around 94% for a wide range of output power. Figure 4.21 shows the efficiency versus aluminium load power with keeping steel load power at its maximum value of 838 W. It is observed that inverter efficiency is high which is around 93% for a wide range of output power. Hence, the proposed inverter offers more than 92.5% efficiency over the entire power control range and also peak efficiency of 94.3%. The efficiency is evaluated as the ratio of output power ($I^2_{f,rms}R_f + I^2_{nf,rms}R_{nf}$) to input power ($V_{dc}I_{dc}$). Figure 4.22 shows thermal images for steel and aluminium load when they are operated at 60% and 90% duty cycles respectively for a minute.

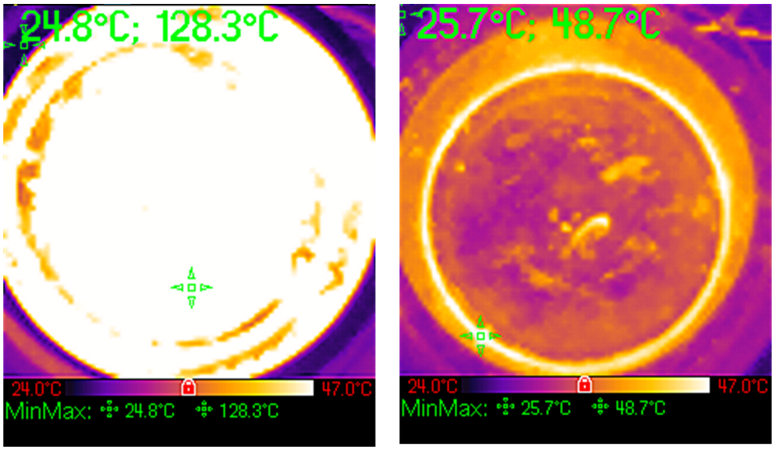

Figure 4.22: Thermal images for the steel and aluminium loads at $d_1 = 60\%$ and $d_2 = 90\%$ respectively

4.4.2 Comparison of the proposed FB-MI with existing inverters

The features of the proposed FB-MI have been compared with the recently proposed inverter topologies available in literature which are suitable for FM and N-FM IH loads. The comparison is described in Table 4.2. In [37], [39] and [42] the authors' primary objective is to propose universal IH solution i.e., one vessel at a time (FM or N-FM). In [41] and [38], the authors aimed for heating FM and N-FM loads simultaneously i.e., multiple load IH solutions. It can be observed from Table 4.2 that the above-mentioned inverter topologies use non-linear control which is not desirable. Some of them do not offer simultaneous operation and control of IH loads. In some of the proposed topologies, the control is more involved. Also, extension for multiple loads (more than 2) leads to increase in component count and hence size of the solution. The proposed inverter can be easily extended for more loads by the addition of a series switch and a diode per IH load. It also offers linear, independent and simultaneous control for all IH loads.

Table 4.2: Comparison of the IH inverters suitable for FM and N-FM loads

Sl. No.	No. of switches	Operating frequency (kHz)	Peak efficiency (%)	Control technique used	Control complexity	Independent/ simultaneous control	Additional no. of switches per load (>2 loads)
[37]	2	23-75	96	Selective harmonic, non-linear	Less	Yes/No	2 + relay
[39]	4	25-125	96.5	LAM, non-linear	High	Yes/No	4 + relay
[38]	4	30 & 150	92	ADC, non-linear	Less	Yes/Yes	2
[41]	8	20,100,400	$\geq$92	ADC, non-linear	Moderate	Yes/Yes	2
[42]	4	30/78	94.32	PWM + PSC, non-linear	Moderate	Yes/No	4 + relay
Proposed	6	30 & 220	94.3	ON-OFF, linear	Less	Yes/Yes	1 + diode

4.5 Summary

The proposed inverter circuit for heating vessels of different materials with ON-OFF control for multi-load application is described in this chapter. For both the different material loads, linear power variation is obtained using ON-OFF control independently. The range of power control for an aluminum load has been increased by implementing frequency based control. The operation of the proposed inverter has been validated through simulations and experiments. The designed experimental prototype has been tested for a total output power of 1624 W. It offers higher efficiency over the entire range of power control. Performance comparison of the proposed inverter is presented in Table 4.2. Simple, linear, simultaneous and independent power control in vessels of different material are key advantages of the proposed inverter circuit for multiple load IC application. It can also be used for heating more number of loads by adding a low frequency series switch and a diode combination per load which makes it suitable for multi-load IC applications. The minimum number of devices required for heating two different loads is six which is a bit higher compared to some of the existing topologies. However for the additional loads, the number of components required per load is less as compared with other topologies.

Chapter 5

Three Switch Dual Frequency Resonant Inverter for Different Material Induction Cooking Application

Chapter 5

Three Switch Dual Frequency Resonant Inverter for Different Material Induction Cooking Application

5.1 Introduction

In this chapter, a three switch dual frequency resonant inverter (3S-DFRI) has been proposed. It uses three switches to simultaneously power and control two different material IH loads. When compared to the inverter proposed in Chapter 4, 3S-DFRI has reduced number of switching devices. It provides two HB inverter operation with three switches. It generates two different frequency components in the output to meet heating requirements of FM and N-FM materials. The inverter operation is verified by rigorous simulation and experimentation on the developed 2 kW prototype. It can also be extended for multiple loads with additional inverter legs each having three switches. Each additional leg provides two independent load operation. The key advantages offered by the proposed inverter with dual frequency control are as below:

i) Reduced device count for multi-load different material induction cooking applications.

ii) Simultaneous as well as independent control for multi-load IH applications.

iii) Soft-switching operation for increasing efficiency.

iv) Extension with additional three switches for two different IH loads.

v) No requirement for electro-mechanical switches.

Further, this chapter is organised from Section 5.2 to Section 5.7. Section 5.2 describes the inverter topology with control. Operating modes of the inverter are discussed in Section 5.3. Mathematical expressions for output power control is derived in Section 5.4. Experimental results are discussed in Section 5.5. Extension of the inverter is discussed in Chapter 5.6. Major conclusions are presented in Section 5.7.

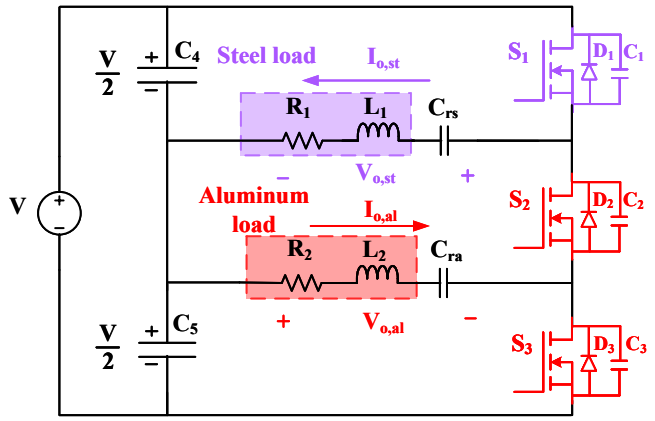

Figure 5.1: Proposed three switch dual frequency resonant inverter

5.2 Inverter Topology and Control Technique

Circuit diagram of the proposed resonant inverter is as shown in Figure 5.1. It comprises of a dc source (V), split capacitors (C_4 and C_5), three switching devices (S_1, S_2 and S_3) and two different material IC loads (steel and aluminum) with their respective series resonant capacitors. Steel and aluminum loads are modelled as '$R_1 - L_1$' and '$R_2 - L_2$' respectively. Capacitors C_{rs} and C_{ra} resonate steel and aluminum load at their respective resonant frequencies.

The proposed control logic is presented in Figure 5.2. It generates gate pulses for the three switching devices as shown in Figure 5.3. This control meets the different frequency heating requirement of the ferro and non-ferromagnetic material IC loads with three switches. The switching frequency of S_1 decides the operating frequency for steel load. The switching frequency of S_2 and S_3 when S_1 is ON decides the operating frequency for aluminum load. The control parameters for the two IC loads can be given as follows.

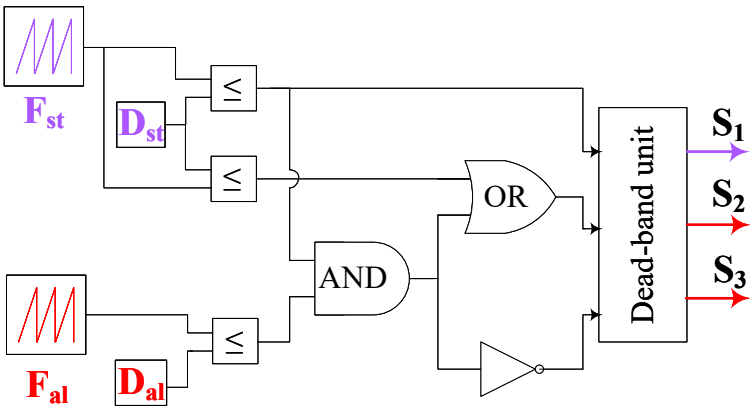

Figure 5.2: Dual frequency control logic

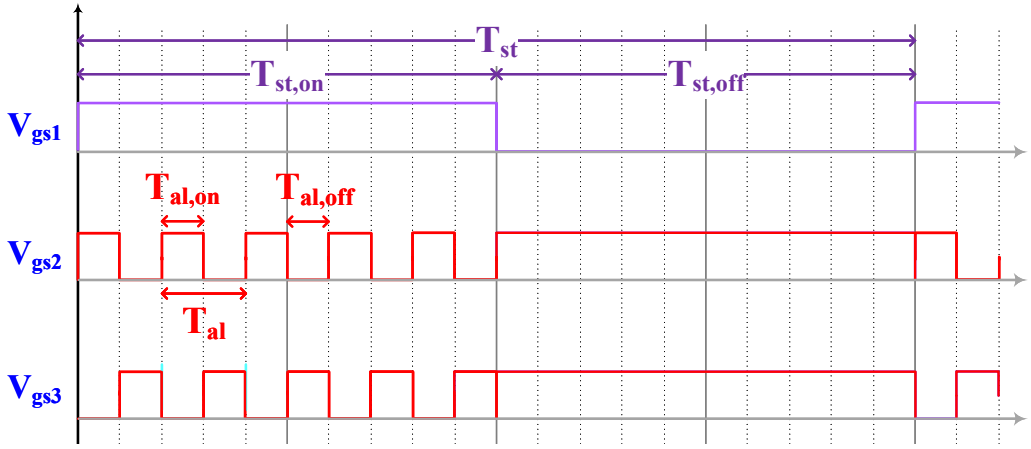

Figure 5.3: Gate-pulses for the 3S-DFRI

$$D_{st} = \frac{T_{st,on}}{T_{st}} \qquad f_{st} = \frac{1}{T_{st}} \tag{5.1}$$

$$D_{al} = \frac{T_{al,on}}{T_{al}} \qquad f_{al} = \frac{1}{T_{al}} \tag{5.2}$$

Where, D_{st} and f_{st} are duty cycle and operating frequency for the steel load respectively. D_{al} and f_{al} are duty cycle and operating frequency for the aluminum load respectively. $T_{st,on}$ and T_{st} are the ON time and total time period of the switch S_1. $T_{al,on}$ and T_{al} are the turn-on and total time period of the switch S_2 when S_1 is ON. S_3 operates in complementary to S_2 when S_1 is ON. Also, both S_2 and S_3 are ON continuously when S_1 is OFF as shown in the Figure 5.3.

5.3 Operating Modes

The complete operation of the 3S-DFRI is depicted in Figure 5.4 and is divided into following three modes.

5.3.1 Mode-1

In this mode, S_1 and S_2 are ON and S_3 is OFF as shown in Figure 5.4(a). Both the loads are powered by C_4. Steel load current is negative and it flows through body diode of S_1 during the transition from mode-3 to mode-1, where S_1 is turning ON which was in OFF state during mode-3. The voltage across S_1 is clamped. Hence, ZVS turn-ON of S_1 is obtained. The direction of the currents through both the IH loads is as depicted in Figure 5.4(a).

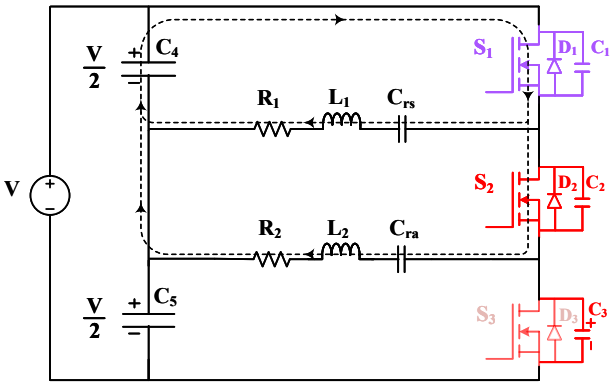

(a) Mode-1

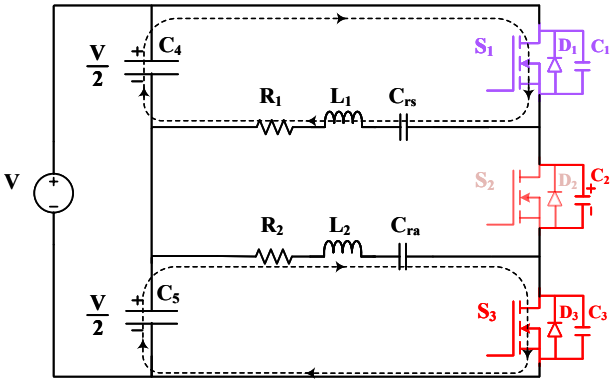

(b) Mode-2

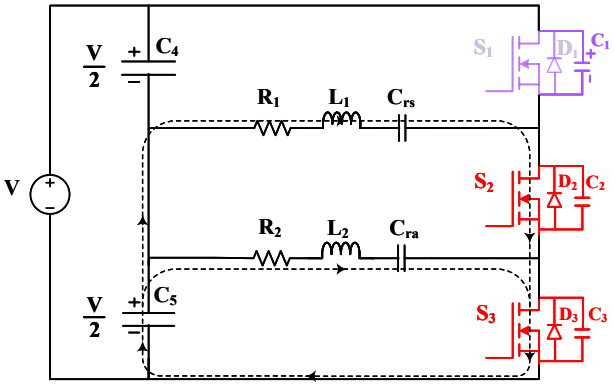

(c) Mode-3

Figure 5.4: Operating modes for 3S-DFRI

5.3.2 Mode-2

In this mode, S_2 is being turned-off and S_3 is turning ON. As load current is of lagging nature, negative current will flow though body diode of S_3 in the transition from mode-1 to mode-2. This ensures zero voltage turn-on of S_3. The load current directions are shown in Figure 5.4(b).

5.3.3 Mode-3

During this mode, S_2 is turning ON and S_1 is turning OFF. Steel load current shown in mode-2 will pass through the body diode of S_2 during the transition from mode-2 to mode-3 ensuring ZVS for turn-on of S_2. The state during this mode is depicted in Figure 5.4(c).

5.4 Output Power Control

The resonant frequency for the IH load is given by

$$f_r = \frac{1}{2\pi\sqrt{LC}} \tag{5.3}$$

Where, L is equivalent inductor of the IH load and C is resonant capacitor for the loads. Using above equation 5.3, respective resonant frequencies for steel (f_{rs}) and aluminum (f_{ra}) loads can be obtained for their respective parameters mentioned in Table 5.1. The switching frequencies are selected a bit higher than their respective resonant frequencies to ensure lagging of load current. It helps in ZVS operation. For steel load, Fourier series expression for output voltage $V_{o,st}$ can be expressed as

$$v_{o,st}(t) = \frac{V(2D_{st}-1)}{2} + \sum_{n=1}^{\infty} \frac{2V}{n\pi} \sin(n\pi D_{st}) \cos(n\omega t - n\pi D_{st}) \tag{5.4}$$

Using fundamental component, the rms voltage across steel load can be written as

$$V_{o,st,rms} = \frac{\sqrt{2}V}{\pi} \sin(\pi D_{st}) \tag{5.5}$$

$$I_{o,st,rms} = \frac{\sqrt{2}V \sin(\pi D_{st})}{\pi} \frac{\cos\psi}{R_1} \tag{5.6}$$

where,

$$\cos\psi = \frac{1}{\sqrt{1+Q_{L,st}^2(\frac{\omega}{\omega_o}-\frac{\omega_o}{\omega})^2}} \tag{5.7}$$

where $Q_{L,st}$ = quality factor for‘ the steel load, ω_o = resonant frequency. Now, the output power equation for steel load can be given by

$$P_{st} = I_{o,st,rms}^2 \times R_1 \tag{5.8}$$

$$= \frac{2V^2\sin^2(\pi D_{st})}{\pi^2 R_1} \times \frac{1}{1+Q_{L,st}^2(\frac{\omega}{\omega_o}-\frac{\omega_o}{\omega})^2} \tag{5.9}$$

It can be observed from above equations that P_{st} depends on D_{st}. By varying frequency f_{st}, the operating point on resonance curve changes so impedance of the circuit also changes. Hence, steel load current can also be varied by varying f_{st}.

For aluminum load, it is getting powered only when switch S_1 is ON i.e., $T_{st,on}$. As the switch S_1 is turning on and off, the current through the aluminum load, i_{al} is oscillatory as shown in Figure 5.5. The envelope of this load current ($i_{E,al}$) follows first order response with time constant $\tau = \frac{2L}{R}$.

By using the detailed procedure mentioned in [61], the average power in aluminum load can be given by

$$\begin{aligned} P_{al} &= \frac{2}{\pi}V\cos\alpha\frac{1}{T_{st}}\int_0^{T_{st,on}} i_{e,al}(t)dt \\ &= P_{al,m}\frac{T_{st,on}}{T_{st}} + \frac{\tau}{T_{st}}\left(\frac{1-e^{\frac{-T_{st,on}}{\tau}}}{1-e^{\frac{-T_{st}}{\tau}}}\right)\left(e^{\frac{-T_{st,on}}{\tau}} - e^{\frac{-T_{st}}{\tau}}\right) \end{aligned} \tag{5.10}$$

Where $P_{al,m} = (2/\pi)VI_{al,m}\cos\alpha$ is the maximum output power for aluminium for when $T_{st,on} = T_{st}$. And α is the angle between output voltage and load current. The maximum current

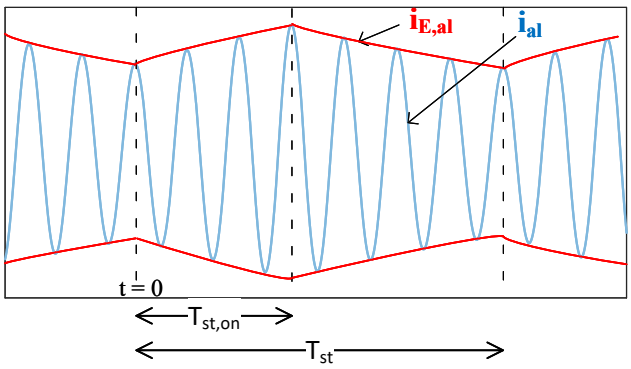

Figure 5.5: Aluminum load current and its envelope

Table 5.1: Parameters for proposed 3S-DSFRI.

Component	**Value**
DC supply voltages, $2 \times \frac{V}{2}$	$2 \times 82.5 = 165V$
steel load equivalent resistance, R_1	2.8 Ω
steel load equivalent inductance, L_1	66 μH
resonant capacitor for steel load, C_{rs}	0.52 μF
aluminum load equivalent resistance, R_2	2 Ω
aluminum load equivalent inductance, L_2	52.7 μH
resonant capacitor for aluminum load, C_{ra}	10.5 nF
steel load control frequency, f_{st}	29-44 kHz
aluminum load control frequency, f_{al}	215-228 kHz
MOSFETs used	IRFP4127PbF
r_{ds} of MOSFETs	17 $m\Omega$

can be derived using Fourier analysis and is given by

$$I_{al,m} = \frac{2V}{\pi|Z|}\sin(\pi D_{al}) \tag{5.11}$$

Where, 'Z' is the impedance of aluminum load. Now, for $T_{st} << \tau$, no oscillations in the output power will occur and the relation can be given by

$$\lim_{\tau\to\infty} P_{al} = P_{al,m}\left(\frac{T_{st,on}}{T_{st}}\right)^2 \tag{5.12}$$

And for $T_{st} >> \tau$, the load current will become discontinuous and its equation can be given by

$$\lim_{\tau\to 0} P_{al} = P_{al,m}\frac{T_{st,on}}{T_{st}} \tag{5.13}$$

It can be observed from above equations that power in aluminum load, P_{al} depends on D_{al}, τ and $T_{st,on}$. By varying the operating frequency f_{al}, the impedance of the circuit and hence the current flowing through aluminum load can be altered. Frequency based control is applied for both the loads. For aluminum load, duty cycle control is also applied. The power in the aluminum load is depending on the D_{st}. To increase maximum power for aluminum load, D_{st} can be increased above 50%. This will reduce the maximum power for steel load which can be compensated by reducing its operating frequency. Analysis of the inverter operation is done with $D_{st} = 50\%$ and $D_{st} = 65\%$ and is verified through simulation and experimentation.

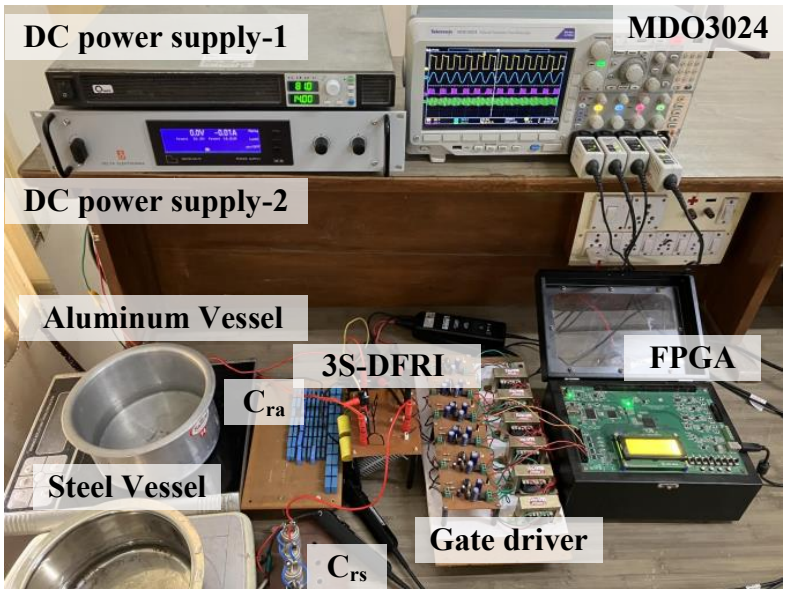

Figure 5.6: Hardware setup

5.5 Experimentation Results and Analysis

The experimental parameters for the 3S-DFRI are mentioned in the Table 5.1. Two DC power supplies are connected in series to obtain 165 V. Resonant capacitors are obtained by series-parallel combination of MKV-B25834 and MKP-B32672L type capacitors. The complete experimentation setup is shown in Figure 5.6. The control for the inverter is realised using an FPGA controller board. The values of D_{st} should be selected as per the maximum powering requirements of both the loads. The inverter prototype has been tested for D_{st} values of 65% and 50% .

The full load output power experimentation results are shown in Figure 5.7. For $D_{st} = D_{al} = 50\%$ (50-50), the results are shown in Figure 5.7(a). f_{st} and f_{al} are 30 kHz and 215 kHz respectively. The rms currents flowing through steel and aluminum loads are 19.95 A and 15.86 A respectively. Steel load is powered at 1114.41 W and aluminium load is powered at 503.08 W. The total power delivered is 1617.49 W. Figure 5.7(b) shows the experimental results when D_{st}=65% and D_{st}=50% (65-50). f_{st} and f_{al} are maintained at 29 kHz and 215 kHz respectively. The rms currents of 20.36 A and 19.54 A flows through steel and aluminum loads powering them at 1160.68 W and 763.62 W respectively. Total output load power for the inverter is 1924.3 W. The soft switching operation of the three switches during full load power modes is shown in Figure 5.8.

The output power variation results are shown in Figure 5.9. Figure 5.9(a) and Figure 5.9(b) depicts the results for frequency based control for both the loads. Figure 5.9(a)

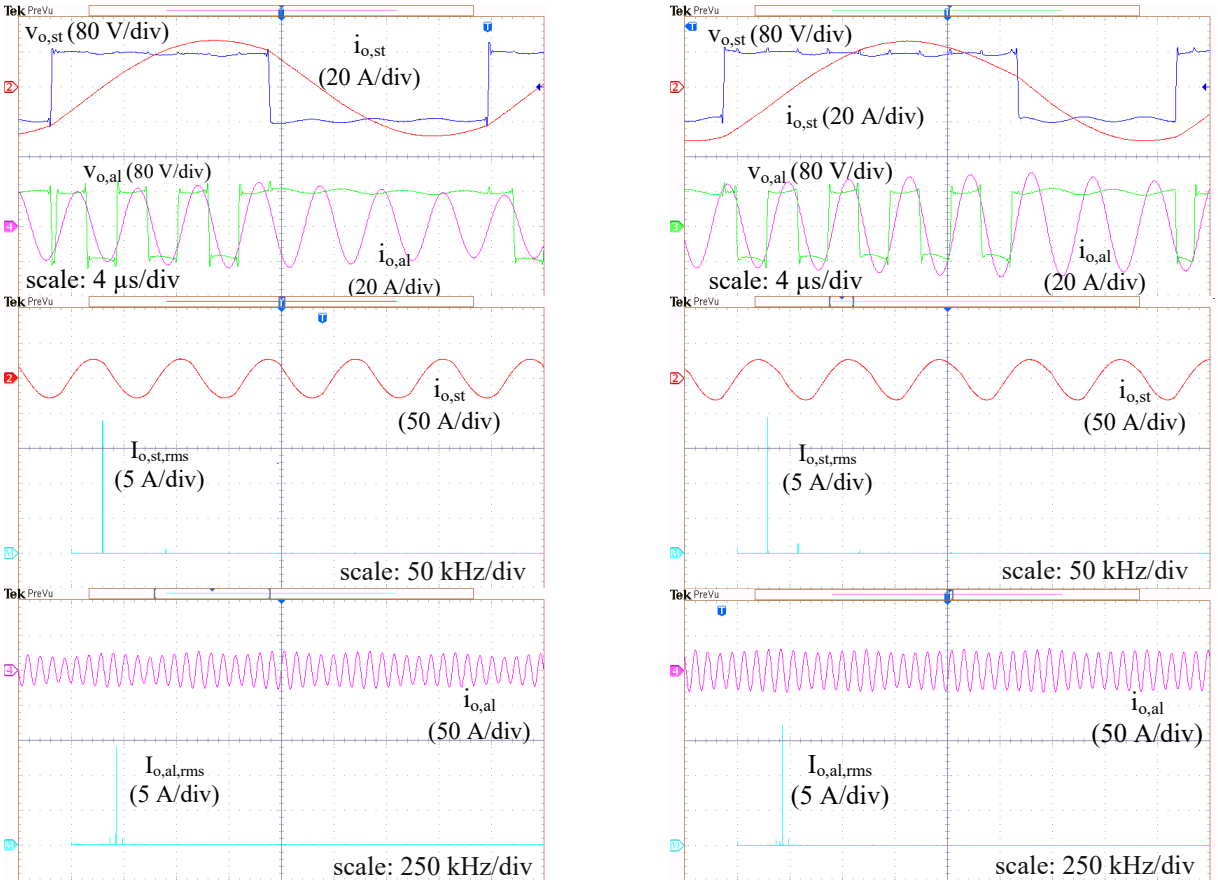

(a) $D_{st} = D_{al} = 50\%$ (b) $D_{st} = 65\%, D_{al} = 50\%$

Figure 5.7: Experimentation waveforms for full load power operation. From top to bottom: output voltage-current waveforms and load current FFTs for steel and aluminum loads

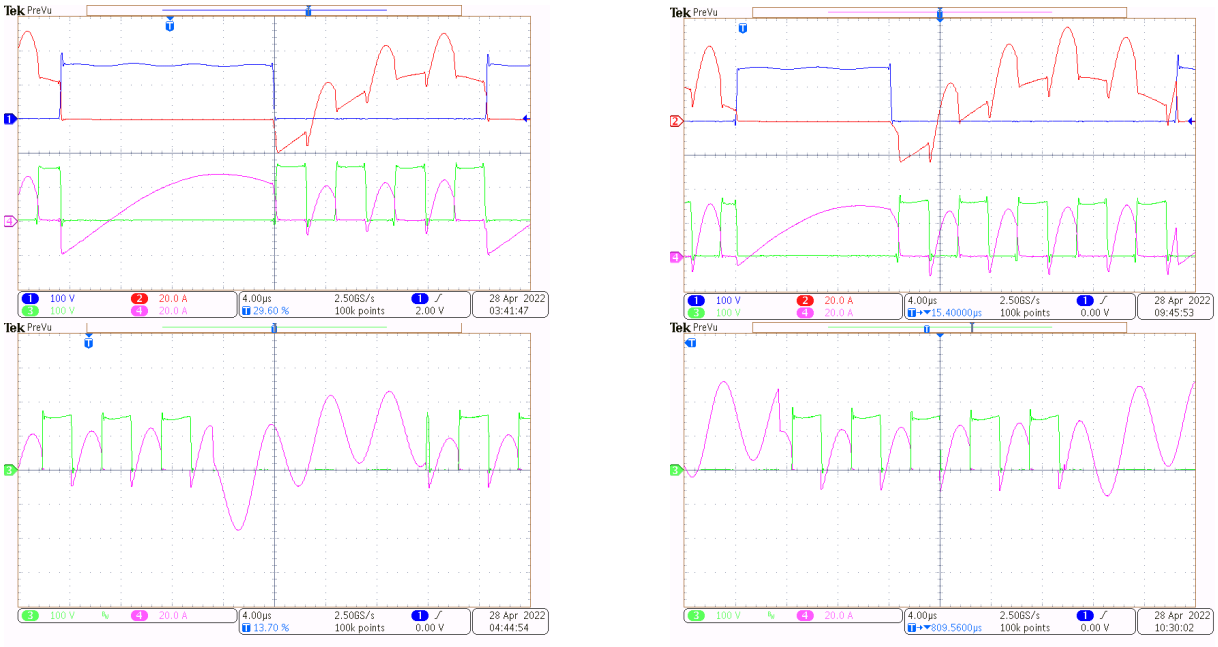

(a) $D_{st} = D_{al} = 50\%$ (b) $D_{st} = 65\%, D_{al} = 50\%$

Figure 5.8: Experimentation waveforms of switch voltage and currents for full load power operation. From top to bottom: S_1, S_2 and S_3 respectively. Scale: voltage (100 V/div) and current (20 A/div)

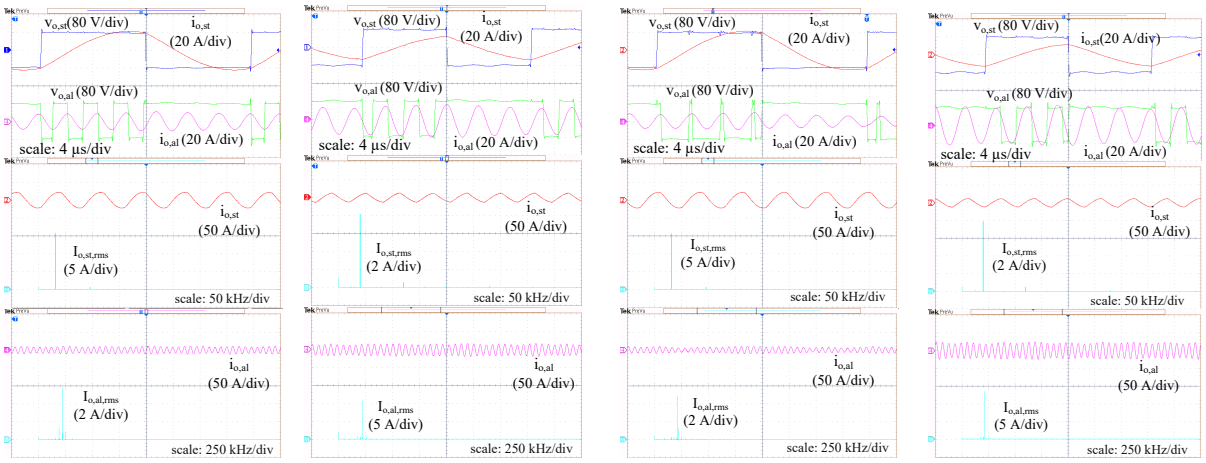

(a) f_{st}=32 kHz and f_{al}=220 kHz (b) f_{st}=40 kHz and f_{al}=216 kHz (c) f_{st}=32 kHz and D_{al}=85% (d) f_{st}=40 kHz and D_{al}=50%

Figure 5.9: Variable power operation of 3S-DFRI with frequency and duty cycle control for $D_{st} = 50\%$. From top to bottom: output voltage-current waveforms and load current FFTs for steel and aluminum loads. (a) and (b): $D_{al} = 50\%$. (c) and (d) f_{al} = 215 kHz.

shows the experimental results when steel and aluminum loads are powered at 677.1 W and 74.71 W carrying 15.6 A and 6.1 A respectively. Figure 5.9(b) shows the experimental results when steel and aluminum loads are powered at 190 W and 247.3 W carrying 8.24 A and 11.12

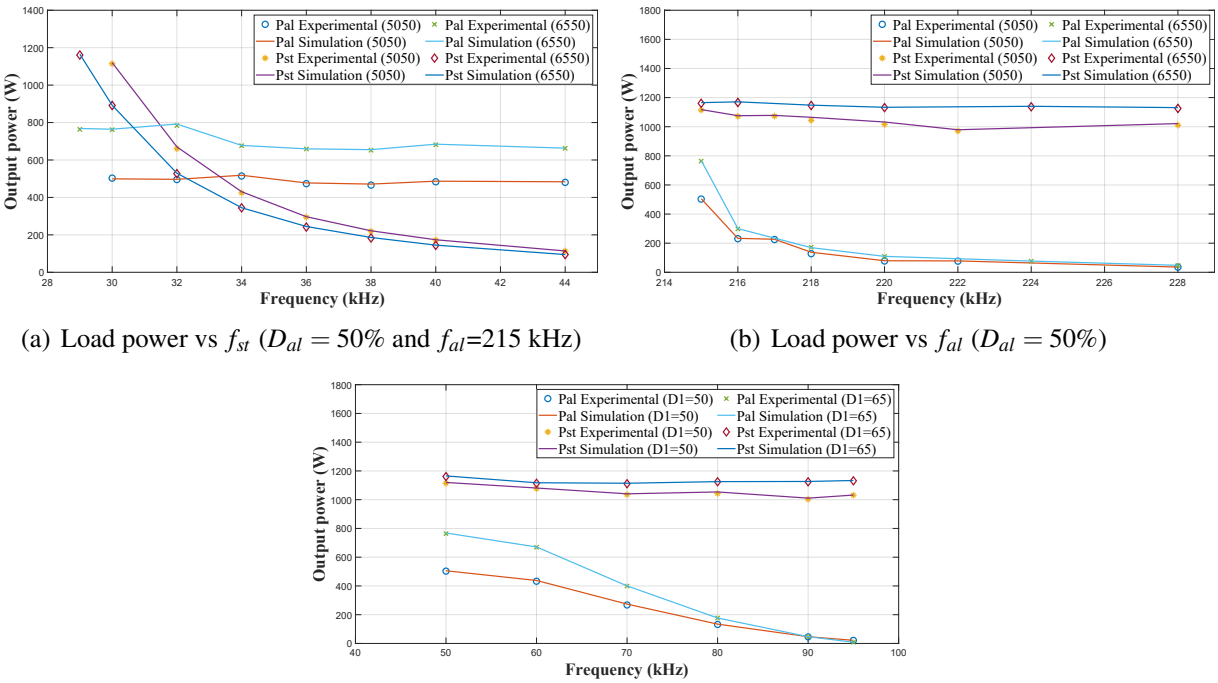

(a) Load power vs f_{st} ($D_{al} = 50\%$ and f_{al}=215 kHz)

(b) Load power vs f_{al} ($D_{al} = 50\%$)

(c) Load power vs D_{al} (f_{al}=215 kHz)

Figure 5.10: Output power variation over frequency and duty cycle control.

A respectively. Figure 5.9(c) and Figure 5.9(d) depicts the results for frequency based control for steel and duty cycle based control for aluminum load. Figure 5.9(c) shows the results when steel and aluminum loads currents are 15.5 A and 5.7 A with load powers of 673.57 W and 65.67 W respectively. Figure 5.9(d) shows the results when steel and aluminum load currents are 7.9 A and 15.86 A powering them at 176 W and 503.08 W respectively.

The graphs of output power variation with frequencies and duty cycles are plotted in Figure 5.10. Simulation and experimental results for variable power operation under $D_{st} = 50\%$ and $D_{st} = 65\%$ are plotted. And it is observed that simulation and experimental results are in good accord with each other. Figure 5.10(a) shows steel load power variation over frequency while aluminum load control parameters are maintained constant. The steel load power is controlled from 1114.41 W to 113.62 W and 1160.68 W to 94.68 W for $D_{st} = 50\%$ and $D_{st} = 65\%$ respectively. D_{al} is also maintained constant at 50% throughout the operation. Figure 5.10(b) shows aluminum load power variation over frequency while steel load control parameters are maintained constant. The aluminum load power is controlled from 503.08 W to 35.28 W and 763.62 W to 46.87 W for $D_{st} = 50\%$ and $D_{st} = 65\%$ respectively. D_{al} is maintained at 50% constant through the operation. Figure 5.10(c) shows the aluminum load power variation with duty cycle while steel load control parameters are maintained constant. With the duty cycle control, aluminium load power is varied from 503.08 W to 21.26 W and 763.62 W to 8 W for

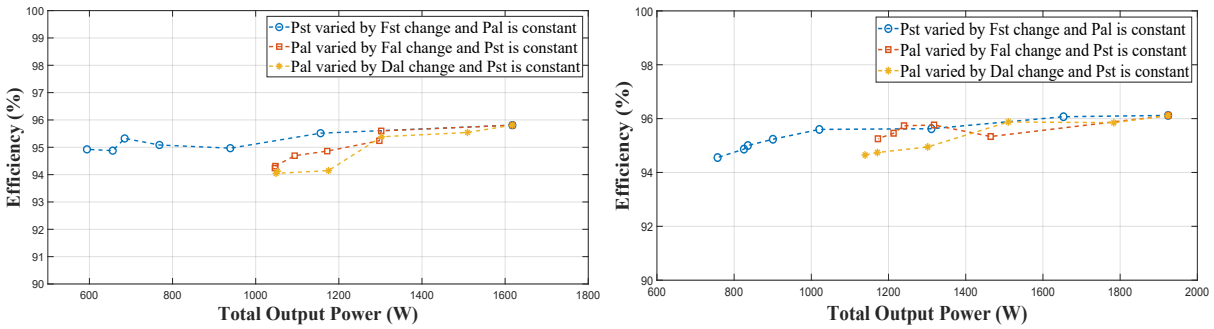

(a) $D_{st} = D_{al} = 50\%$ (b) $D_{st} = 65\%$

Figure 5.11: Efficiency over total output power variation

$D_{st} = 50\%$ and $D_{st} = 65\%$ respectively. Steel and aluminum load frequencies are maintained constant during the entire operation. The efficiency of the inverter over the total output power variation is plotted in Figure 5.11. It can be observed that the inverter operates with more than 94% efficiency for the entire power variation. The peak efficiency offered by the inverter is 96.11%. Thermal images for both the vessels operated at full load for a minute is shown in Figure 5.12. The proposed inverter topology is compared with the other existing inverter topologies which are suitable for two different material IH loads and is presented in Table 5.2. It is observed that the proposed inverter topology offers the advantages of soft-switching operation, high efficiency, independent as well as simultaneous control and low component count without any electro-mechanical switches.

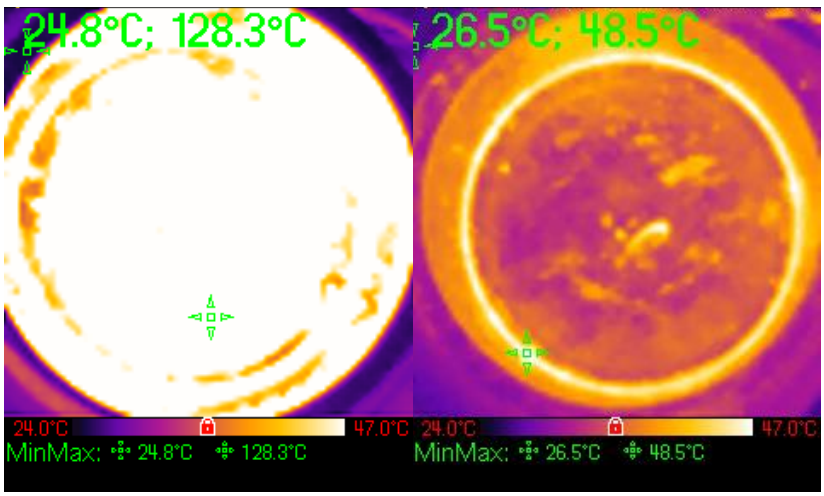

Figure 5.12: Thermal images for steel and aluminum loads

Table 5.2: Comparison of IH solutions for different material vessels for two loads

Ref.	Operating frequency (kHz)	Soft switching	Peak efficiency (%)	Independent control	Simultaneous control	No. of switches & diodes	Electro-mechanical switches	No. of L & C
[33]	20, 50	No	-	Yes	No	2	1	2 coils, 1 C
[37]	23-75	No	96	Yes	No	2	1	1 C
[38]	30,150	Yes	92	Yes	Yes	4	0	1 C
[39]	25-125	Yes	96.5	Yes	No	4	2	1 C
[41]	20,100,400	No	$\geq$92	Yes	Yes	8	0	2 C
[42]	30/78	Yes	94.32	Yes	No	4	1	1 L & 2 C
Proposed 3S-DFRI	29-44, 215-228	Yes	96.11	Yes	Yes	3	0	2 C

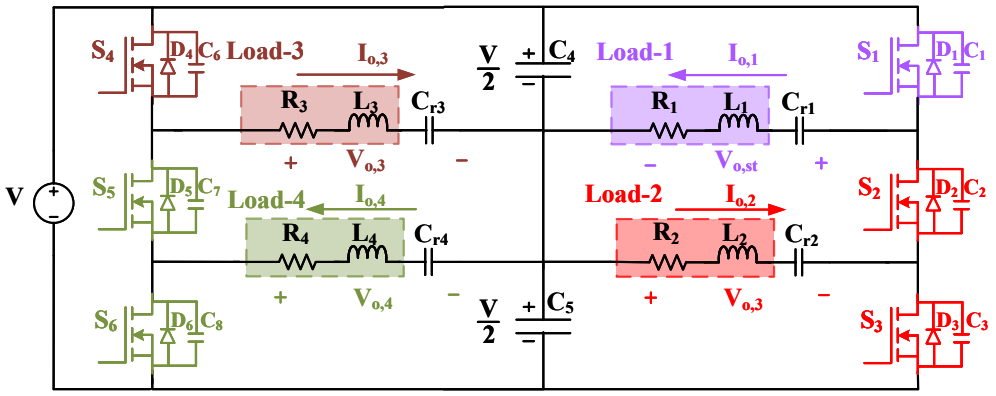

Figure 5.13: Extension of the topology with four different IH loads

5.6 Extension of the Inverter

The proposed inverter can be extended for multiple different material IH loads. Figure 5.13 shows the extension of the proposed 3S-DFRI for four loads. All these four loads can be powered at four different frequencies. Hence, different frequency requirement of the loads can be met and also load powers can be independently controlled. This topology can be extended for multiple IH loads by addition of three switches per two loads. The extension gives provision of four independent frequency component generation as output.

5.7 Conclusion

In this chapter, the proposed 3S-DFRI topology suitable for two different material IH loads has been explained in detail. The operation of the proposed inverter and independent power control have been verified with rigorous simulation and experimentation. Experimental prototype of the inverter has been implemented and tested for 1.92 kW total output power rating. Steel and aluminum vessel loads have been used for experimentation. It provides peak efficiency of 96.11%. Frequency and duty cycle based controls have been used for simultaneous as well as independent power control. The proposed solution can be extended for multiple IH loads with three switches per two different IH loads. Low component count, high efficiency, simultaneous and independent control are main advantages of the proposed solution for heating vessels of different materials.

Chapter 6

Dual Half-bridge Resonant Inverter for Different Material Induction Cooking Application

Chapter 6

Dual Half-bridge Resonant Inverter for Different Material Induction Cooking Application

6.1 Introduction

This chapter proposes a dual half-bridge three switch resonant inverter (DHB-3SRI). It eliminates the lossy split capacitor arrangement present in the proposed inverters of Chapter 3 and Chapter 5. It can simultaneously power different material vessel loads with independent power control. Its performance has been thoroughly analyzed with rigorous simulations and experimentation for total output power rating of 1.95 kW. Reduced component count, high efficiency, compactness and cost effectiveness are the key advantages of the proposed dual half-bridge three switch resonant inverter. The detailed explanation of the proposed DHB-3SRI is presented in further sections of this chapter. Section 6.2 describes the inverter and its control. The operating modes of the inverter are explained in Section 6.3. The complete analysis of the inverter with relevant mathematical expressions is described in Section 6.4. The experimental results and analysis are presented in Section 6.5. Section 6.6 explains the possibility of extension of the proposed inverter for multiple loads. Finally, major conclusions of this research work are presented in Section 6.7.

6.2 Proposed DHB-3SRI and its Control

The proposed inverter circuit is shown in Figure 6.1. It consists of a dc source, three switches and ferro and non-ferromagnetic material vessel IH loads with their respective series resonant capacitors. FM load is modelled as '$R_f - L_f$' (Load-f) and it is resonated with capacitor C_{rf}. N-FM load is modelled as '$R_n - L_n$' (Load-n) and its resonant capacitor as C_{rn}.

The control logic for DHB-3SRI is presented in Figure 6.2. It offers two half-bridge operation using only three switches. Gate pulses generated for the inverter are as shown in Figure. 6.3. It can be observed that when S_a is ON, high frequency pulses are generated by switching S_b and S_c for Load-n. Hence, S_b and S_c form a high frequency HB circuit. When S_a is OFF, both S_b and S_c turns ON which ensures powering Load-f at low frequency. Now, S_a and

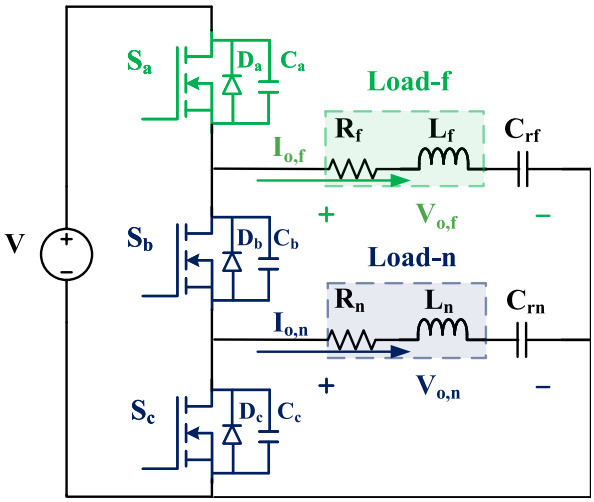

Figure 6.1: Proposed dual half-bridge three switch resonant inverter

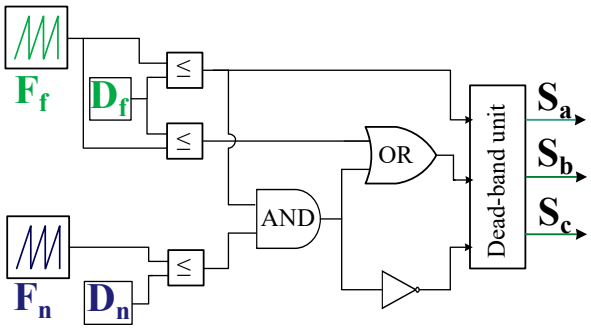

Figure 6.2: Two frequency control logic

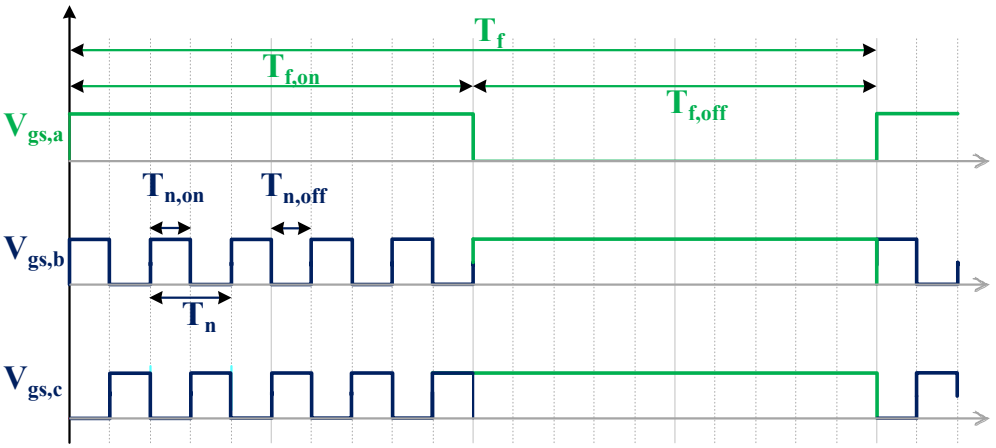

Figure 6.3: Gate-pulses for the DHB-3SRI

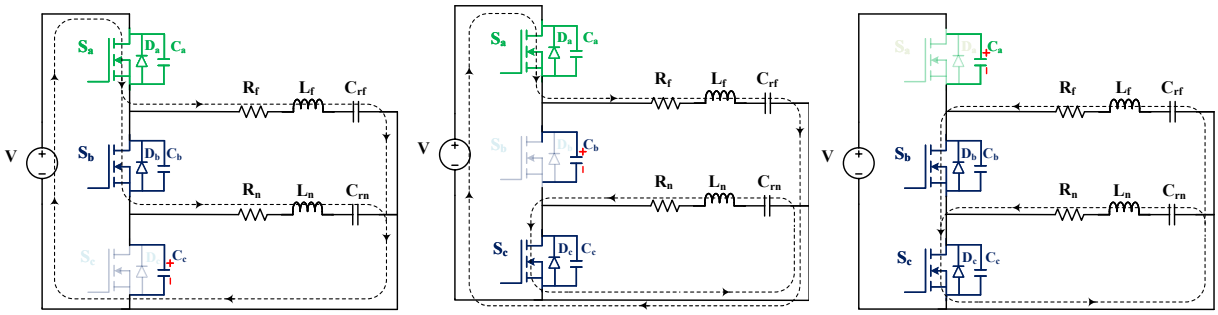

(a) Mode-1 (b) Mode-2 (c) Mode-3

Figure 6.4: Operating modes for DHB-3SRI

S_b & S_c form the low frequency HB. The duty cycle and frequencies for FM and N-FM loads can be given as follows.

$$D_f = \frac{T_{f,on}}{T_f} \qquad f_f = \frac{1}{T_f} \tag{6.1}$$

$$D_n = \frac{T_{n,on}}{T_n} \qquad f_n = \frac{1}{T_n} \tag{6.2}$$

Where, D_f and D_n are duty cycles for FM and N-FM loads respectively. f_f and f_n are switching frequencies for FM and N-FM loads respectively. $T_{f,on}$ and T_f are respectively the ON time and total time period of S_a. $T_{n,on}$ and T_n are respectively the ON time and total time period of the switch S_b when S_a is ON as depicted in the Figure 6.3.

6.3 Operating Modes

The operation of DHB-3SRI is divided into three modes as presented in Figure 6.4.

6.3.1 Mode-1

In this mode, both the loads are powered as S_a, S_b are ON while S_c is OFF as shown in Figure 6.4(a). S_a is being turned ON from its previous OFF condition. During this turn-ON transition, diode D_a across S_a will conduct and FM load current flows through it. It clamps the voltage across S_a during its turn-ON. So, ZVS turn-ON of S_a is ensured. The direction of the currents through both the loads is as depicted in Figure 6.4(a).

Table 6.1: DHB-3SRI circuit parameters.

Component	**Value**
DC supply voltages, $2 \times \frac{V}{2}$	$2 \times 82.5 = 165V$
Load-f equivalent resistance, R_f	2.8 Ω
Load-f equivalent inductance, L_f	66 μH
Load-f resonant capacitor, C_{rf}	0.52 μF
Load-n equivalent resistance, R_n	2 Ω
Load-n equivalent inductance, L_n	53.4 μH
Load-n resonant capacitor, C_{rn}	10.5 nF
Load-f control frequency, f_f	29-44 kHz
Load-n control frequency, f_n	215-228 kHz
switching devices, MOSFETs	IRFP4127PbF
r_{ds} of MOSFET	17 $m\Omega$

6.3.2 Mode-2

In this mode, N-FM load current is freewheeled while FM load continue to be powered. S_b is turning off and S_c is turning ON. As load current is of lagging nature, N-FM load current will flow though body diode of S_c during the transition from Mode-1 to Mode-2. This ensures ZVS during turn-on of S_c. The load current directions are shown in Figure 6.4(b).

6.3.3 Mode-3

During this mode, both the loads are freewheeling as S_b and S_c are ON. S_b is turning ON and S_a is turning OFF. FM load current shown in Mode-2 will pass through the body diode of S_b during the transition from Mode-2 to Mode-3 ensuring zero voltage turn ON of S_b. This state is depicted in Figure 6.4(c).

6.4 Output Power Control

For IH load, the resonant frequency is calculated as

$$f_r = \frac{1}{2\pi\sqrt{LC}} \tag{6.3}$$

where, L and C are equivalent inductor and resonant capacitor of the load respectively. Using equation 6.3, respective resonant frequencies of FM (f_{rf}) and N-FM (f_{rn}) loads can be obtained

for their respective parameters indicated in Table 6.1. FM load is resonated at a low frequency of 29 kHz and N-FM load is resonated at a high frequency of 215 kHz. This ensures the independent operation for FM and N-FM load. The switching frequencies are chosen a bit higher than that of their respective resonant frequencies to ensure lagging nature of IH load currents. It facilitates in ZVS operation. For FM load, Fourier series expression for output voltage $v_{o,f}$ is given as

$$v_{o,f}(t) = \frac{V(2D_f - 1)}{2} + \sum_{n=1}^{\infty} \frac{2V}{n\pi} \sin(n\pi D_f) \cos(n\omega t - n\pi D_f) \tag{6.4}$$

Considering only fundamental component, the rms voltage and current of FM load can be given as

$$V_{o,f,rms} = \frac{\sqrt{2}V}{\pi} \sin(\pi D_f) \tag{6.5}$$

$$I_{o,f,rms} = \frac{\sqrt{2}V \sin(\pi D_f)}{\pi} \frac{\cos\psi}{R_1} \tag{6.6}$$

where,

$$\cos\psi = \frac{1}{\sqrt{1 + Q_{L,f}^2 (\frac{\omega}{\omega_o} - \frac{\omega_o}{\omega})^2}} \tag{6.7}$$

where $Q_{L,f}$ = quality factor of the FM load, ω_o = resonant frequency. Now, the output power for FM load can be expressed as

$$P_f = I_{o,f,rms}^2 \times R_1 \tag{6.8}$$

$$= \frac{2V^2 \sin^2(\pi D_f)}{\pi^2 R_1} \times \frac{1}{1 + Q_{L,f}^2 (\frac{\omega}{\omega_o} - \frac{\omega_o}{\omega})^2} \tag{6.9}$$

It can be noted from above equations that P_f depends on D_f. By varying f_f, the operating point and load impedance changes. Hence, FM load power can also be varied by changing f_f.

Now, N-FM load is powered only during $T_{f,on}$ (when S_a is ON). The turn-on and turn-off of S_a make the N-FM load current i_n, oscillatory as depicted in Figure 6.5. This load current envelope ($i_{E,n}$) gives the response of first order with time constant $\tau = 2L/R$. By using the

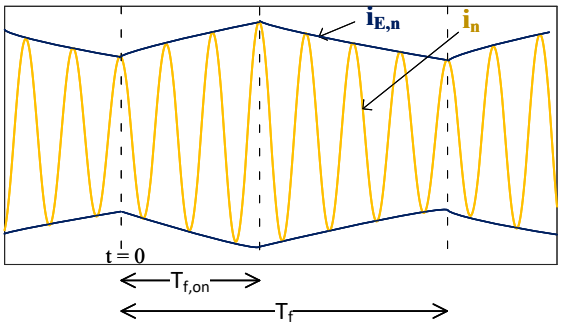

Figure 6.5: N-FM load current envelope

procedure described in [59], the average power delivered to N-FM load can be expressed by

$$\begin{aligned} P_n &= \frac{2}{\pi} V \cos\alpha \frac{1}{T_f} \int_0^{T_{f,on}} i_{e,n}(t)dt \\ &= P_{n,m}\frac{T_{f,on}}{T_f} + \frac{\tau}{T_f}\left(\frac{1-e^{\frac{-T_{f,on}}{\tau}}}{1-e^{\frac{-T_f}{\tau}}}\right)\left(e^{\frac{-T_{f,on}}{\tau}} - e^{\frac{-T_f}{\tau}}\right) \end{aligned} \tag{6.10}$$

Where $P_{n,m} = (2/\pi)VI_{n,m}\cos\alpha$ is the maximum value of output power for N-FM load when $T_{f,on} = T_f$. And α is the angle between load voltage and current. The expression for maximum current can be obtained using Fourier series as below:

$$I_{n,m} = \frac{2V}{\pi|Z|}\sin(\pi D_n) \tag{6.11}$$

where, 'Z' is the impedance of N-FM load. From the above equations, it can be inferred that the power in N-FM load, P_n is related to D_n, τ and $T_{f,on}$. Also, the power in N-FM load can be altered by changing the operating frequency, f_n as the load impedance changes with frequency. Duty cycle control of FM load is changing the output power of N-FM load also. Hence, frequency control is used for FM load power control. N-FM load can be independently controlled using duty cycle and frequency based control. The thorough analysis of the proposed DHB-3SRI with aforementioned controls is done for $D_f = 50\%$ and 65% with simulation and experimentation.

6.5 Results and Analysis

The parameters for the proposed DHB-3SRI are given in Table 6.1. Series connection of two DC sources is used to get 165 V. MKV-B25834 and box type MKP-B32672L capacitors are used to obtain different resonant capacitor requirements. FM load is realised by steel vessel and an IH coil arrangement. N-FM load is realised by aluminum vessel and an IH coil combination.

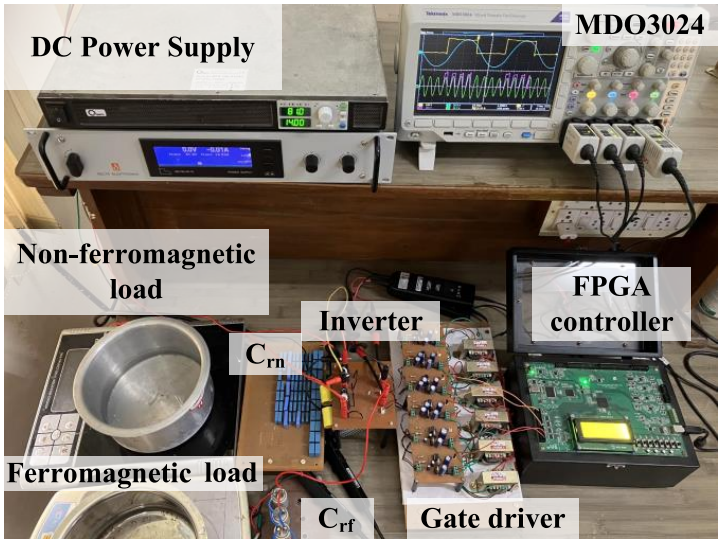

Figure 6.6: Hardware setup

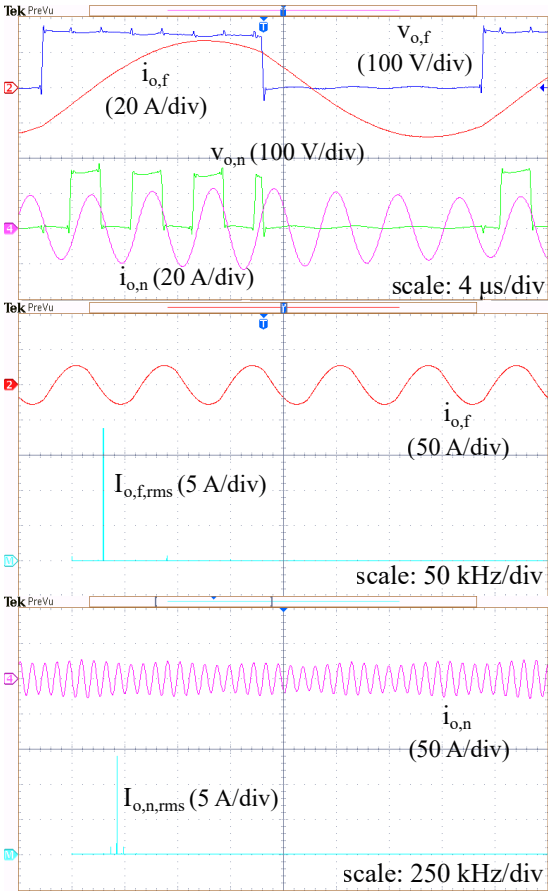

(a) $D_f = D_n = 50\%$

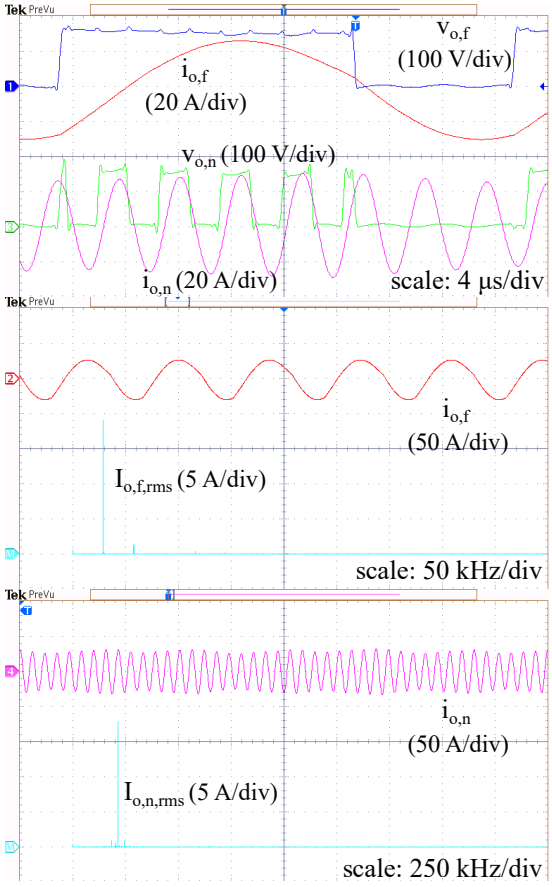

(b) $D_f = 65\%, D_n = 50\%$

Figure 6.7: Experimentation waveforms for full load power operation. From top to bottom: load voltage-current waveforms and load current FFTs for FM and N-FM loads

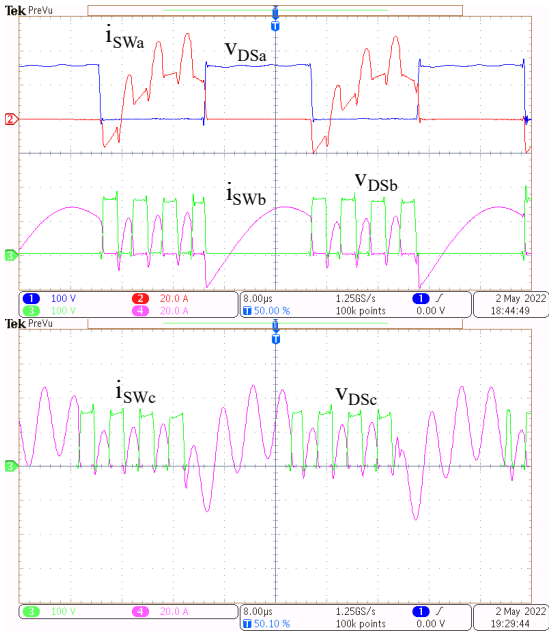

Figure 6.8: Switching devices voltage and current waveforms showing ZVS for D_f=D_n=50%. From top to bottom: S_a, S_b and S_c

Experimental setup for the proposed DHB-3SRI is shown in Figure 6.6. Spartan-6 FPGA controller is used for controlling the designed prototype. The DHB-3SRI prototype has been tested for D_f values of 65% and 50% to vary the maximum power output of FM and N-FM loads. Based on the maximum power requirements of FM and N-FM loads, the value of D_f is to be selected.

Figure 6.7 shows the full-load operation of the inverter. Figure 6.7(a) depicts the results for $D_f = D_n = 50\%$. f_f and f_n are 30 kHz and 215 kHz respectively. The rms currents flowing through FM and N-FM loads are 19.88 A and 16 A respectively. FM load is powered at 1106.6 W and N-FM load is powered at 512 W. The total output power delivered is 1618.6 W. The experimental results when D_f=65% and D_n=50% is presented in Figure 6.7(b). f_f and f_n are maintained at 29 kHz and 215 kHz respectively. The rms currents of 20.05 A and 20.25 A flow through FM and N-FM loads powering them at 1125.61 W and 820.13 W respectively. Total output load power for the inverter is 1945.74 W. Voltage and current waveforms of the switching devices S_a,S_b, and S_c are shown in Figure 6.8. ZVS operation of the devices is observed from this figure.

The results related to output power variation are shown in Figure 6.9. Figure 6.9(a) and Figure 6.9(b) depict the results for frequency based control of both the loads. Figure 6.9(a) shows the experimental results when FM and N-FM loads are powered at 670.96 W and 75.15 W carrying 15.48 A and 6.13 A respectively. Figure 6.9(b) shows the experimental results when FM and N-FM loads are powered at 172.54 W and 245.09 W carrying 7.85 A and 11.07

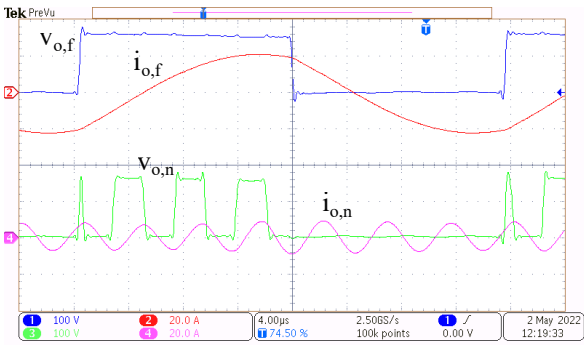

(a) f_f=32 kHz and f_n=220 kHz

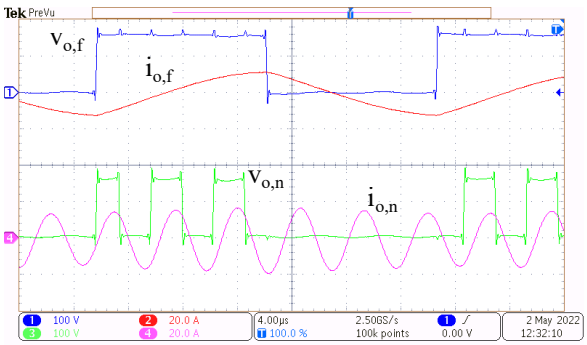

(b) f_f=40 kHz and f_n=216 kHz

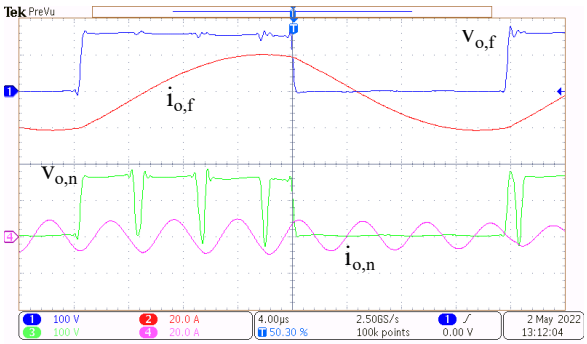

(c) f_f=32 kHz and $D_n = 85\%$

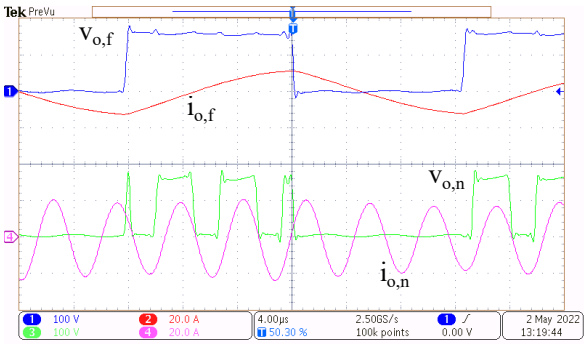

(d) f_f=40 kHz and $D_n = 60\%$

Figure 6.9: Variable power operation of DHB-3SRI with frequency and duty cycle control for D_f=50%. From top to bottom: output voltage-current waveforms for FM and N-FM loads. Scale:load voltage (100 V/div) and current (20 A/div)

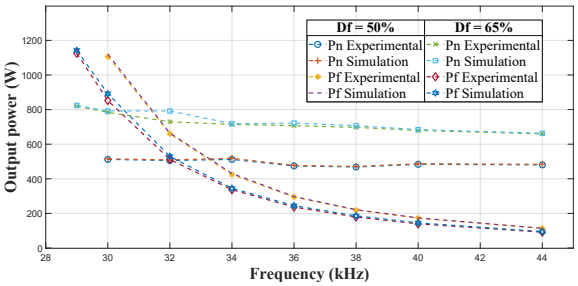

(a) FM load power variation with frequency when N-FM load is operated with fixed duty (D_n) and frequency (f_n)

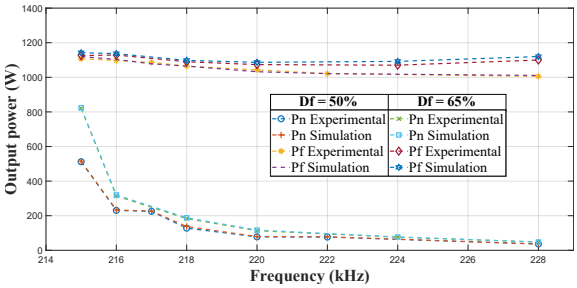

(b) N-FM load power variation with frequency when FM load is operated with fixed duty (D_f) and frequency (f_f)

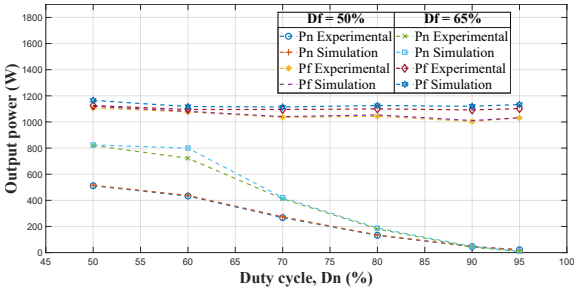

(c) N-FM load power variation with duty cycle when FM load is operated with fixed duty (D_f) and frequency (f_f)

Figure 6.10: Output power change over frequency and duty cycle control

A respectively. Figure 6.9(c) and Figure 6.9(d) show the experimental results for power control by frequency variation for FM load and duty cycle control for N-FM load. Figure 6.9(c) show the results when FM and N-FM loads currents are 14.95 A and 5.65 A powering them at 625.81 W and 63.85 W respectively. Figure 6.9(d) shows the results when FM and N-FM load currents are 7.65 A and 14.76 A powering them at 163.86 W and 435.72 W respectively.

The graphs of the load power variation with frequencies and duty cycles are plotted in Figure 6.10. Simulation and experimentation data for variable load power operation under $D_f = 50\%$ and $D_f = 65\%$ is plotted. Figure 6.10(a) shows FM load power variation with frequency while N-FM load control parameters are kept constant. The FM load power is controlled from 1106.6 W to 113.62 W at $D_f = 50\%$ and from 1125.61 W to 91.55 W at $D_f = 65\%$. D_n is maintained at 50%. Figure 6.10(b) shows N-FM load power variation over frequency while FM load control parameters are kept constant. The N-FM load power is controlled from 512 W to 36.46 W when $D_f = 50\%$ and from 820.13 W to 47.63 W when $D_f = 65\%$. D_n is maintained at 50%. Figure 6.10(c) shows the N-FM load power variation with duty cycle while FM load control parameters are kept constant. Using duty cycle based control, N-FM load power is varied from 512 W to 21.26 W when $D_f = 50\%$ and from 820.13 W to 9.25 W when

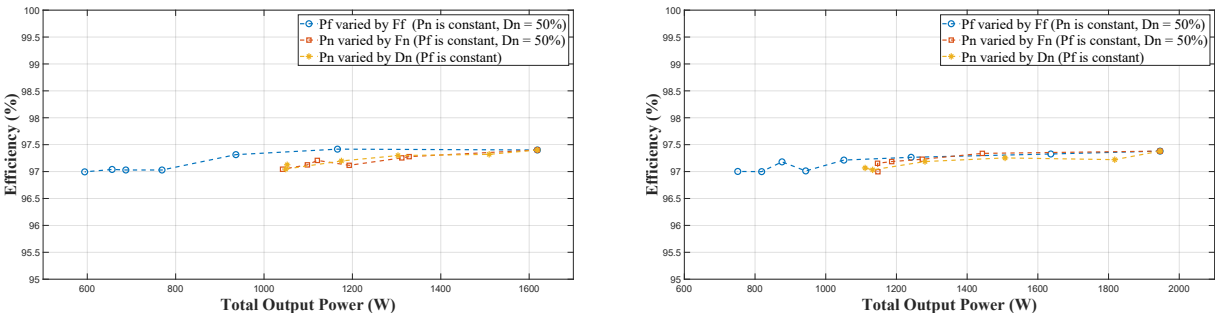

(a) $D_f = 50\%$ (b) $D_f = 65\%$

Figure 6.11: Efficiency vs total output power change

$D_f = 65\%$. FM and N-FM load frequencies are maintained constant throughout the operation. It can be observed from Figure 6.10(a) that while controlling FM load with frequency, the power in N-FM load is slightly reduced with increase in frequency. However frequency based control gives a wider range of power variation for FM load. FM load power remains unaffected when N-FM load is controlled with frequency or duty cycle as depicted in Figure 6.10(b) and Figure 6.10(c) respectively. It is observed that in N-FM load, duty cycle based control offers a wider and smooth power variation than that of frequency control. From above discussions, it can be concluded that the proposed inverter can heat FM load at high power but N-FM load with a limited power operation.

The inverter efficiency with total output power variation is presented in Figure 6.11. For the entire power range, the inverter operates at an efficiency of more than 96.75%. The peak efficiency of the inverter is 97.38%. The performance of the proposed inverter is compared with the inverter configurations available in the literature for powering FM and N-FM loads. Table 6.2 shows the comparison for some of the key features. It can be seen that in some of the configurations, electromechanical switches are used with capacitor switching which is not preferable. In some configurations, the number of components is more. And many of them do not have simultaneous and independent control. When compared to the classical two HB inverter, the voltage stresses for the proposed inverter remains same. However, the current stresses of the switches are increased as two IH load currents are flowing through three switches. The increased current stresses may lead to increased conduction losses. But as the drain-source resistance of the MOSFETs used for induction heating is very low, this increase in conduction losses will not have much significant effect on the overall efficiency. Also, the proposed converter offers many advantages over the conventional two half-bridge inverter. The proposed inverter uses a single capacitor whereas the classical two half-bridge approach uses a split capacitor arrangement. The parasitic resistance of these capacitors may be high. As the current

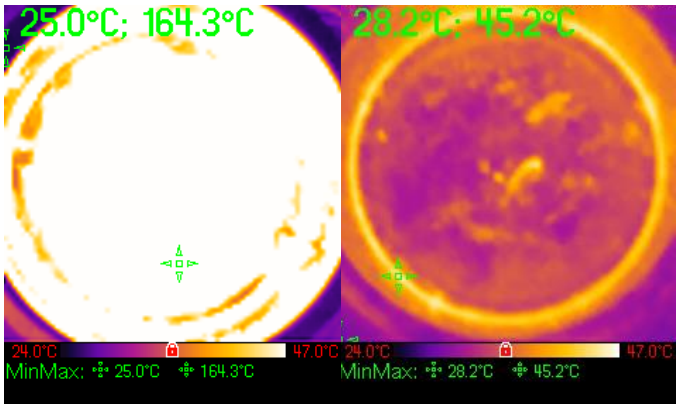

Figure 6.12: Thermal images for FM and N-FM loads during full-load operation

requirement for multi-load IH application is high, it will lead to increase in capacitor losses. This will affect the over all system efficiency. Also, the proposed converter uses three switches whereas two half-bridge inverter uses four switching devices. Hence, the number of switches and the gate drivers is more in two half-bridge inverter when compared to the proposed solution. This increased component count will affect the cost and size of the system. The proposed DHB-3SRI provides following key advantages:

(i) reduced component count

(ii) high efficiency

(iii) simultaneous and independent control

(iv) easy extension for multiple different material loads by adding three switches per two loads

Thermal images of steel and aluminum vessels when they are powered at full load for two minutes is given in Figure 6.12.

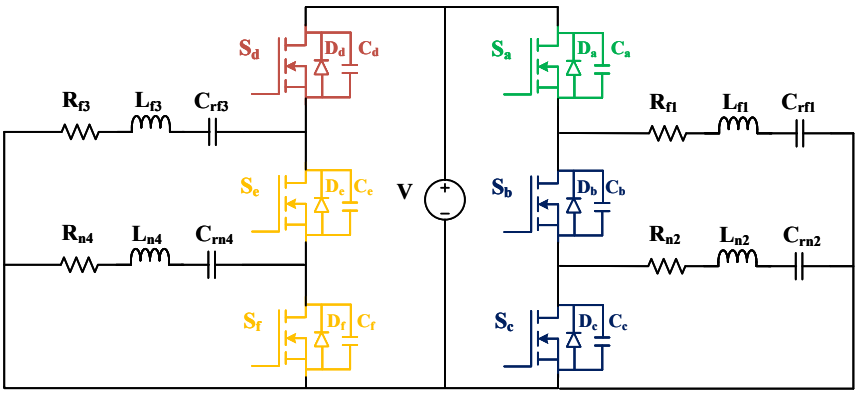

Figure 6.13: Extension of the topology for four different material loads

Table 6.2: Comparison of inverter topologies for two different material IH loads

Ref.	Operating frequency (kHz)	Soft switching	Peak efficiency (%)	Simultaneous control	Independent control	No. of switches & diodes	Electro-mechanical switches	No. of L & C
[33]	20, 50	No	-	No	Yes	2	1	2 coils, 1 C
[37]	23-75	No	96	No	Yes	2	1	1 C
[38]	30,150	Yes	92	Yes	Yes	4	0	1 C
[39]	25-125	Yes	96.5	No	Yes	4	2	1 C
[41]	20,100,400	No	$\geq$92	Yes	Yes	8	0	2 C
[42]	30/78	Yes	94.32	No	Yes	4	1	1 L & 1 C
Proposed	29-44, 215-228	Yes	97.38	Yes	Yes	3	0	1 C

6.6 Extension of the Inverter

The proposed DHB-3SRI can be extended for multiple loads as shown in Figure 6.13. It shows the extension of the inverter for four loads. All these four loads can be powered independently and controlled at four different frequencies. This topology can be easily extended for multiple different material IH loads by adding only three switching devices per additional two loads of different materials.

6.7 Conclusion

In this chapter, the proposed DF-3SRI has been described in detail. It operates as the combination of two half bridges operated at two different frequencies. Output voltage with two frequency components has been produced which can heat FM and N-FM material vessels at the same time. The detailed mathematical analysis of the inverter has also been presented. Further, the performance of the inverter has been verified by simulations and experimentation. For experimentation, a 1.95 kW hardware prototype has been built and tested. The simulation and experimentation results are in good agreement with each other. Output power characteristics with change in controlling parameters of frequency and duty cycles have been plotted. The proposed inverter is suitable for high power range operation of FM load and low to medium power range operation for N-FM load. The efficiency of the inverter has been measured and plotted for the entire control range. The proposed inverter operates with the peak efficiency of 97.38%. Reduced component count, removal of lossy split capacitors, high efficiency and compactness make the proposed inverter more promising for multiple load different material induction cooking application.

Chapter 7

Conclusions

Chapter 7

Conclusions

7.1 General Summary

Induction heating applications are gaining popularity these days. In this thesis, multiple load induction heating and different material induction heating applications are studied in detail. Four different inverter configurations for IC application are proposed. In this chapter, the detailed analysis of design, implementation and comparison of the proposed IH inverter topologies is performed.

7.1.1 Summary of important findings

The following conclusions have been arrived from the research work.

7.1.1.1 Proposed Three Switch Resonant Inverter (3SI) Configuration

A 3SI has been proposed for multiple load IH application. It uses three switches and a split capacitor arrangement to power two FM based vessels. The operating frequency of the 3SI is 28 kHz. Asymmetrical duty cycle control is used to obtain independent power control in each load. The proposed topology has been thoroughly analyzed, designed, simulated and hardware prototype has been implemented. Simulation and experimental results are in good agreement with each other. Following are the key advantages of the proposed 3SI:

- Lowest switch to load ratio for multiple ferromagnetic IH load control
- Simultaneous and independent control of IH loads with ADC control technique
- Compact solution for multiple load IH applications
- Soft-switching operation during both turn-ON and turn-OFF
- High efficiency (96.3%)

Hence, the proposed 3SI is suitable for multiple load IH application. It can also be extended for more loads by adding three switches per two loads.

7.1.1.2 Proposed Full Bridge based Multi-load Inverter (FB-MI) Configuration

A FB-MI configuration has been proposed for heating vessels of different materials. It uses a full bridge circuit along with switch-diode modules to power and control multiple different material IH loads. The operating frequency of the inverter is 30 kHz and 220 kHz. It uses an ON-OFF control technique for independent power control in each IH load. The proposed inverter has been designed, simulated and experimentally verified on a hardware prototype of 1.6 kW. The simulation and experimental results are in agreement with each other. The major advantages of the proposed inverter are as follows:

- Simple control
- Simultaneous and independent control of different material IH loads
- Easy extension for multiple IH loads application
- Soft-switching during turn-ON of switching devices
- High efficiency (94.3%)

Hence, the proposed FB-MI configuration is suitable for multiple load different material IH application. It can also be extended for more loads by adding a switch-diode module per each additional IH load.

7.1.1.3 Proposed Three Switch Dual Frequency Resonant Inverter (3S-DFRI) Configuration

A 3S-DFRI configuration for heating two different material vessel loads has been proposed. It uses three switches and a split capacitor arrangement to generate two different frequency components. The operating frequency for the inverter is 29 kHz-44 kHz and 215 kHz-228 kHz. Independent power control is realised by frequency and duty cycle based controls. The proposed dual frequency resonant inverter has been designed, simulated and a hardware prototype of 1.92 kW is implemented. Simulation and experimental results are in accord with each other. The key advantages of the proposed inverter are as follows:

- Reduced switch count for heating two IH loads of different materials
- Simultaneous and independent control of different material IH loads

- Soft-switching operation during turn-ON
- High efficiency (96.11%)

Hence, the proposed 3S-DFRI is suitable for powering two different material IH loads. It can also be extended for more loads by adding three switching devices per two different material IH loads.

7.1.1.4 Proposed Dual Half-bridge Three Switch Resonant Inverter (DHB-3SRI) Configuration

A DHB-3SRI for two different material IH application has been proposed. Unlike the previously proposed topologies, it does not use any split capacitor arrangement. Two different material IH loads have been powered using three switches in the proposed inverter. The operating frequency of the inverter is 29 kHz-44 kHz and 215 kHz-228 kHz. Duty cycle and frequency based controls have been implemented. A detailed analysis and design of the proposed inverter has been carried out. OrCAD-Pspice software is used for performing simulations. A hardware prototype of 1.95 kW has been designed and tested. Simulation and experimental results are in good agreement with each other. The key advantages of the proposed inverter are as follows:

- Reduced component count
- Removal of lossy split capacitor arrangement
- Simultaneous and independent control of different material IH loads
- Soft switching operation during turn-ON
- High efficiency (97.38%)

Hence, the proposed inverter offers a compact solution for powering two IH loads of different materials. It can also be extended for more loads by adding three switching devices per two different material IH loads.

7.2 Comparison of the Proposed Inverter Configurations

A relative comparison of all four proposed inverter configurations is presented in Table 7.1. All the proposed inverter configurations are suitable for multi-load IC application and

they offer soft-switching operation, high efficiency and simultaneous as well as independent power control. Configuration-I (3SI) is suitable for heating two loads of ferromagnetic material type. Two steel vessels are used as IH loads. It offers reduced switch to load ratio. Its extension can heat vessels of different material but the component count will be more. It uses ADC control and control complexity is less. It is suitable for two IH loads of medium power. Configuration-II (FB-MI) is suitable for heating multiple vessels of different material. Steel and aluminum vessels are used as IH loads. The component count for basic two loads is high. However, component count per additional load is reduced. Also, it does not use a split capacitor arrangement. It is suitable for multiple IH loads of medium/high power. Configuration-III (3S-DFRI) is suitable for heating two IH loads of different materials. It offers reduced switch to load ratio for different material IC application. It is suitable for one medium and one low power IH load. Both configuration-I and configuration-III use split capacitor arrangement which may increase the power losses. Configuration-IV (DHB-3SI) is suitable for heating two different material vessels. It does not use split capacitor arrangement which leads to increase in efficiency. It also offers reduced switch to load ratio for different material IC application. It is suitable for one medium and one low power IH load.

Hence, these four proposed inverter configurations are suitable for multi-load IC aplications with high efficiency and independent control.

Table 7.1: Comparison of the proposed inverter configurations

Features\Contributions	3SI	FB-MI	3S-DFRI	DHB-3SRI
Multiple load capability	Yes	Yes	Yes	Yes
Different material vessel heating capability	No	Yes	Yes	Yes
Control technique	ADC	ON-OFF	Frequency control, duty cycle control	Frequency control, duty cycle control
Independent & simultaneous power control	Yes	Yes	Yes	Yes
Operating frequency (kHz)	28	30 & 220	29-44, 215-228	29-44, 215-228
Control frequency (kHz)	28	1	29-44, 215-228	29-44, 215-228
Control complexity	Less	Less	Medium	Medium
No. of switches	3	6	3	3
No. of diodes	0	2	0	0
No. of capacitors	2	1	2	1
Components per additional two loads	3 S	2 S + 2 D	3 S	3 S
IH load rating	Load-1: 280 W Load-2: 280 W	Load-1: 840 W Load-2: 790 W	Load-1: 1200 W Load-2: 760 W	Load-1: 1100 W Load-2: 820 W
Total power rating	560 W	1.6 kW	2 kW	2 kW
Peak efficiency (%)	96.3	94.3	96.11	97.38
Application	Two medium power IH loads	Multiple medium/high power IH loads	One medium and one low power IH load	One medium & one low power IH load

7.3 Suggestions for Future Research

As an extension to the current research work, there is scope for exploring further for a prospective researcher:

- The operation of the proposed inverter circuits with AC based input supply can be studied.
- Application of SiC and GaN devices can be analysed for the proposed configurations.
- The operation of the proposed inverter configurations can be studied with reference to photo-voltaic input.
- Application of the proposed inverter topologies to the active surface induction heating application can be studied.

Bibliography

Bibliography

[1] O. Lucía, P. Maussion, E. J. Dede, and J. M. Burdío, "Induction heating technology and its applications: past developments, current technology, and future challenges," *IEEE Transactions on industrial electronics*, vol. 61, no. 5, pp. 2509–2520, 2013.

[2] H. Ogiwara, M. Itoi, and M. Nakaoka, "Pwm-controlled soft-switching sepp high-frequency inverter for induction-heating applications," *IEE Proceedings-Electric Power Applications*, vol. 151, no. 4, pp. 404–413, 2004.

[3] B. Saha and R.-Y. Kim, "High power density series resonant inverter using an auxiliary switched capacitor cell for induction heating applications," *IEEE Transactions on Power Electronics*, vol. 29, no. 4, pp. 1909–1918, 2013.

[4] H. Sarnago, O. Lucia, A. Mediano, and J. M. Burdio, "Class-d/de dual-mode-operation resonant converter for improved-efficiency domestic induction heating system," *IEEE Transactions on Power Electronics*, vol. 28, no. 3, pp. 1274–1285, 2012.

[5] T. Mishima, C. Takami, and M. Nakaoka, "A new current phasor-controlled zvs twin half-bridge high-frequency resonant inverter for induction heating," *IEEE Transactions on Industrial Electronics*, vol. 61, no. 5, pp. 2531–2545, 2013.

[6] O. Lucia, J. M. Burdio, I. Millan, J. Acero, and D. Puyal, "Load-adaptive control algorithm of half-bridge series resonant inverter for domestic induction heating," *IEEE transactions on industrial electronics*, vol. 56, no. 8, pp. 3106–3116, 2009.

[7] V. Esteve, J. Jordan, E. Sanchis-Kilders, E. J. Dede, E. Maset, J. B. Ejea, and A. Ferreres, "Enhanced pulse-density-modulated power control for high-frequency induction heating inverters," *IEEE Transactions on Industrial Electronics*, vol. 62, no. 11, pp. 6905–6914, 2015.

[8] H. Sarnago, O. Lucia, D. Navarro, and J. M. Burdio, "Operating conditions monitoring for high power density and cost-effective resonant power converters," *IEEE Transactions on Power Electronics*, vol. 31, no. 1, pp. 488–496, 2015.

[9] C. Bi, H. Lu, K. Jia, J. Hu, and H. Li, "A novel multiple-frequency resonant inverter for induction heating applications," *IEEE Transactions on Power Electronics*, vol. 31, no. 12, pp. 8162–8171, 2016.

[10] N. A. Ahmed and M. Nakaoka, "Boost-half-bridge edge resonant soft switching pwm high-frequency inverter for consumer induction heating appliances," *IEE Proceedings-Electric Power Applications*, vol. 153, no. 6, pp. 932–938, 2006.

[11] B. Saha, S. K. Kwon, N. A. Ahmed, H. Omori, and M. Nakaoka, "Commercial frequency ac to high frequency ac converter with boost-active clamp bridge single stage zvs-pwm inverter," *IEEE Transactions on Power Electronics*, vol. 23, no. 1, pp. 412–419, 2008.

[12] Z.-F. Li, J.-C. Hu, M.-S. Huang, Y.-L. Lin, C.-W. Lin, and Y.-M. Meng, "Load estimation for induction heating cookers based on series rlc natural resonant current," *Energies*, vol. 15, no. 4, p. 1294, 2022.

[13] H. Sarnago, O. Lucia, A. Mediano, and J. M. Burdio, "Multi-mosfet-based series resonant inverter for improved efficiency and power density induction heating applications," *IEEE transactions on power electronics*, vol. 29, no. 8, pp. 4301–4312, 2013.

[14] E. Plumed, I. Lope, J. Acero, and J. M. Burdío, "Domestic induction heating system with standard primary inductor for reduced-size and high distance cookware," *IEEE Transactions on Industry Applications*, 2022.

[15] O. Jimenez, O. Lucia, I. Urriza, L. A. Barragan, P. Mattavelli, and D. Boroyevich, "An fpga-based gain-scheduled controller for resonant converters applied to induction cooktops," *IEEE Transactions on Power Electronics*, vol. 29, no. 4, pp. 2143–2152, 2013.

[16] D. N. Sankhe, R. R. Sawant, and Y. S. Rao, "Fpga-based hybrid control strategy for resonant inverter in induction heating applications," *IEEE Journal of Emerging and Selected Topics in Industrial Electronics*, vol. 3, no. 1, pp. 156–165, 2021.

[17] F. Forest, E. Labouré, F. Costa, and J. Y. Gaspard, "Principle of a multi-load/single converter system for low power induction heating," *IEEE Transactions on Power Electronics*, vol. 15, no. 2, pp. 223–230, 2000.

[18] J. M. Burdio, F. Monterde, J. R. Garcia, L. A. Barragan, and A. Martinez, "A two-output series-resonant inverter for induction-heating cooking appliances," *IEEE Transactions on Power Electronics*, vol. 20, no. 4, pp. 815–822, 2005.

[19] H. Fujita, N. Uchida, and K. Ozaki, "A new zone-control induction heating system using multiple inverter units applicable under mutual magnetic coupling conditions," *IEEE Transactions on Power Electronics*, vol. 26, no. 7, pp. 2009–2017, 2010.

[20] M. Perez-Tarragona, H. Sarnago, O. Lucia, and J. M. Burdio, "Design and experimental analysis of pfc rectifiers for domestic induction heating applications," *IEEE transactions on Power Electronics*, vol. 33, no. 8, pp. 6582–6594, 2017.

[21] F. Forest, S. Faucher, J.-Y. Gaspard, D. Montloup, J.-J. Huselstein, and C. Joubert, "Frequency-synchronized resonant converters for the supply of multiwinding coils in induction cooking appliances," *IEEE transactions on industrial electronics*, vol. 54, no. 1, pp. 441–452, 2007.

[22] D. Vijaya Bhaskar, N. Vishwanathan, T. Maity, and S. Porpandiselvi, "A three-output inverter for induction cooking application with independent control," *EPE Journal*, vol. 28, no. 2, pp. 89–99, 2018.

[23] O. Lucia, J. M. Burdio, L. A. Barragan, J. Acero, and I. Millán, "Series-resonant multiinverter for multiple induction heaters," *IEEE Transactions on Power Electronics*, vol. 25, no. 11, pp. 2860–2868, 2010.

[24] O. Lucia, H. Sarnago, and J. M. Burdio, "Soft-stop optimal trajectory control for improved performance of the series-resonant multiinverter for domestic induction heating applications," *IEEE Transactions on Industrial Electronics*, vol. 62, no. 10, pp. 6251–6259, 2015.

[25] M. Pérez-Tarragona, H. Sarnago, Ó. Lucía, and J. M. Burdío, "High performance full-bridge multi-inverter featuring 900-v sic devices for domestic induction heating applications," *EPE Journal*, vol. 27, no. 4, pp. 143–152, 2017.

[26] L. Meng and K. W. E. Cheng, "Wireless power transfer technology for electric iron based on multi-coils induction heating design," *IET Power Electronics*, vol. 12, no. 10, pp. 2566–2577, 2019.

[27] J. Serrano, I. Lope, and J. Acero, "Nonplanar overlapped inductors applied to domestic induction heating appliances," *IEEE Transactions on Industrial Electronics*, vol. 66, no. 9, pp. 6916–6924, 2018.

[28] R. C. M. Gomes, M. A. Vitorino, D. A. Acevedo-Bueno, and M. B. de Rossiter Corrêa, "Multiphase resonant inverter with coupled coils for ac–ac induction heating application," *IEEE Transactions on Industry Applications*, vol. 56, no. 1, pp. 551–560, 2019.

[29] O. Lucia, D. Navarro, P. Guillén, H. Sarnago, and S. Lucia, "Deep learning-based magnetic coupling detection for advanced induction heating appliances," *IEEE access*, vol. 7, pp. 181 668–181 677, 2019.

[30] H. Sarnago, J. M. Burdio, and Ó. Lucía, "High-performance and cost-effective zcs matrix resonant inverter for total active surface induction heating appliances," *IEEE Transactions on Power Electronics*, vol. 34, no. 1, pp. 117–125, 2018.

[31] P. Guillen, H. Sarnago, O. Lucia, and J. M. Burdio, "Series-resonant matrix inverter with asymmetrical modulation for improved power factor correction in flexible induction heating appliances," *IEEE Transactions on Industrial Electronics*, 2022.

[32] P. Guillén, H. Sarnago, Ó. Lucía, and J. M. Burdío, "Mains-synchronized pulse density modulation strategy applied to a zvs resonant matrix inverter," *IEEE Transactions on Industrial Electronics*, vol. 68, no. 11, pp. 10 835–10 844, 2020.

[33] T. Tanaka, "A new induction cooking range for heating any kind of metal vessels," *IEEE Transactions on Consumer Electronics*, vol. 35, no. 3, pp. 635–641, 1989.

[34] H. Yonemori and M. Kobayashi, "On the heating characteristic and magnetic flux of a double-coil drive type induction heating cooker," in *IECON 2006-32nd Annual Conference on IEEE Industrial Electronics*. IEEE, 2006, pp. 2488–2493.

[35] T. Hirokawa, M. Okamoto, E. Hiraki, T. Tanaka, and M. Nakaoka, "A novel type time-sharing high-frequency resonant soft-switching inverter for all metal ih cooking appliances," in *IECON 2011-37th Annual Conference of the IEEE Industrial Electronics Society*. IEEE, 2011, pp. 2526–2532.

[36] T. Hirokawa, E. Hiraki, T. Tanaka, M. Okamoto, and M. Nakaoka, "The practical evaluations of time-sharing high-frequency resonant soft-switching inverter for all metal ih cooking appliances," in *IECON 2012-38th Annual Conference on IEEE Industrial Electronics Society*. IEEE, 2012, pp. 3302–3307.

[37] I. Millan, J. Burdío, J. Acero, O. Lucía, and S. Llorente, "Series resonant inverter with selective harmonic operation applied to all-metal domestic induction heating," *IET power electronics*, vol. 4, no. 5, pp. 587–592, 2011.

[38] S. K. Papani, V. Neti, and B. K. Murthy, "Dual frequency inverter configuration for multiple-load induction cooking application," *IET Power Electronics*, vol. 8, no. 4, pp. 591–601, 2015.

[39] H.-P. Park and J.-H. Jung, "Load-adaptive modulation of a series-resonant inverter for all-metal induction heating applications," *IEEE Transactions on Industrial Electronics*, vol. 65, no. 9, pp. 6983–6993, 2018.

[40] W. Han, K. Chau, C. Jiang, and W. Liu, "All-metal domestic induction heating using single-frequency double-layer coils," *IEEE Transactions on Magnetics*, vol. 54, no. 11, pp. 1–5, 2018.

[41] S. Khatroth and P. Shunmugam, "Cascaded full-bridge resonant inverter configuration for different material vessel induction cooking," *IET Power Electronics*, vol. 13, no. 19, pp. 4428–4438, 2020.

[42] W. Han, K. T. Chau, W. Liu, X. Tian, and H. Wang, "A dual-resonant topology-reconfigurable inverter for all-metal induction heating," *IEEE Journal of Emerging and Selected Topics in Power Electronics*, 2021.

[43] W. Han, K. Chau, and W. Lam, "All-utensil domestic induction heating system," *Energy Conversion and Management*, vol. 195, pp. 1035–1043, 2019.

[44] S. R. Ramalingam, C. Boopthi, S. Ramasamy, M. Ahsan, and J. Haider, "Induction heating for variably sized ferrous and non-ferrous materials through load modulation," *Energies*, vol. 14, no. 24, p. 8354, 2021.

[45] S. Komeda and H. Fujita, "A phase-shift-controlled direct ac-to-ac converter for induction heaters," *IEEE Transactions on Power Electronics*, vol. 33, no. 5, pp. 4115–4124, 2017.

[46] H. Sarnago, O. Lucia, A. Mediano, and J. M. Burdio, "A class-e direct ac–ac converter with multicycle modulation for induction heating systems," *IEEE Transactions on Industrial Electronics*, vol. 61, no. 5, pp. 2521–2530, 2013.

[47] S. Sharifi, M. Monfared, M. Babaei, and A. Pourfaraj, "Highly efficient single-phase buck–boost variable-frequency ac–ac converter with inherent commutation capability," *IEEE Transactions on Industrial Electronics*, vol. 67, no. 5, pp. 3640–3649, 2019.

[48] T. Mishima, Y. Nakagawa, and M. Nakaoka, "A bridgeless bhb zvs-pwm ac–ac converter for high-frequency induction heating applications," *IEEE Transactions on Industry Applications*, vol. 51, no. 4, pp. 3304–3315, 2015.

[49] T. Mishima, S. Sakamoto, and C. Ide, "Zvs phase-shift pwm-controlled single-stage boost full-bridge ac–ac converter for high-frequency induction heating applications," *IEEE Transactions on Industrial Electronics*, vol. 64, no. 3, pp. 2054–2061, 2016.

[50] S. Sakamoto, T. Mishima, and C. Ide, "A phase-shift pwm-controlled zvs boost full-bridge ac-ac converter for metal-surface high-frequency induction heating applications," in *2016 IEEE Energy Conversion Congress and Exposition (ECCE)*. IEEE, 2016, pp. 1–7.

[51] H. Sarnago, A. Mediano, and O. Lucia, "High efficiency ac–ac power electronic converter applied to domestic induction heating," *IEEE transactions on Power Electronics*, vol. 27, no. 8, pp. 3676–3684, 2012.

[52] H. Sarnago, O. Lucia, A. Mediano, and J. M. Burdio, "Direct ac–ac resonant boost converter for efficient domestic induction heating applications," *IEEE Transactions on Power Electronics*, vol. 29, no. 3, pp. 1128–1139, 2013.

[53] H. Sarnago, Ó. Lucía, M. Pérez-Tarragona, and J. M. Burdío, "Dual-output boost resonant full-bridge topology and its modulation strategies for high-performance induction heating applications," *IEEE Transactions on Industrial Electronics*, vol. 63, no. 6, pp. 3554–3561, 2016.

[54] M. Ozturk and N. Altintas, "Multi-output ac–ac converter for domestic induction heating," *Electrical Engineering*, pp. 1–20, 2022.

[55] O. Lucia, C. Carretero, J. M. Burdio, J. Acero, and F. Almazan, "Multiple-output resonant matrix converter for multiple induction heaters," *IEEE Transactions on Industry Applications*, vol. 48, no. 4, pp. 1387–1396, 2012.

[56] S. Khatroth and P. Shunmugam, "Single-stage pulse frequency controlled ac–ac resonant converter for different material vessel induction cooking applications," *International Journal of Circuit Theory and Applications*, vol. 49, no. 9, pp. 2865–2884, 2021.

[57] H. Sugimura, N. A. Ahmed, T. Ahmed, H.-W. Lee, and M. Nakaoka, "Utility ac frequency to high frequency acpower conversion circuit with soft switching pwm strategy," *KIEE International Transaction on Electrical Machinery and Energy Conversion Systems*, vol. 5, no. 2, pp. 181–188, 2005.

[58] P. Sharath Kumar, N. Vishwanathan, and B. K. Murthy, "Multiple-load induction cooking application with three-leg inverter configuration," *Journal of Power Electronics*, vol. 15, no. 5, pp. 1392–1401, 2015.

[59] H. Fujita and H. Akagi, "Pulse-density-modulated power control of a 4 kw, 450 khz voltage-source inverter for induction melting applications," *IEEE transactions on industry applications*, vol. 32, no. 2, pp. 279–286, 1996.

[60] M. K. Kazimierczuk and D. Czarkowski, *Resonant power converters*. John Wiley & Sons, 2012.

[61] V. Esteve, E. Sanchis-Kilders, J. Jordán, E. J. Dede, C. Cases, E. Maset, J. B. Ejea, and A. Ferreres, "Improving the efficiency of igbt series-resonant inverters using pulse density modulation," *IEEE transactions on industrial electronics*, vol. 58, no. 3, pp. 979–987, 2011.

Appendix

Publications

Refereed International SCI Journal Publications:

[1] Bhavin Salvi, S. Porpandiselvi and N. Vishwanathan, "A Three Switch Resonant Inverter for Multiple Load Induction Heating Applications," *IEEE Transactions on Power Electronics*, vol. 37, no. 10, pp. 12108-12117, Oct. 2022, doi: 10.1109/TPEL.2022.3173931.

[2] Bhavin Salvi, S. Porpandiselvi and N. Vishwanathan, "An Inverter Circuit Configuration Suitable for Vessels of Different Material for Multi-load Induction Cooking Application," *IEEE Journal of Emerging and Selected Topics in Power Electronics*, vol. 11, no. 3, pp. 3223-3235, June 2023, doi:10.1109/JESTPE.2023.3247482.

[3] Bhavin Salvi, S. Porpandiselvi and N. Vishwanathan, "A Dual Frequency Resonant Inverter for Different Material Vessel Induction Hob," *Electrical Engineering, Springer Nature*, pp. 1-11, September 2023, doi:10.1007/s00202-023-02032-w.

Journals Communicated:

[1] Bhavin Salvi, S. Porpandiselvi and N. Vishwanathan, "Dual Half-bridge Resonant Inverter for Different Material Induction Cooking Application," *Electric Power Components and Systems*. (Under Review)